University of Southampton Research Repository

University of Southampton

Faculty of Environmental and Life Sciences

School of Ocean and Earth Sciences

Analysis of Earth's Climate Sensitivity: Past, Present & Future

by

Alice Rachel Booth

Thesis for the degree of

Doctor of Philosophy

2025

“All models are wrong, but some are useful”

George E. P. Box

University of Southampton

Abstract

Faculty of Environmental and Life Sciences
School of Ocean and Earth Sciences

Doctor of Philosophy

Analysis of Earth's Climate Sensitivity: Past, Present & Future

by
Alice Rachel Booth

Earth's climate system is comprised of a complex web of interacting feedbacks, each operating on differing timescales and with varying spatial patterns. Our understanding of climate feedbacks inform quantitative estimates of climate sensitivity, which represents Earth's response to changes in its energy balance. Despite decades of research, understanding of climate sensitivity is incomplete, and this directly affects our ability to predict future climate change and develop effective mitigation and adaptation strategies. This thesis uses probabilistic assessment to explore and quantify Earth's climate feedbacks over multiple response timescales using multiple lines of evidence. Chapter 2 utilises an efficient earth system model with a Bayesian statistical framework to constrain Earth's fast and multidecadal feedbacks. Chapter 3 estimates the magnitude and equilibrium response timescale of the ice sheet-albedo feedback using proxy evidence from the most recent deglaciation which then inform long term projections of future warming in Chapter 4. Chapter 4 also utilises a conceptual energy balance model to explore polar amplification and the latitudinal behaviour of the total climate feedback parameter under different mean climatic states, both warmer and colder than today. Together, these findings provide new insights into the evolving spatial and temporal behaviour of Earth's feedbacks and help to develop understanding of climate sensitivity in the context of the past, present and future. This shall contribute towards the collective effort to predict and prepare for the future of our climate with the acknowledgement that Earth's feedbacks are likely to amplify human-induced warming on multiple time horizons.

Table of Contents

List of Tables

List of Figures

Research Thesis: Declaration of Authorship

I declare that this thesis and the work presented in it are my own and has been generated by me as the result of my own original research.

I confirm that:

1. This work was done wholly or mainly while in candidature for a research degree at this University;
2. Where any part of this thesis has previously been submitted for a degree or any other qualification at this University or any other institution, this has been clearly stated;
3. Where I have consulted the published work of others, this is always clearly attributed;
4. Where I have quoted from the work of others, the source is always given. With the exception of such quotations, this thesis is entirely my own work;
5. I have acknowledged all main sources of help;
6. Where the thesis is based on work done by myself jointly with others, I have made clear exactly what was done by others and what I have contributed myself;
7. Parts of this work have been published as:

Booth, A., Goodwin, P., & Cael, B. B. (2024). Ice sheet-albedo feedback estimated from most recent deglaciation. Geophysical Research Letters, 51, e2024GL109953

Signature: .... Date:...............................

Acknowledgements

This PhD journey has not been an easy one and I could not have made it to this stage without the help and support of a great many people. Firstly, and most importantly, I'd like to thank my primary supervisor Dr Phil Goodwin whose creation of the WASP model and EBM facilitated all the research in this thesis. His patience and guidance has been invaluable. I'd also like to thank my secondary supervisors, Dr Kevin Oliver, Prof Toby Tyrrell and particularly Dr B.B. Cael for providing feedback on drafts, advising on the journal publishing process, and contributing to early research design and discussion. I'd also like to thank Dr Francisco 'Kiko' Calafat for the use of his and Cael's dataset as an observational constraint in Chapter 2. Thank you as well to the NERC INSPRIRE DTP for funding my PhD and Fellowship at POST.

I am very grateful to my panel chair, Prof Ivan Haigh for looking out for me throughout this whole process and for conducting all my progression reviews. Similarly, I'd like to thank my examiners, Prof Helene Hewitt, Prof Bob Marsh, and Prof Piers Forster, for taking the time to trek through my confirmation report and thesis respectively, and for conducting the oral examinations.

I've been lucky enough to be able to work with Public Policy Southampton for the last three years of my PhD and I am extremely grateful to the entire team, particularly Giles and Wassim, for taking the time to teach me and give me the opportunity to gain such brilliant experiences in policy. You helped me realise what I wanted to do when I grew up!

Thank you so much to Julie, my wonderful Mentor, for keeping me sane and on track and listening to all my rants and PhD frustrations. You've taught me how to manage my brain.

Finally, I cannot put into words how much the love and support of my family and friends has contributed to the completion of this PhD. Mum, Will, Matthew, Auntie Willie, Dalo, Phoebe, Liv, Emily, Sasha, Hazel, Chris: you've all been there for me during some not-so-great points in the last four years. You have kept me going and made me a better, happier person. Thank you.

For my father,

thank you for everything.

xx

Chapter 1 Introduction

1.1 Motivation

Our ability to successfully predict future climate change and the impacts this will have on human populations is directly influenced by our understanding of climate sensitivity. A quantitative measure of Earth's response to changes to its energy balance, climate sensitivity represents the global mean surface temperature (GMST) change caused by elevated carbon dioxide (CO_2) levels in the atmosphere from anthropogenic emissions. Despite decades of research, the value of climate sensitivity is still uncertain and must be constrained to inform predictions of future climate change and allow humans to plan for the future of our planet. Uncertainty is extremely costly to the development of effective climate policy and continually slows international progress to address climate change (Hope, 2015; Smith *et al.*, 2023).

The ongoing uncertainty around climate sensitivity stems from the complex relationships between countless earth system feedbacks which are spatially and temporally heterogenous and will influence the system in different ways (Hansen *et al.*, 2005; Rohling *et al.*, 2018). Information about the inner workings of the earth system can be gleaned from a plethora of sources and each will capture different aspects of the earth system; the 800-ka oxygen isotope record extracted from an Antarctica ice core will contain different information to the shorter modern instrumental record of local sea surface temperatures (SST) in the northern Pacific Ocean, and both will capture different aspects of the system than a complex global climate model (GCM). Therefore, climate sensitivity may appear different depending on the line of evidence used to estimate it (Knutti, Rugenstein and Hegerl, 2017; Goodwin, 2018).

The overarching aim of this PhD is to improve our understanding of earth system dynamics and reduce the statistical uncertainty surrounding climate sensitivity and key climate feedbacks, thereby contributing to better-informed simulations of future climate change. I aim to improve understanding of climate sensitivity by utilising probabilistic assessment in conjunction with semi-empirical numerical models to combine evidence from the historical record, palaeoclimate record, and process understanding to produce estimates of the total climate feedback parameter and individual feedbacks that are consistent across multiple lines of evidence. This work assumes that climate sensitivity evolves spatially and over time due to the influence of time-evolving and spatially-variable fast and slow climate feedbacks.

A key gap in current understanding of climate sensitivity is the exact behaviour of Earth's feedbacks on different response timescales, and uncertainty persists in determining the magnitude and nature of fast, multi-decadal, and slow earth system feedbacks (Goodwin, 2021). I aim to address this throughout this thesis. In particular, Chapter 2 shall work to constrain Earth's fast and multi-decadal feedbacks through the use of an efficient earth system model with a Bayesian statistical framework. Beyond this, Chapters 3 and 4 shall focus on slow feedbacks, addressing uncertainty surrounding ice sheet-climate interactions on centennial to millennial-scale timescales. Despite acknowledgement that the ice sheet-albedo feedback has a significant amplifying influence, specific quantitative understanding is still limited, and ice sheet-climate interactions are typically simplified in model assessments of climate sensitivity (Forster *et al.*, 2021; Madsen *et al.*, 2022). Chapter 3 aims to address this through a proxy data-based probabilistic assessment of the ice sheet-albedo feedback during the most recent deglaciation. The simplification of Earth's slow feedbacks in model assessments of climate sensitivity has ramifications for our predictions of future climate change; we have very limited understanding of how earth's climate will evolve beyond the end of the 21st century which, while perhaps of limited relevance to those alive today, has major consequences for future generations and it is important that we consider the long term implications of humanity's actions today on the world that we will leave for our descendants. To this end, in Chapter 4 I build on the work of Chapter 3 to explore the implications of slow ice sheet-climate interactions for climate sensitivity on long timescales.

While methods differ, all work in this thesis is based around the concept of probabilistic assessment, with a primary intention of generating quantitative estimates for climate feedbacks, constrained by multiple sources of existing evidence. By improving the quantification of the total climate feedback parameter and key individual climate feedbacks, this work contributes towards the collective understanding of climate sensitivity. Crucially, it should be noted that the complexity of climate sensitivity is such that a comprehensive assessment of all sources of uncertainty is beyond the scope of this thesis. For instance, our understanding of climate sensitivity is tied to our understanding of radiative forcing, particularly from CO_2, but this thesis shall focus specifically on climate feedbacks on multiple spatial and temporal scales.

The remainder of this chapter serves to summarise the background literature surrounding climate sensitivity and to further highlight the research gaps that I intend to address. The basic methodology of the key models utilised in this thesis is also introduced here.

1.2 Climate Sensitivity

1.2.1 Definitions

The concept of climate sensitivity grew out of a need to quantify the impact humans were having on the world around us and specific definitions continue to evolve. For more than a century, scientists have worked to calculate the global temperature rise that would occur for a given increase in atmospheric CO_2 in an attempt to understand how increasing human emissions could affect Earth's climate (Arrhenius, 1897; Callendar, 1938). Climate sensitivity can be defined in numerous ways, but the most common measure used today is that of ECS which is the GMST increase per doubling of atmospheric CO_2 after the climate has reached a new quasi-equilibrium (Charney *et al.*, 1979; Hansen and Takahashi, 1984). Since first proposed by Charney in 1979, the accepted estimate of ECS remained relatively unchanged for more than 30 years at a likely range of 1.5 – 4.5°C per doubling of atmospheric CO_2 (Charney *et al.*, 1979; Schwartz, 2012; IPCC, 2013). This range was narrowed in the most recent 6th Assessment Report authored by the Intergovernmental Panel on Climate Change (IPCC) after a tremendous community effort to improve process understanding and model accuracy. The IPCC now estimates that ECS lies in the likely range of 2.5 – 4.0°C, with a best estimate of 3.0°C (Forster *et al.*, 2021).

ECS is an imperfect definition for climate sensitivity as it fails to incorporate slower Earth feedbacks that operate over a timescale of more than ~100 years (Knutti, Rugenstein and Hegerl, 2017; Rohling *et al.*, 2018). Earth System Sensitivity (ESS) is a more recent concept that also incorporates all slower feedback processes except for the carbon cycle (Lunt *et al.*, 2010; Knutti and Rugenstein, 2015). The processes included in the definitions of ECS and ESS are illustrated in figure 1.1. The distinction between ECS and ESS in models is generally made under an assumption of timescale separation into fast and slow processes but the interacting nature of Earth's feedbacks means that this distinction is somewhat irrelevant in the real world (Knutti and Rugenstein, 2015; Ashwin and von der Heydt, 2020).

However, Earth's climate system is not in equilibrium but is instead in a constantly changing, transient state that evolves over time (Yoshimori *et al.*, 2016; Meehl *et al.*, 2020). As such, the magnitude of climate sensitivity is not static or even linear over time, but instead evolves due to the complex interacting relationships of multiple feedbacks and forcings (Zeebe, 2013; Goodwin, 2018; Rohling *et al.*, 2018; Rugenstein *et al.*, 2020). Therefore, it could be argued that the concepts of ECS and ESS are too disconnected from the real world to be of much use. Measures such as the Transient Climate Response (TCR), which quantifies the GMST at the time of doubling of CO_2 after an idealised 1% yr^{-1} CO_2 increase experiment, may provide greater insight into the initial response of the climate system over several decades (Knutti, Rugenstein and Hegerl, 2017). The Transient Climate Response to Cumulative Carbon Emissions (TCRE) meanwhile, places warming in the context of total emitted CO_2 and is therefore more relevant for the estimation of carbon budgets (Knutti and Rugenstein, 2015). The distinction between TCR, TCRE, ESS and ECS are depicted in figure 1.1.

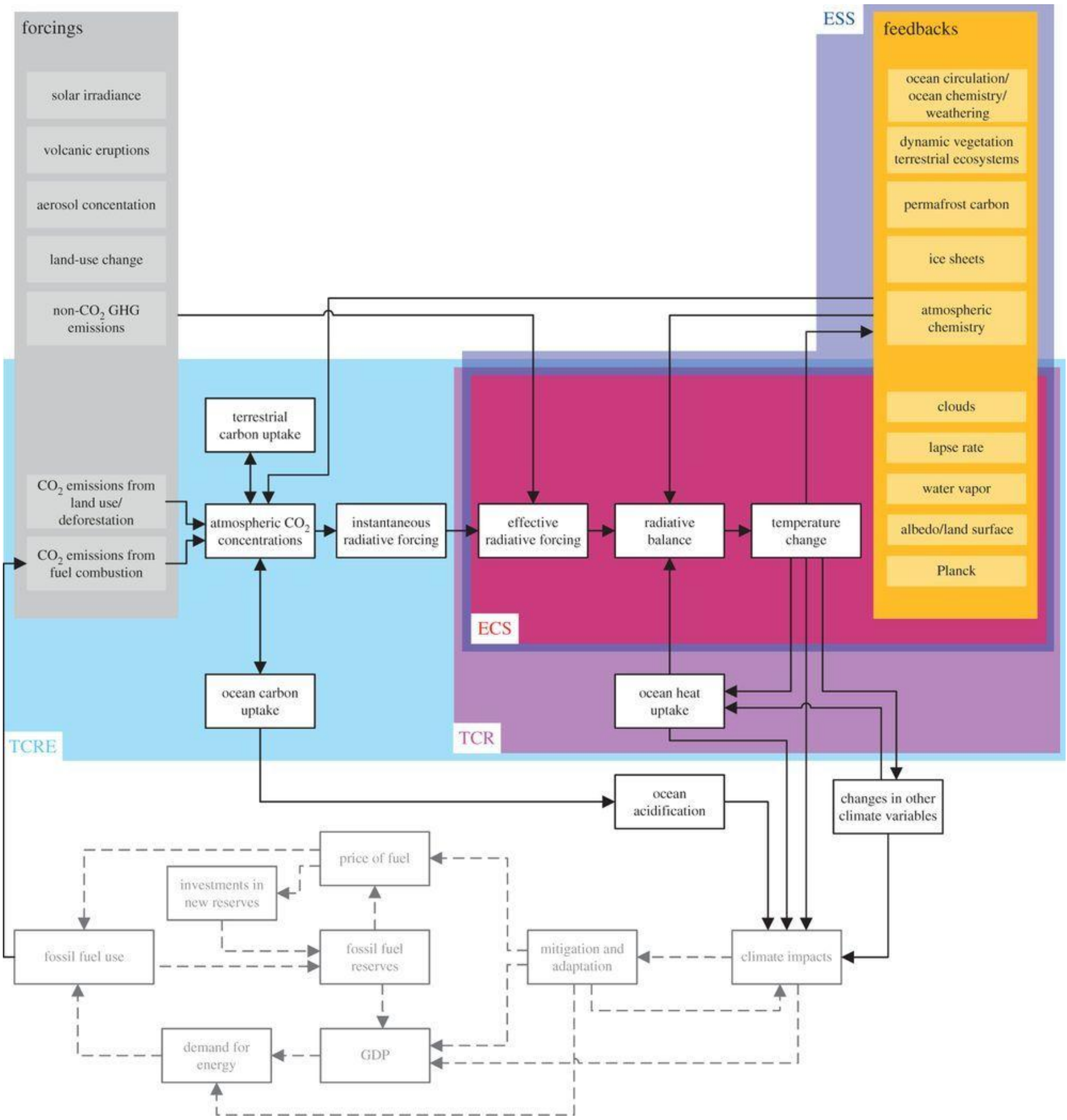

Figure 1.1: *Illustrative distinction between feedbacks acting in and on the climate system. The coloured boxes indicate the processes included in different definitions of climate sensitivity. From Knutti and Rugenstein (2015).*

All measures of climate sensitivity are imperfect. Despite not fully describing reality, ECS remains extremely valuable for model comparison and evaluation and is a good fundamental indicator of Earth's sensitivity to CO_2 forcing (Grose *et al.*, 2018; Dai *et al.*, 2020; Meehl *et al.*, 2020). The value of ECS lies in its almost ubiquitous use in climate science allowing for easy model comparison and evaluation, and as a fundamental indicator of climate sensitivity (Grose *et al.*, 2018; Dai *et al.*, 2020).

1.2.2 Causes of uncertainty

The Earth System is comprised of a complex web of interacting feedback relationships, wherein a change in one climate parameter will affect another, which in turn can either amplify or dampen the original signal. The relative radiative contributions and exact impacts of different feedbacks can vary greatly over space and time, meaning the overall sensitivity of the system to perturbation can be difficult to quantify (Hansen *et al.*, 2005; Knutti and Rugenstein, 2015; Rohling *et al.*, 2018; Chao and Dessler, 2021).

Different feedbacks operate over different timescales. Some, like the Planck feedback, are almost instantaneous, whilst others take years to complete the loop (Knutti and Rugenstein, 2015). Some modes are so slow that it can take millions of years to see a measurable response. Figure 1.2 depicts the key climate feedbacks that influence climate sensitivity and the timescales over which they operate. The time-evolving nature of Earth's fast and slow feedback loops results in a climate sensitivity that evolves over time and so may appear different depending on the time window studied (Caballero and Huber, 2013; Zeebe, 2013; Pfister and Stocker, 2017; Goodwin, 2018).

The increasingly dominant consensus within climate science is that climate feedbacks, and consequently climate sensitivity, are strongly influenced by the background state of the climate with higher estimates generated using data from past warm periods in the palaeoclimate record, compared to cooler periods (Caballero and Huber, 2013; Meraner, Mauritsen and Voigt, 2013; von der Heydt *et al.*, 2014; Friedrich *et al.*, 2016; Shaffer *et al.*, 2016; Zhu, Poulsen and Tierney, 2019; Anagnostou *et al.*, 2020; Sherwood *et al.*, 2020; Zhu and Poulsen, 2020; Bloch-Johnson *et al.*, 2021). The exact nature of this relationship is still being debated with both changes in atmospheric CO_2 concentration and temperature considered potential drivers (Rohrschneider, Stevens and Mauritsen, 2019; Bloch-Johnson *et al.*, 2021). However, modelling evidence suggests that the relationship is primarily a dependence between temperature and feedback strength, found to explain 69% of the sensitivity (Bloch-Johnson *et al.*, 2021), in which water vapour and cloud feedbacks have the greatest influence (Meraner, Mauritsen and Voigt, 2013; Seeley and Jeevanjee, 2021). The role of state dependence is still uncertain, and understanding would particularly benefit from further study of cloud feedbacks, which remain the largest contribution to simulation uncertainty (Caldwell *et al.*, 2016; Zelinka, Zhou and Klein, 2016; Zelinka *et al.*, 2020). Like feedbacks, radiative forcings have also been shown to experience state dependence. In particular, the magnitude of radiative forcing from a doubling of atmospheric CO_2, long assumed to be constant, has recently been shown to change with background climatic state (Jeevanjee *et al.*, 2021; He *et al.*, 2023).

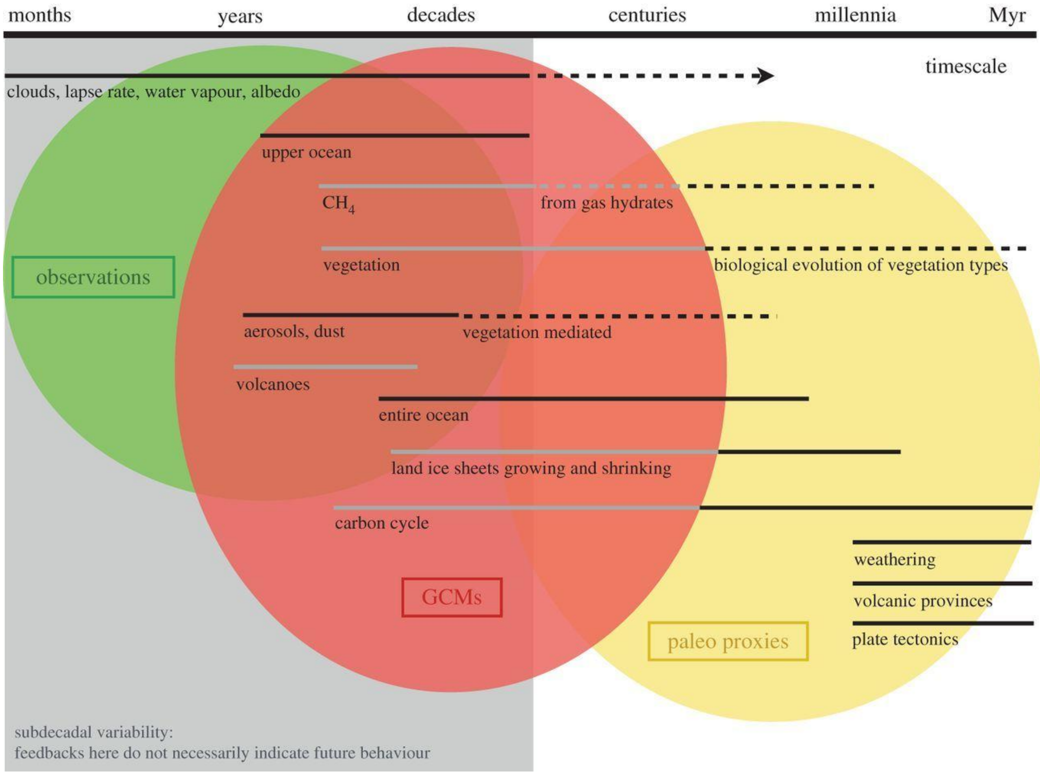

Figure 1.2: *Climate feedback processes involved in climate sensitivity and their response timescales. Grey bars indicate processes that are assumed to be partly inactive or non-existent by GCMs. Dashed lines indicate timescales where feedback is weaker or only operates under certain circumstances. Circles indicate the processes that are captured by different lines of evidence: observational records, model simulations, and palaeoclimate proxies. From Knutti and Rugenstein (2015).*

Efforts to quantify climate sensitivity are further complicated by the presence of tipping elements within the Earth system that could trigger abrupt climatic change if critical thresholds, or 'tipping points' are crossed (Lenton *et al.*, 2008). The scientific community has now identified a number of potential tipping elements within the system, several of which are exhibiting early warning signs of reaching critical tipping points (Lenton *et al.*, 2019; Rosier *et al.*, 2021; Abrams *et al.*, 2023). Notable elements of concern include the Greenland ice sheet, the Atlantic Meridional Overturning Circulation, and die-back of the Amazon rainforest (Weijer *et al.*, 2019; Bradley and Hewitt, 2024; Flores *et al.*, 2024). Once a tipping point is crossed, self-amplifying feedbacks propel the system towards a new stable state, with potentially dramatic impacts on other components of the earth system, which may themselves trigger further tipping cascades in other tipping elements (Levermann *et al.*, 2012; Lenton *et al.*, 2024; Wunderling *et al.*, 2024). Tipping points have been crossed before in Earth's history, and are observable within the geological record, but we are now experiencing unprecedented, rapid anthropogenic forcing under new boundary conditions, introducing considerable unknowns into our predictive models (Steffen *et al.*, 2018; Stocker *et al.*, 2024). The existence of tipping points is important because under an abrupt transition, the assumption of a linear response to perturbation no longer holds, and this introduces further uncertainty into estimates of climate sensitivity (Ashwin and von der Heydt, 2020).

1.2.3 Climate feedbacks

The strength of a climate feedback is quantified by its climate feedback parameter, λ ($Wm^{-2}K^{-1}$), which is defined here as the change in outgoing radiation at the top of the atmosphere (TOA) per unit of temperature change. Sign conventions for λ differ between studies, but this thesis follows the convention that the total climate feedback parameter, λ_{total} ($Wm^{-2}K^{-1}$), being the additive combination of all individual feedbacks, is negative for a stable climate system, such that individual positive λ terms indicate amplifying contributions to λ_{total}. The magnitude of an individual feedback, λ, at time, t, is calculated as follows:

$$\lambda(t) = \frac{N(t) - F_{total}(t)}{\Delta T(t)}$$

Equation 1.1

Where N is the net TOA energy imbalance (Wm^{-2}), F_{total} is the total radiative forcing (Wm^{-2}), and ΔT is the global surface temperature anomaly (K). For reference, this translates to an ECS at time, t, that is calculated as follows once all feedbacks have been considered:

$$ECS(t) = -\frac{F_{2xCO2}}{\lambda_{total}(t)} = \frac{F_{2xCO2}\Delta T(t)}{N(t) - F_{total}(t)}$$

Equation 1.2

Where F_{2xCO2} is the radiative forcing for a doubling of atmospheric CO_2.

Due to computational practicalities, this work departs from the traditional ECS definition for climate sensitivity, instead favouring the metric of 'effective climate sensitivity' (EffCS, in K), similar to the method developed by Gregory et al. (2004). Gregory's EffCS is derived from the earth system response during the first 150 years following an instantaneous quadrupling of CO_2. As GMST tends towards equilibrium, regression of the TOA energy imbalance against temperature can be extrapolated to the eventual GMST when the energy imbalance is zero (Gregory *et al.*, 2004). Throughout, I assume a time-evolving λ_{total}, resulting in a gradient that changes over time. Although comparable to ECS, this method estimates climate sensitivity using data from a system that is not in equilibrium and does not require the very long model runs, in excess of 1000 years, that are required for ECS (Danabasoglu and Gent, 2009; Rugenstein *et al.*, 2020). This follows previous similar studies of climate sensitivity (e.g. (Sherwood *et al.*, 2020)).

From a modelling perspective, the total climate feedback parameter, λ_{total}, can be considered the additive combination of all fast and slow feedbacks operating within the Earth System and therefore can be broken down into component terms based on response timescale (Knutti and Rugenstein, 2015). Again, it could be argued that this assumption is unrealistic, but the complicated web of interacting feedbacks within the Earth system determines that the practicalities of disentangling individual feedbacks becomes near impossible. Furthermore, all feedbacks are spatially heterogeneous and the resultant climate responses are distinctly non-fungible and will differ by region, a phenomenon known as the pattern effect (Sherwood *et al.*, 2015; Chao and Dessler, 2021; Andrews *et al.*, 2022; Zhou *et al.*, 2023). However, in practice, the magnitudes of individual feedbacks are generally assumed to be globally ubiquitous as the uncertainties involved in attempting to differentiate spatially would make any resulting estimates much less useful.

As can be expected, the international climate modelling effort has focused heavily on feedbacks most relevant to the next few centuries of future climatic change. These faster feedbacks have been well-constrained, informed by observational evidence from the historical record (Kamae *et al.*, 2016; Fyke *et al.*, 2018; Rugenstein *et al.*, 2020). However, within increasing timescales comes reduced understanding as the volume of observational data decreases, and as such, the magnitude of climate feedbacks that operate on multi-decadal, centennial, and millennial timescales are less well-constrained.

The relationship between the cryosphere and global temperature is a key focus within this thesis, explored in more depth in chapters 3 and 4. The cryosphere is defined as the frozen aspects of the earth system, incorporating snow, sea ice, ice sheets, glaciers, and permafrost (Fox-Kemper *et al.*, 2021). Cryosphere feedbacks are therefore numerous, involving the atmosphere, biosphere, and both the surface and deep ocean, and operate over multiple temporal scales. Perhaps the most influential aspect of the cryosphere relevant to global temperature is that of albedo; snow and ice are highly reflective meaning any reduction in snow and ice cover results in a decrease in the local albedo, increasing the absorption of incoming radiation and raising local temperature. On short timescales, changes in snow cover drive changes in local temperature, but the feedback becomes extremely significant over multi-decadal, centennial, and millennial timescales when considering large spatial changes in the extent of sea ice and ice sheets (Clark, Alley and Pollard, 1999; Stap *et al.*, 2017; Scherrenberg *et al.*, 2023). Xiao *et al.* (2017) calculate the magnitude of the short-term northern hemisphere snow-albedo feedback during the period 2003-2016 as 0.18 ± 0.08 $Wm^{-2}K^{-1}$. On longer timescales, the magnitude of the ice sheet-albedo feedback continues to be very uncertain, and this is something that I investigate in this work. Alongside albedo, ice sheets more indirectly affect climate through freshwater fluxes and regional cloud, wind, and precipitation patterns, but these are beyond the scope of this thesis (Fyke *et al.*, 2018).

1.2.4 Estimates of climate sensitivity

Climate sensitivity can be calculated using several lines of evidence: model simulations based on physical understanding; observations within the historical record; and palaeoclimate reconstructions. As illustrated in figure 1.2, no single line of evidence succeeds in capturing all earth system processes on all timescales meaning all lines of evidence need to be combined to create a complete picture of Earth's complex climate system (Stevens *et al.*, 2016; Goodwin, 2018; Sherwood *et al.*, 2020). Different lines of evidence therefore tend to indicate differing estimates of climate sensitivity, demonstrating the varying timescales being captured (Knutti, Rugenstein and Hegerl, 2017; Goodwin, 2018). To understand climate sensitivity over all relevant timeframes and reduce uncertainty, we must combine the evidence from multiple different sources (Stevens *et al.*, 2016; Sherwood *et al.*, 2020).

1.2.4.1 Model simulations

Climate sensitivity can be estimated from our understanding of the current climate system and its internal feedbacks and variability. Our understanding of these processes is typically explored using comprehensive GCMs which are informed using physical theory to run idealised experiments within a computerised representation of our climate system. In this way, we can explore global and regional responses to simulated scenarios to gain knowledge about the internal behaviour of the system (Raju and Kumar, 2020). However, GCMs often lack the spatial resolution required to fully represent processes that occur on very small scales, such as cloud droplet formation, which instead must be accounted for by approximate parameterizations (McFarlane, 2011; Knutti, Baumberger and Hirsch Hadorn, 2019; Raju and Kumar, 2020).

The drive to improve model skill and reliability has given rise to climate model intercomparison projects (CMIPs) which create opportunities to explore climate sensitivity across a large multi-model ensemble (Tebaldi and Knutti, 2007). The quality of an individual model is traditionally determined by its consistency with observations of current climate with the assumption that models that can reproduce current climate will be best placed to predict future changes or estimate ECS, but unfortunately this is not always the case (Gleckler, Taylor and Doutriaux, 2008; Waugh and Eyring, 2008; Caldwell, Zelinka and Klein, 2018). A potential solution that is currently being explored is the concept of 'emergent constraints' which refer to observable quantities in the current climate that tend to be a good predictor of future changes in GCMs and therefore can be used to identify trustworthy models (Caldwell, Zelinka and Klein, 2018; Hall *et al.*, 2019). Potential emergent constraints for climate sensitivity have also been identified, with most relating to cloud feedbacks as the largest source of uncertainty in ECS in current GCMs (Caldwell, Zelinka and Klein, 2018; Cox, Huntingford and Williamson, 2018; Hall *et al.*, 2019; Schlund *et al.*, 2020; Sherwood *et al.*, 2020). However, not all identified emergent constraints have a solid physical basis and many do not hold for more recent GCMs, such as those in CMIP6, and so this method should be applied with caution (Caldwell *et al.*, 2014; Caldwell, Zelinka and Klein, 2018; Schlund *et al.*, 2020; Sherwood and Forest, 2024).

Despite significant ongoing uncertainty, the evidence from models based on process understanding is difficult to reconcile with a low estimate for ECS with most recent simulations favouring a sensitivity at the higher end of the IPCC's range (Knutti, Rugenstein and Hegerl, 2017; Gettelman *et al.*, 2019; Bjordal *et al.*, 2020; Meehl *et al.*, 2020; Rugenstein *et al.*, 2020; Zelinka *et al.*, 2020; Zhu and Poulsen, 2020).

1.2.4.2 Historical record

Since the 18th century, the world has warmed by more than 1°C, primarily due to rise of anthropogenic greenhouse gases (GHGs) and aerosols, and this warming is well documented by instrumental observations (IPCC, 2013; Allen, 2018). The historical climate record is therefore a useful data source to inform estimates of climate sensitivity. Estimates derived from the historical record are typically calculated from observed changes in temperature and ocean heat uptake using a conceptual or physical model to infer ECS from a present-day warming in response to forcing relative to a baseline (Hegerl and Zwiers, 2011; Skeie *et al.*, 2014; Skeie *et al.*, 2018; Gregory *et al.*, 2020). Alternatively, observations can be used in conjunction with model simulations to identify a value for ECS that results in the greatest consistency between the two (Knutti and Tomassini, 2008; Skeie *et al.*, 2014; Johansson *et al.*, 2015).

Estimates for ECS using this line of evidence are generally lower than from other approaches with a best estimate of ~2°C (Knutti, Rugenstein and Hegerl, 2017; Sherwood *et al.*, 2020). However, extensive observational uncertainty persists, and data coverage is incomplete in certain regions and time periods (Cowtan *et al.*, 2015; Karl *et al.*, 2015; Richardson *et al.*, 2016; Knutti, Rugenstein and Hegerl, 2017). Moreover, the historical climate record is too short to capture feedbacks that operate on longer timescales and natural variability may obscure key trends (Olson *et al.*, 2013; Huber, Beyerle and Knutti, 2014). Furthermore, our climate is in a transient state and this must be considered when drawing conclusions on ECS from observations of a system undergoing constant change (Huber, Beyerle and Knutti, 2014; Yoshimori *et al.*, 2016; Knutti, Rugenstein and Hegerl, 2017; Gregory *et al.*, 2020).

Until recently, many estimates based on the instrumental record have assumed that feedbacks are spatially and temporally constant, which is unrealistic (Otto *et al.*, 2013; Gregory and Andrews, 2016; Knutti, Rugenstein and Hegerl, 2017; Andrews *et al.*, 2018). The spatial and temporal heterogeneity of feedback strength is partly a consequence of unforced 'pattern effects' wherein the spatial pattern of surface warming will alter the strength of a feedback at a particular time (Rose *et al.*, 2014; Armour, 2017; Andrews *et al.*, 2018; Dessler, 2020; Dong *et al.*, 2020; Chao, Muller and Dessler, 2022). In particular, variations in shortwave cloud feedbacks have been identified as the primary contributor to the unforced pattern effect (Dessler, Mauritsen and Stevens, 2018; Dessler, 2020; Chao and Dessler, 2021; Chao, Muller and Dessler, 2022). Figure 1.3 shows how the strength of the pattern effect influences the magnitude of committed warming, that is the GMST change that is 'inevitable' due to the lifetime of CO_2 in the Earth system (Mauritsen and Pincus, 2017; Zhou *et al.*, 2021).

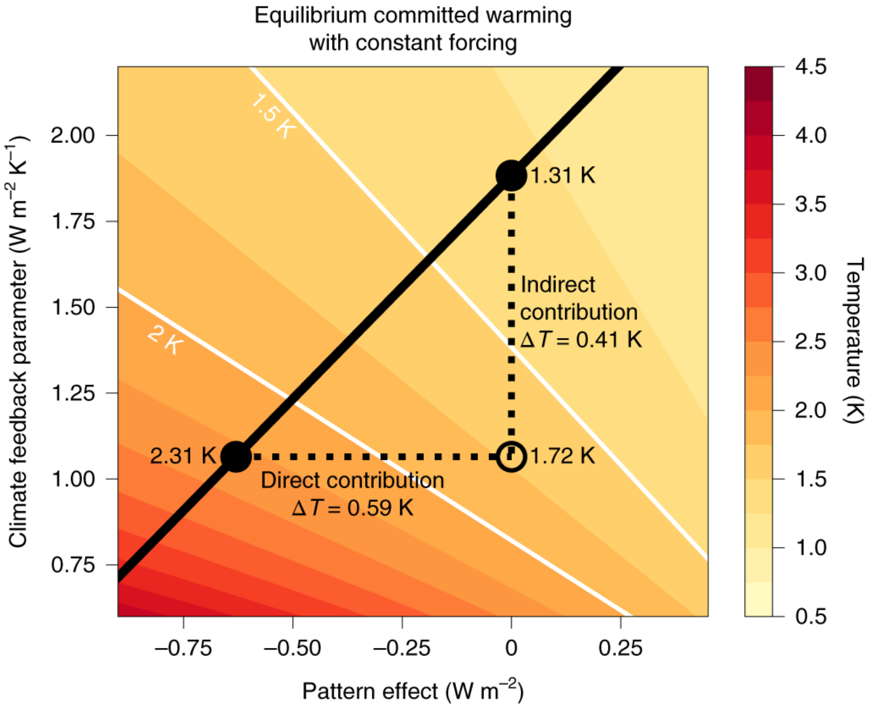

Figure 1.3: *Impact of the pattern effect on equilibrium committed warming with constant forcing. White contours indicate thresholds from the Paris Agreement. Black line describes the relationship between the pattern effect and λ. Black markers highlight the difference in committed warming depending on the strength of the pattern effect. From Zhou et al., (2021).*

Due to the pattern effect, some studies have concluded that estimates of ECS that assume constant feedbacks are likely underestimated, thereby resolving the apparent discrepancy between estimates based on observations versus GCMs (Gregory and Andrews, 2016; Knutti, Rugenstein and Hegerl, 2017; Andrews *et al.*, 2018; Dessler, 2020; Sherwood *et al.*, 2020;

Tokarska *et al.*, 2020). The overall effect of pattern effects can lead estimates of ECS based on historical observations to be as much as 0.5K below the true value of ECS (Dessler, 2020).

Figure 1.4 depicts a visual comparison of the magnitude of the pattern effect in the CMIP5 and CMIP6 ensembles of complex climate models. Whilst the majority of models in both ensembles indicate an amplifying effect from multi-decadal feedbacks, with a mean change of 0.51 $Wm^{-2}K^{-1}$ from multi-annual to centennial timescales in CMIP5 and 0.4 $Wm^{-2}K^{-1}$ in CMIP6, some models do show a damping effect, as illustrated by their negative change in λ (Andrews, Gregory and Webb, 2015; Dong *et al.*, 2020). This highlights the uncertainty that persists and that must be remedied to improve estimates of climate sensitivity.

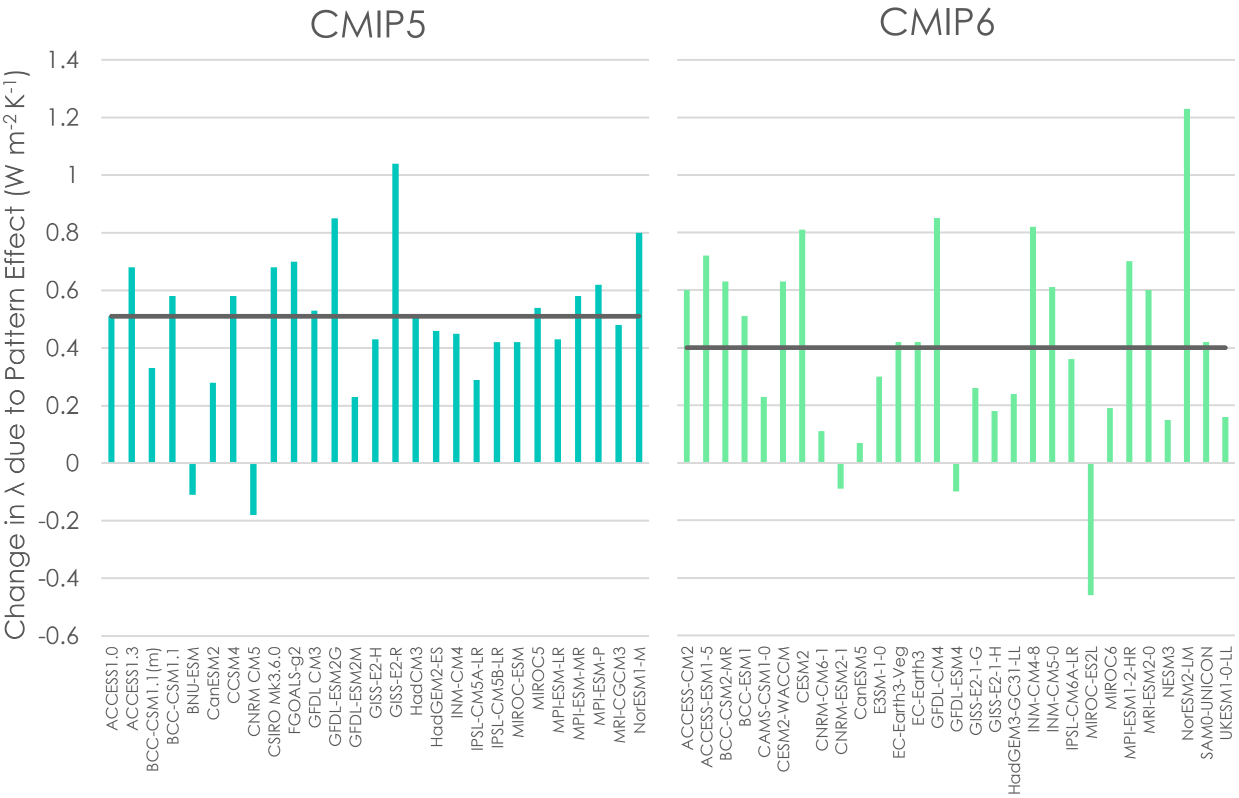

Figure 1.4: *Bar chart showing the difference in magnitude in λ between short timescales (0 – 20 years) and longer timescales (121-150 years) in CMIP5 and CMIP6. The grey lines indicate the ensemble means. CMIP5 data from Andrews, Gregory and Webb (2015). CMIP6 data from Dong et al. (2020).*

1.2.4.3 Palaeoclimate record

Past climates offer a unique insight into the slower feedbacks of the climate system and can provide useful information with which to constrain climate sensitivity (Rohling *et al.*, 2012b; Rohling *et al.*, 2018; Tierney *et al.*, 2020a). Estimates derived from the palaeoclimate record are typically based on periods of time where the climate remained sufficiently stable over multiple centuries to millennia as the system can be assumed to be in quasi-equilibrium (Covey, Sloan and Hoffert, 1996; Rohling *et al.*, 2012b; von der Heydt *et al.*, 2016). Climate sensitivity can be estimated either by comparing time series of a specific time slice to a pre-industrial control to determine how the climate responded to the change in radiative forcings, or by studying multiple climate cycles over a long time series such as the glacial/ interglacial transitions of the Pleistocene (~ past 2.5Ma) (Rohling *et al.*, 2012b; Friedrich *et al.*, 2016; von der Heydt *et al.*, 2016; Rohling *et al.*, 2018; Inglis *et al.*, 2020; Tierney *et al.*, 2020b).

The growing consensus is that climate sensitivity is influenced by the background climate state and is higher in warmer climates (Caballero and Huber, 2013; Meraner, Mauritsen and Voigt, 2013; Friedrich *et al.*, 2016; Anagnostou *et al.*, 2020; Zhu and Poulsen, 2020). Therefore, both cold periods like the Last Glacial Maximum (LGM ~20,000 years ago) and warm periods such as the Mid-Pliocene Warm Period (mPWP ~3.3 – 3.0Ma) must be studied with a consideration of changing feedbacks to derive a comprehensive estimate from the palaeoclimate record (Schmittner *et al.*, 2011; Caballero and Huber, 2013; von der Heydt *et al.*, 2016; Farnsworth *et al.*, 2019; Inglis *et al.*, 2020; Tierney *et al.*, 2020b).

However, the study of past climates incorporates additional uncertainty. The methods used to reconstruct past climates utilise indirect evidence that is unlikely to be spatially complete and may be influenced by multiple environmental factors alongside temperature (Rohling *et al.*, 2012b; von der Heydt *et al.*, 2016; Rohling *et al.*, 2018; Sherwood *et al.*, 2020). For example, the Mg/Ca palaeothermometer, utilises the ratio of magnesium to calcium in preserved fossil foraminifera from marine sediments to infer past ocean temperatures under the premise that in warmer oceans, foraminifera will incorporate more Mg into their calcite shells and the Mg/Ca ratio will be higher (Glaubke, 2022). However, the Mg/Ca ratio can also be influenced by secondary factors such as seawater chemistry, species type, or partial-dissolution and these must be accounted for when calibrating the proxy to reconstruct temperature (Bryan and Marchitto, 2008; Lowenstein and Hönisch, 2012). Cross-validation between multiple proxy types can provide greater confidence here (e.g (Martínez-Botí *et al.*, 2015; Chalk *et al.*, 2017; Raitzsch *et al.*, 2018)). Furthermore, palaeoclimate studies must contend with changes in topography, surface vegetation, ice cover, and continental configuration, records of which may be poorly constrained (Markwick, 2007; Sømme, Helland-Hansen and Granjeon, 2009; Farnsworth *et al.*, 2019).

Estimates of climate sensitivity from the palaeoclimate record generally confirm the IPCC's range but establish that the state-dependency is such that estimates differ between cold and warm periods meaning further constraint is difficult (Rohling *et al.*, 2012b; Kutzbach *et al.*, 2013; Köhler *et al.*, 2015; Martínez-Botí *et al.*, 2015; Friedrich *et al.*, 2016; Anagnostou *et al.*, 2020; Sherwood *et al.*, 2020).

1.2.5 Combining lines of evidence

The most established and accepted method of combining multiple lines of evidence is the Bayesian statistical framework (Annan, 2015; Stevens *et al.*, 2016). The method is based on Bayes' Theorem, where the probability of an unknown value is proportional to the current knowledge of the parameter, multiplied by its likelihood to be true based on the consistency with new information (Bayes and Price, 1763; Papoulis and Saunders, 1989; Annan and Hargreaves, 2006).

This approach requires the construction of a prior distribution of possible values for climate sensitivity as a probability density function (PDF) which represents the current knowledge of the parameter (Annan and Hargreaves, 2006; Annan, 2015; Annan and Hargreaves, 2020). A likelihood filter then probabilistically constructs a posterior distribution based on consistency with other evidence (Annan, 2015; Skeie *et al.*, 2018). This updated PDF represents the current best estimate for climate sensitivity based on the available evidence. Figure 1.5 depicts how the estimated range for climate sensitivity can be further constrained by combining multiple lines of evidence.

A challenge when combining multiple lines of evidence is determining whether they are independent (Hegerl *et al.*, 2006; Knutti and Hegerl, 2008; Annan and Hargreaves, 2017; Sherwood *et al.*, 2020). If there is a significant co-dependency or mutual influence on more than one line of evidence then the calculation may be complicated, particularly if the relationship is 'reinforcing' and amplifies one or both factors (Annan and Hargreaves, 2017; Sherwood *et al.*, 2020). This can occur if multiple parameters are uncertain or erroneous and they then reinforce each other. Co-dependency errors often originate from model selection bias if, for example, observations are used to evaluate the skill of a GCM simulation (Sherwood *et al.*, 2020). Other potential co-dependencies may arise if a large proportion of a multi-model ensemble originate from the same research centre or if different models share code or biases (Annan, 2015; Annan and Hargreaves, 2017).

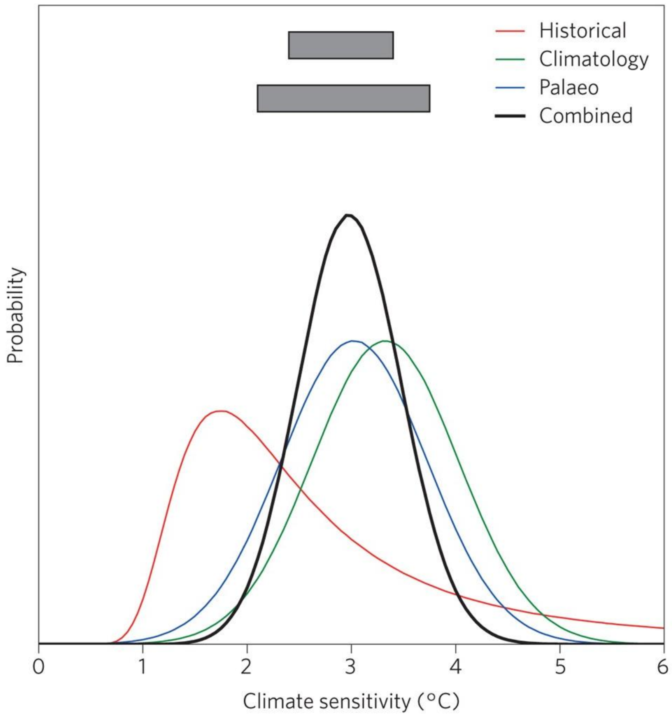

Figure 1.5: *Illustrative example of combining multiple constraints for climate sensitivity with the PDFs for the estimate from the historical climate record (red), process understanding (green), palaeoclimate (blue), and the combined estimate from all three constraints (black). Grey boxes indicate the 'likely' (66%) and 'very likely' (90%) combined ranges. From Knutti, Rugenstein and Hegerl (2017).*

1.3 Overall Methodology

1.3.1 WASP Model

1.3.1.1 Model structure

The nature of probabilistic assessment requires the use of very large ensembles of simulations to ensure coverage of the full distribution of potential values. Such ensemble sizes would be entirely impractical using a complex GCM due to the computing power and time required. This computational intensity demands that all values of climate parameters within the model are carefully chosen, in hope of producing the most accurate and likely simulations within the available run time. Therefore, complex model teams do not sufficiently systematically vary the input parameters of their models to enable a rigorous probabilistic assessment and less likely values tend to be under-sampled (Goodwin, 2021). The alternative is the use of efficient climate models that are specifically designed for the generation of large ensembles through reduced resolution and simplified complexity (Nicholls *et al.*, 2020b).

The Warming Acidification and Sea level Projector (WASP) model is an efficient 8-box model of the atmosphere-ocean-terrestrial earth system that solves for GMST rise for carbon emission scenarios, developed by my primary supervisor Dr Phil Goodwin (Goodwin, 2016;2018). Following a Bayesian statistical framework, the model generates large member ensembles using 25 input parameters that are independently varied between simulations using the Monte Carlo method. A history-matching approach is then applied to compare ensemble members (Williamson *et al.*, 2015) for agreement with specified observational constraints of GMST, ocean heat content, and carbon fluxes which act as a likelihood filter to extract posterior ensembles (Goodwin, 2018). Since its initial development (figure 1.6), WASP has been updated to include climate feedbacks that can independently vary over time for each source of forcing (Goodwin, 2018; Goodwin and Cael, 2020).

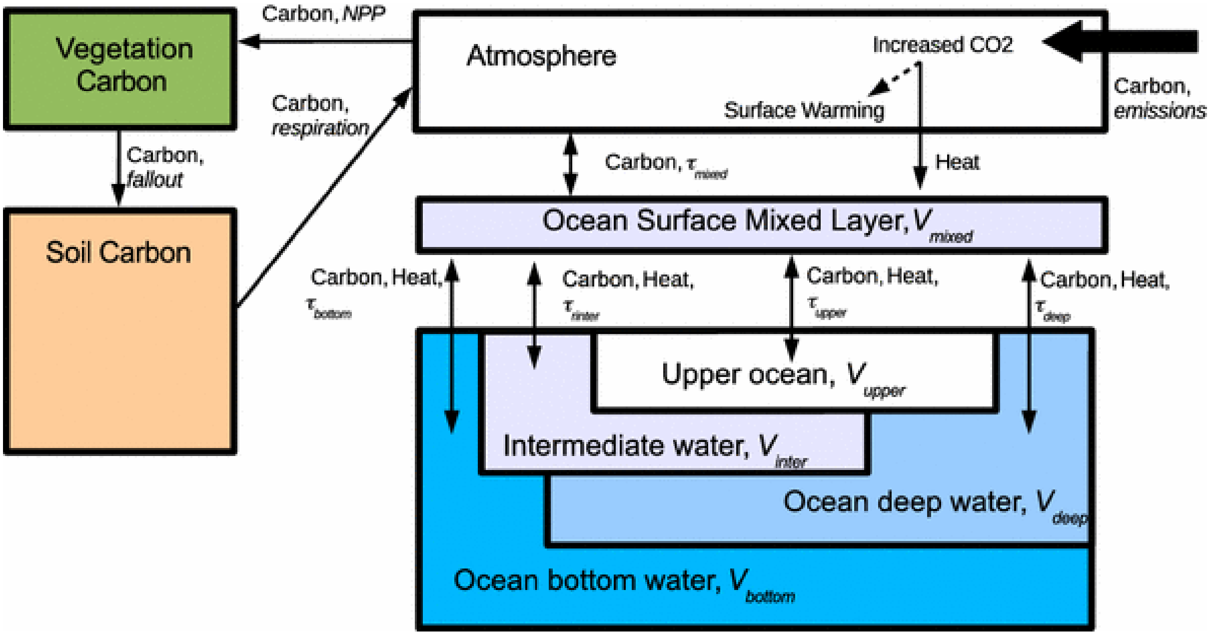

Figure 1.6: *Schematic of the WASP model. Arrows indicate carbon and heat fluxes. The ocean has prescribed e-folding timescales, τ, for tracers to equilibrate. From Goodwin, (2016).*

WASP has an advantage over previous attempts to probabilistically constrain climate sensitivity using a Bayesian framework (e.g. (Sherwood *et al.*, 2020)) as it is able to generate future climate projections that are consistent with its constrained estimate of climate sensitivity. Furthermore, WASP is far more computationally efficient than many other simple climate models as it is written in a 'compiled' computing language, C++, rather than an 'interpreted' language such as Python. This additional efficiency gives WASP the capability to generate very large member ensembles in a short period of time, thereby facilitating a more robust probabilistic assessment. The work throughout this thesis has built upon WASPv3, which uses time-evolving climate feedbacks split into three components: the instantaneous Planck feedback, λ_{Planck}, fast feedbacks, λ_{fast}, and multi-decadal feedbacks, λ_{md}, (Goodwin and

Cael, 2020). The WASP model is utilised in chapters 2 and 4, with each chapter making additional modifications and additions to the existing WASP model to study a specific research question.

1.3.1.2 Time-evolving earth system feedbacks

Equation 1.1 assumes the existence of a single overall climate feedback response to total radiative forcing. As discussed, this assumption is flawed and as such WASPv3 follows Goodwin (2018) and later work to include a time-evolving climate feedback parameter, λ, where surface warming is modelled as an extended energy balance framework in response to i sources of radiative forcing by j climate feedbacks, each operating over different response timescales (Goodwin, 2018; Goodwin and Cael, 2020). As such, the surface temperature anomaly, ΔT, at time, t, is calculated as follows:

$$\Delta T(t) = \left(1 - \frac{N(t)}{F_{total}(t)}\right) \sum_i \left[\frac{F_i(t)}{\lambda_{Planck} + \sum_j \lambda_{i,j}(t)}\right]$$

Equation 1.3

Where $\lambda_{i,j}$ is the summative combination of λ_{fast} and λ_{md} in response to i sources of radiative forcing. In WASP, the response timescale of λ_{Planck} is instantaneous. The fast feedbacks, λ_{fast}, include feedbacks operating on response timescales of water vapour residence in the atmosphere, and include clouds and water vapour-lapse rate. The response timescale of λ_{fast} varies between simulations with a random normal distribution of 8.9 ± 0.4 days following van der Ent and Tuinenburg (2017). Also considered a fast feedback, the snow and sea ice albedo feedback functionally operates in WASP as a separate term with a timescale that varies between simulations according to a uniform prior distribution between 0.5 and 1.5 years. The multi-decadal feedbacks, λ_{md}, include feedbacks that operate on the timescale of the sea surface temperature (SST) warming pattern adjustment. In WASP, the response timescale of λ_{md} varies between simulations according to a uniform prior distribution from 20 to 45 years; the minimum limit follows (Andrews, Gregory and Webb, 2015) and the maximum limit follows (Fine *et al.*, 2017). The i sources of radiative forcing in equation 1.3 include: atmospheric CO_2 forcing after (IPCC, 2013); combined forcing from well-mixed greenhouse gases (GHGs) after (Etminan *et al.*, 2016); combined anthropogenic aerosol forcing after (Myhre *et al.*, 2013a; Smith *et al.*, 2018); volcanic aerosol forcing from (Gregory *et al.*, 2016; Nicholls *et al.*, 2020a); solar forcing; and internal variability with imposed first order autoregressive noise following (Trenberth, Fasullo and Balmaseda, 2014).

The climate feedback response behaves differently in the model depending on whether the radiative forcing from source i is increasing in magnitude between two time steps, $t + \delta t$

(Goodwin and Cael, 2020). When radiative forcing from source i is increasing in magnitude, $|F_i(t+\delta t)| > |F_i(t)|$, the climate feedback, $\lambda_{i,j}$ evolves from t to $t + \delta t$ according to:

$$\lambda_{i,j}(t+\delta t) = \left|\frac{F_i(t)}{F_i(t+\delta t)}\right| \left(\lambda_{i.j}(t) + \left(\lambda_j^{equil} - \lambda_{i.j}(t)\right) \left(1 - exp\left(\frac{-\delta t}{\tau_j}\right)\right)\right)$$

Equation 1.4

On the other hand, when the radiative forcing from source i is not increasing in magnitude, $|F_i(t+\delta t)| \leq |F_i(t)|$, the climate feedback, $\lambda_{i,j}$ evolves over time according to:

$$\lambda_{i,j}(t+\delta t) = \lambda_{i,j}(t) + \left(\lambda_j^{equil} - \lambda_{i,j}(t)\right) \left(1 - exp\left(\frac{-\delta t}{\tau_j}\right)\right)$$

Equation 1.5

Consequently, the response of climate feedbacks in the model evolves over the e-folding response timescales, τ_j towards equilibrium such that at any given point in time λ can have a different value for each source of radiative forcing (Goodwin, 2018; Goodwin and Cael, 2020).

1.3.1.3 Bayesian statistical framework

The WASP model ensembles are built upon a Bayesian statistical framework and as such utilise Bayes' Theorem to calculate the posterior probability that the climate feedback parameter, and therefore climate sensitivity, has a specific set of values, X', given background information, I, and observations of the climate system, $\{obs\}$, according to the following:

$$prob(X = X'|\{obs\}, I) \propto prob(\{obs\}|X = X', I) \times prob(X = X'|I)$$

Equation 1.6

Where $prob(X = X'|I)$ is the prior probability that $X = X'$ for a given climate parameter, and $prob(\{obs\}|X = X', I)$ is the likelihood function which gives the probability of obtaining the observations, $\{obs\}$, given the value of the parameter, $X = X'$, and background information, I. The prior ensemble is generated such that the relative frequencies of model parameter values match the prior knowledge for each parameter, $prob(X = X'|I)$. The prior ensemble assumes each different parameter has a value that is independent of all other parameter's values (for example the value of fast climate feedback is independent of the value of multi-decadal climate feedback in the prior ensemble).

In WASP, the prior ensembles are not assumed to be uniform and in the case of λ, a translated lognormal distribution is adopted with three choices to set: the distribution's minimum value, median value, and uncertainty. In this way, for the j^th^ climate feedback term, the prior distribution is given as follows:

$$\lambda_j \sim Lognormal\left(ln\left(\mu_j - \lambda_{j:min}\right), ln\left(1 + \frac{\sigma_j^2}{\left(\mu_j - \lambda_{j:min}\right)^2}\right)\right) + \lambda_{j:min}$$

Equation 1.7

Where $\lambda_{j:min}$ is the minimum value that the j^th^ climate feedback can take, $\mu_j - \lambda_{j:min}$ is the difference between the distribution's median and minimum values, and σ_j^2 is the variance. This study uses the same equations for its prior distributions as Goodwin (2021) and as such, for the Planck feedback, assumes a median value of 3.3 and an uncertainty of 0.1. This gives the following equation for the prior probability distribution for λ_{Planck}:

$$\lambda_{\text{Planck}} \sim \text{Lognormal}\left(\ln 3.3, \ln\left(1 + \frac{0.1^2}{3.3^2}\right)\right)$$

Equation 1.8

WASP adopts a position of ignorance when approaching the prior distributions of the fast and multi-decadal feedbacks so that there is an assumed equal likelihood of these feedbacks being amplifying or damping. WASP also assumes that climate feedbacks are stable for all timescales meaning that λ_{total} must be negative. For this to be the case for the fast feedbacks, the sum of λ_{Planck} and λ_{fast} must therefore be negative, meaning that the minimum value of the distribution is equal to minus the Planck Feedback, whilst the median value must be equal to 0. The uncertainty is assumed to be equal to the difference between the median and minimum values. This gives an equation for the prior probability distribution of fast feedbacks as follows:

$$\lambda_{fast} \sim Lognormal(ln\lambda_{Planck}, ln2) - \lambda_{Planck}$$

Equation 1.9

The same arguments are applied to multi-decadal feedbacks, meaning that the sum of λ_{Planck}, λ_{fast}, and λ_{md} must be negative. Again, no assumption is made here as to whether the multi-decadal feedbacks are amplifying or damping, and the uncertainty scales with the difference between the median and minimum values of the distribution. As such, the prior probability distribution for multi-decadal feedbacks is calculated as follows:

$$\lambda_{\text{md}} \sim \text{Lognormal}(\ln(\lambda_{\text{Planck}} + \lambda_{\text{fast}}), \ln 2) - (\lambda_{\text{Planck}} + \lambda_{\text{fast}})$$

Equation 1.10

In this way, fast and multi-decadal feedbacks are directly related to the magnitude of the Planck feedback in each WASP simulation.

To run WASP, the model code is submitted as a job to IRIDIS5 High Performing Computing Cluster based at the University of Southampton. For each run, the model generates a large Monte Carlo prior ensemble of a specified number of simulations with 25 independently varied input parameters (Baez and Tweed, 2013; Kroese *et al.*, 2014). These parameters are detailed in appendix A. The method used to extract a posterior ensemble varies between work packages.

1.3.2 Energy balance model

Chapter 4 utilises an energy balance model (EBM) introduced in Goodwin and Williams (2023) with some adjustments. The basic methodology of the published EBM shall be described here for clarity and background understanding, with further detail in the original publication, whilst chapter 4 shall cover the adjustments and methods relevant to its specific research question.

The magnitude of Earth's total climate feedback parameter, λ_{total} (Wm^{-2}K^{-1}), is typically calculated using temporal changes in global temperature and energy balance such that:

$$\lambda_{total} = \frac{\Delta(S_{out} + L_{out})}{\Delta T}$$

Equation 1.11

Where $\Delta(S_{out} + L_{out})$ is the total change in the outgoing shortwave and longwave radiation at the TOA (Wm^{-2}) over a given time interval, and ΔT is the global surface temperature anomaly (K). Goodwin and Williams note that whilst this equation holds for global assessments of Earth's energy balance, it must be extended to consider how the vertical radiation balance and horizontal heat transport may differ by latitude when assessing zonal variations in λ_{total} and temperature. The EBM solves for zonal- and annual-mean surface temperature for *i* = 36 discrete horizontal horizons, spaced from -87.5° to 87.5°, giving a resolution of 5° latitudinal bands.

For the vertical radiation balance at a given latitude, the outgoing radiation at the TOA, R_{out} (Wm^{-2}), is given by:

$$R_{out}\,(\phi) = L_{out}(\phi) + S_{out}(\phi) = \varepsilon(\phi)\sigma T_s^4(\phi) + \alpha(\phi)R_{solar}(\phi)$$

Equation 1.12

Where ϕ is the latitude; L_{out} is the outgoing longwave radiation at the TOA; S_{out} is the outgoing shortwave radiation at the TOA; ε is the local planetary emissivity, accounting for both the surface emissivity and the atmospheric greenhouse effect; σ is the Stephan-Boltzmann constant (Wm^{-2}K^{-4}); T_s is the local surface temperature (K); α is the local albedo; and R_{solar} is the local incoming solar radiation (Wm^{-2}). All variables are the zonal mean for the specified latitudinal band. The zonal-mean net heat uptake, $\mathcal{H}$ (Wm^{-2}), for a specified latitudinal band, per unit area per unit time for a steady state is then calculated as follows:

$$\mathcal{H}(\phi) = c(\phi)\frac{dT_s}{dt}(\phi) = R_{solar}(\phi) - \frac{\delta f}{\delta y}(\phi) - R_{out}(\phi)$$

Equation 1.13

Where ϕ is the latitude; c is the heat capacity (Jm^{-2}k^{-1}); $\frac{dT_s}{dt}$ is the rate of warming (Ks^{-1}); R_{out} is the TOA outgoing radiation (Wm^{-2}), R_{solar} is the local incoming solar radiation (Wm^{-2}), and $-\frac{\delta f}{\delta y}$ is the meridional convergence in the mean poleward heat transport (Wm^{-2}). At a steady state, the surface temperature, T_s, stabilises so that $\mathcal{H}(\phi) = 0$.

To represent horizontal heat transport, the EBM utilises the horizontal gradient in surface temperature, T_s, to diffuse heat horizontally via some effective diffusivity, $\kappa_{eff}(\phi)$ (WK^{-1}m^{-1}) so that:

$$f(\phi) = -\kappa_{eff}(\phi)\frac{\delta T_s}{\delta y}(\phi)$$

Equation 1.14

Where $f(\phi)$is the poleward heat transport across a line of latitude per unit latitudinal length in Wm^{-1}, and y is the poleward displacement in m. $f(\phi)$ is the total additive combination of heat transport through: dry-static air, $f_{dry}(\phi)$, latent heat within air, $f_{latent}(\phi)$, and ocean heat transport, $f_{ocean}(\phi)$. Therefore, equation 1.14 can be expanded so that:

$$f(\phi) = f_{dry}(\phi) + f_{latent}(\phi) + f_{ocean}(\phi) = -\left[\kappa_{dry}(\phi) + \kappa_{latent}(\phi) + \kappa_{ocean}(\phi)\right]\frac{\delta T_s}{\delta y}(\phi)$$

Equation 1.15

Where $\kappa_{dry}(\phi)$, $\kappa_{latent}(\phi)$, and $\kappa_{ocean}(\phi)$ represent the dry static diffusivity, latent heat diffusivity, and ocean diffusivity respectively. This is useful because the dominant medium through which poleward heat transport takes place will vary between regions. In particular, the latent heat diffusivity varies with specific humidity.

Meanwhile, the EBM also considers the thermodynamic processes that may influence the effective horizontal diffusivity. To reflect the fact that effective diffusivity is affected by local surface temperature, T_s, the above equation 1.14 is differentiated to give:

$$\frac{\delta f}{\delta y}(\phi) = -\frac{\delta}{\delta y}\left[\kappa_{eff}(\phi)\frac{\delta T_s}{\delta y}(\phi)\right]$$

Equation 1.16

Where $\frac{\delta f}{\delta y}(\phi)$ is the horizontal heat flux divergence.

A positive radiative forcing, δF (Wm^{-2}), occurs when there is a net increase in incoming radiation at the TOA, which can arise either through an increase in incoming solar radiation, R_{solar}, or a decrease in outgoing radiation, R_{out}, whilst the Earth's surface temperature remains unchanged. A negative radiative forcing occurs in the opposite case when there is a net decrease in the incoming radiation at the TOA (or a net increase in the TOA outgoing radiation). Either perturbation will force a latitudinal radiative response within the model where surface temperatures will change to the point at which a new steady state is reached. Following a perturbation, equation 1.13 is adjusted to account for the changing surface temperatures and change in horizontal heat flux, each of which will vary by latitude. The radiative forcing with latitude is then calculated as follows:

$$\delta F(\phi) = \delta R_{out|\delta T_s}(\phi) - \delta\left[\frac{\delta f}{\delta y}\right](\phi) = \frac{\delta R_{out}}{\delta T_s}(\phi)\delta T_s(\phi) - \delta\left[\frac{\delta f}{\delta y}\right](\phi)$$

Equation 4.17

Where $\delta R_{out|\delta T_s}$ is the vertical radiative response from changing surface temperatures; and $\delta\left[\frac{\delta f}{\delta y}\right](\phi)$ is the change in horizontal heat flux. $\frac{\delta R_{out}}{\delta T_s}$ (Wm^{-2}K^{-1}) is equal to the change in outgoing radiation per unit of temperature change at a specific latitude and is therefore equivalent to the local latitudinal value of the effective climate feedback parameter, λ_ϕ (Wm^{-2}K^{-1}).

As illustrated in figure 1.7, the EBM solves for the steady state zonal- and annual-mean surface temperature, T_s (K), with latitude, ϕ, for: imposed zonal- and annual-mean incoming solar radiation with latitude, R_{solar} (Wm^{-2}); parameterised heat transport with imposed horizontal effective diffusivity with latitude, $\kappa_{eff}(\phi)$ (WK^{-1}m^{-1}); and imposed cloudiness with latitude where $f_{CA}(\phi)$ is the cloud amount fraction and $f_{CI}(\phi)$ is zonal- and annual-mean fraction of incoming shortwave radiation that is incident on clouds. Note that $f_{CA}(\phi)$and $f_{CI}(\phi)$differ due to the sub-annual variation in incoming radiation and cloudiness.

Whilst the WASP model incorporates time-evolving earth system feedbacks, the EBM is concerned with latitudinally-varying feedbacks. The use of both models, therefore, serves to address both the temporal and spatial heterogeneity of Earth's complex climate feedbacks.

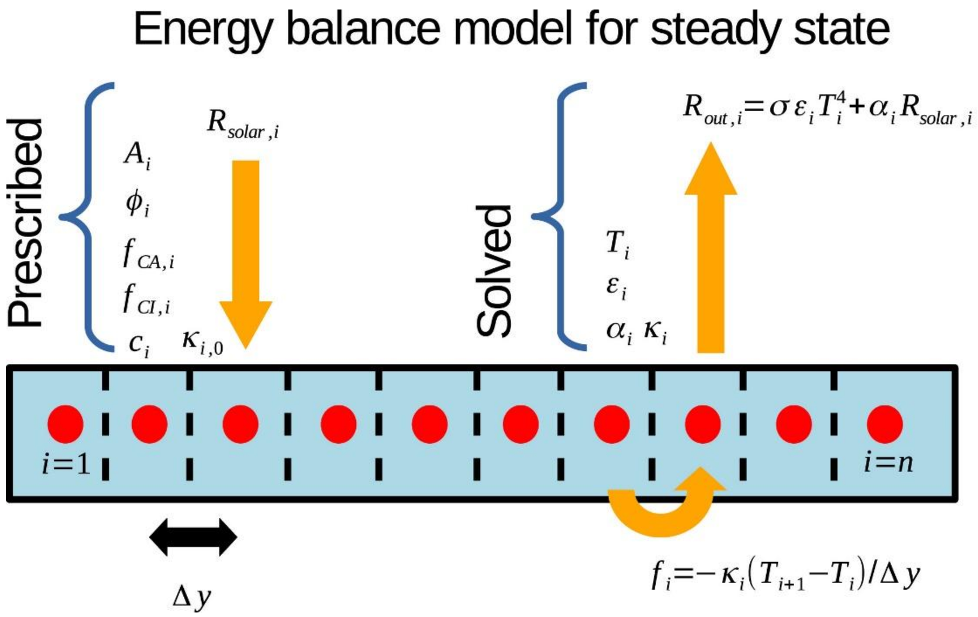

Figure 1.7: *Schematic of the conceptual energy balance model at a steady state, developed by Goodwin and Williams (2023). Here the letter i denotes the prescribed sky condition, that can be changed in the model to represent either: entirely clear sky conditions (where cloud fraction amount is 0); entirely cloudy sky (where cloud fraction amount is 1); or 'all sky' conditions where the cloud fraction amount is determined by prescribed observed climatology.*

1.4 Outline

The central focus of this thesis is to explore and quantify the behaviour of Earth's climate feedbacks in the context of the past, present, and future. All chapters shall therefore serve to contribute to this aim and narrative. This thesis is structured around the following three objectives:

Objective 1:

Constrain the magnitude of Earth's fast and multi-decadal feedbacks and quantify the pattern effect through probabilistic assessment

Objective 2:

Explore and constrain the magnitude of Earth's slow ice sheet-albedo feedback in the context of the most recent deglaciation

Objective 3:

Investigate Earth's climate feedbacks under different background mean climate states and explore the implications of the ice sheet-albedo feedback for long term climate change

These three objectives form the basis of the central chapters of this thesis: Objective 1 is addressed in Chapter 2; Objective 2 is tackled in Chapter 3; and Objective 3 is investigated in Chapter 4. In Chapter 2, a new forced temperature profile extracted from the HadCRUT5 observational dataset is utilised for the first time to act as an observational constraint on the magnitude of multi-decadal feedbacks. Of all chapters, Chapter 2 focuses most heavily on the improvement of the statistical methodology used to constrain climate feedbacks, and three methodological variations are compared to highlight the benefits of each method. Chapter 3 investigates the currently underrepresented slow feedbacks and uses a proxy data-driven approach to quantify both the magnitude and timescale of the ice sheet-albedo feedback since the LGM. Finally, Chapter 4 investigates the relationship between the background climatic mean state and the total climate feedback parameter and further incorporates the findings of Chapter 3 to explore projections of long-term warming under multiple scenarios. Chapter 5 summarises and collates the findings of all chapters and discusses the implications for international climate policy as well as potential future research directions.

Chapter 2 Fast & multi-decadal feedbacks

2.1 Introduction

The magnitude of Earth's countless climate feedbacks continues to cause considerable uncertainty in the prediction of future climate change, greatly hindering our capacity to construct effective adaptation and mitigation strategies for the coming decades. A large proportion of this uncertainty stems from incomplete understanding of Earth's feedbacks which each operate on differing response timescales (Zeebe, 2013; Knutti and Rugenstein, 2015; Pfister and Stocker, 2017; Goodwin, 2018; Chao and Dessler, 2021).

The strength of Earth's climate feedbacks is quantified by the total climate feedback parameter, λ_{total} ($Wm^{-2}K^{-1}$), which is defined here as the change in outgoing radiation at the top of the atmosphere (TOA) per unit of temperature change. λ_{total} at time, t, is calculated as follows:

$$\lambda_{total}(t) = \frac{N(t) - F_{total}(t)}{\Delta T(t)}$$

Equation 2.1

Where N is the net TOA energy imbalance (Wm^{-2}), F_{total} is the total radiative forcing (Wm^{-2}), and ΔT is the global surface temperature anomaly (K). The total climate feedback parameter is considered the sum of multiple terms such that $\lambda_{total}(t) = \sum \lambda_i$ with i denoting the specific feedback. I follow the sign convention that positive λ_i terms climate feedback values amplify future warming.

The spatial and temporal heterogeneity of Earth's feedbacks contribute towards the 'pattern effect', the magnitude of which greatly affects both how climate sensitivity evolves over time and the magnitude of future warming (Rose *et al.*, 2014; Armour, 2017; Andrews *et al.*, 2018; Dessler, 2020; Dong *et al.*, 2020; Chao, Muller and Dessler, 2022). The pattern effect is primarily driven by feedbacks that operate on multi-decadal timescales which demonstrate a significant spread in magnitude across the complex model ensembles of CMIP5 and CMIP6: while the majority of complex models find the pattern effect will amplify future warming some complex models instead show dampening (Andrews, Gregory and Webb, 2015; Dong *et al.*, 2020).

This chapter builds on the findings of both Goodwin (2021) and Goodwin & Cael (2020) who used a combination of observational constraints on GMST and ocean heat content (OHC) anomalies to act as likelihood filters in a probabilistic assessment of Earth's feedbacks. They found two peaks in the posterior probability distributions of the fast and multi-decadal feedbacks as shown in figure 2.1, suggesting that there are two observationally consistent regions corresponding to either: weak amplifying fast feedbacks (~ 0.6 Wm^{-2}) and strong amplifying multi-decadal feedbacks (~ 1.7 Wm^{-2}); or very strong amplifying fast feedbacks (~ 2.2 Wm^{-2}) and damping multi-decadal feedbacks (~ -1.0 Wm^{-2}) (Goodwin and Cael, 2020).

The aim here is to constrain the magnitude of Earth's multi-decadal feedbacks through a probabilistic assessment to determine whether multi-decadal feedbacks have an amplifying or damping effect on climate sensitivity. This gained knowledge will be used to quantify the strength of the pattern effect as a result of multi-decadal feedbacks in the earth system. Furthermore, the interactive relationship between Earth's fast and multi-decadal feedbacks means that this assessment shall also improve the constraint of Earth's faster inter-annual feedbacks.

As figure 2.1 indicates, current knowledge shows that both amplifying and damping multi-decadal feedbacks are statistically plausible. However, both studies by Goodwin (2021) and Goodwin & Cael (2020) utilised 20-year averages for temperature anomalies in their probabilistic assessment to target the longer-term multi-decadal trend. While this approach determines whether simulations are observation-consistent against the overall anthropogenic warming trend, representations of rapid cooling from volcanic forcing are averaged out. This chapter shall investigate the use of 1-year averages for temperature anomalies in the likelihood function, meaning simulations must also be sufficiently similar with the observed inter-annual response to volcanic activity to be considered observation consistent. This shall enable me to determine whether multi-decadal feedbacks are amplifying or damping, according to the historical record: simulations will only be considered observation consistent if they represent both the rapid cooling response to volcanic cooling *and* the overall longer warming trend from anthropogenic forcing.

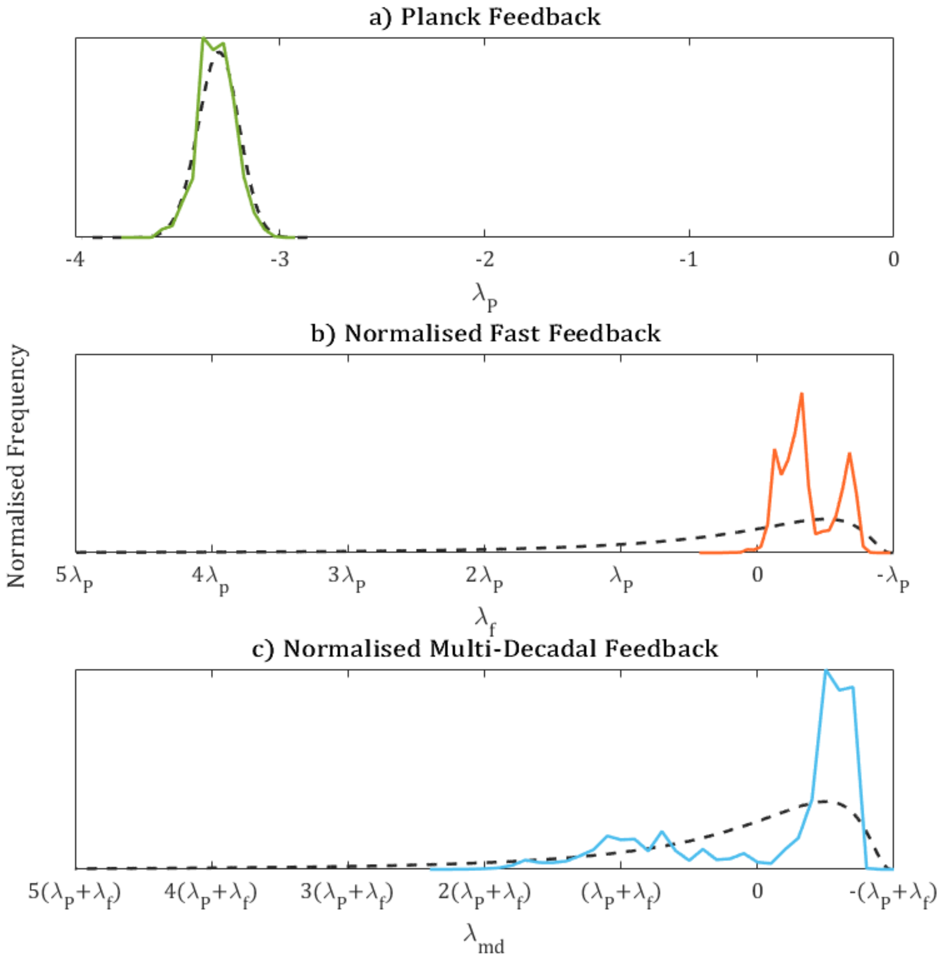

Figure 2.1: *Frequency density distributions for the prior and posterior ensembles from the study by Goodwin (2021) for* ***a****) Planck Feedback,* ***b****) fast feedbacks, and* ***c****) multi-decadal feedbacks. Coloured solid lines show the weighted posterior ensembles, and the black dashed lines show the prior ensembles. Fast feedbacks are normalised in terms of the Planck feedback. Multi-decadal feedbacks are normalised in terms of the combined effect of fast feedbacks and the Planck Feedback. Adapted from (Goodwin, 2021). Note that sign convention differs to publication.*

A challenge when evaluating a model on annual to inter-annual timescales can be the ratio of noise to the target signal as random variability can obscure key trends. I address this by utilising a new extracted forced temperature record from Cael & Calafat (in review) that extracts the annual forced temperature profile from the HadCRUT5 historical record by removing natural variability but leaving the forced signals from anthropogenic and natural sources of radiative forcing. The model simulations can thereby be compared directly to the desired forced signal to evaluate model skill and further constrain the magnitude of Earth's feedbacks.

2.2 Methodology

The underlying statistical framework and numerical model used in this work are described in detail in section 1.3.1 of Chapter 1. This section shall describe the methodology specifically relevant to this chapter. In order to demonstrate the comparative benefit of using 1-year averages to extract the posterior ensemble, I also repeat the method used by Goodwin (2021) and Goodwin & Cael (2020) who used 20-year averages to extract the posterior ensemble. This serves to facilitate a direct comparison between the two methods. In addition to varying the timescale of comparison, I investigate the effect of two different statistical methods of likelihood filter on the resultant posterior ensemble, namely a cost function and a multivariate likelihood function. Together, these investigations cumulate in 3 experimental methods: 20-year averages and a cost function; 1-year averages and a cost function; and 1-year averages and a multivariate likelihood function. In all experiments the prior ensemble in WASP runs from 1850 to 2020 (171 times 12 monthly time steps), simulating the historical period.

2.2.1 Method 1: 20-year averages

For Method 1, the WASP model is used to generate a Monte Carlo prior ensemble of 16 million simulations. The likelihood filter used to extract the posterior ensemble for method 1 is comprised of an OHC constraint from (Cheng *et al.*, 2017) and an observed temperature constraint from the HadCRUT5 dataset (Morice *et al.*, 2021). Each WASP simulation is split into 20-year averaged periods from 1900 to present, each relative to the 1850-1900 period. The same method is applied to the HadCRUT5 observational dataset and compared to each simulation in 20-year sections. Both HadCRUT5 and the WASP simulations are normalised to the 1850 - 1900 period to facilitate direct comparison between the two.

In this statistical framework, ensemble members are selected for the posterior ensemble according to consistency with observational evidence. In this case, the relative success of each simulation in reproducing the observational record is determined by a cost function that compares temperature and OHC to the imposed constraints. The cost function for each 20-year section of each ensemble member is calculated assuming Gaussian uncertainty:

$$cost\ function\ =\ e^{-(\mu-x)^2/2\sigma^2}$$

Equation 2.2

Where μ is the observational best estimate, σ is the observational standard deviation, and x is the simulated value. The overall cost function for each ensemble members is calculated as the product of all sections of the temperature time series, combined with the OHC constraint.

If the overall cost function of each ensemble member is greater than a prescribed automatic acceptance limit, set at 5.0×10^{-8} for this experiment, then the ensemble member is accepted into the posterior ensemble and weighted by the ratio of the cost function to the automatic acceptance limit. Otherwise, the ensemble member is either rejected or accepted with a weighting of 1 if the cost function was greater than a random number between 0 and the automatic acceptance limit. Method 1 generates a posterior ensemble of 8834 simulations. Ensemble members are then sorted into percentiles for analysis.

2.2.2 Method 2: 1-year averages

In order to target the forced signal when comparing WASP simulations to the observational record at an inter-annual timescale, random noise must be ignored and as such WASP is run without prescribed internal variability. For Method 2, the WASP model is used to generate a prior ensemble of 20 million simulations.

The likelihood filter for Method 2 is comprised of an OHC constraint from (Cheng *et al.*, 2017) and a new forced temperature record that extracts the annual forced anthropogenic temperature profile from the HadCRUT5 historical record by removing natural variability (Cael and Calafat, in review; Calafat and Cael, Submitted). Both the forced temperature constraint and the WASP simulations are normalised to the 1850 - 1900 period to facilitate direct comparison between the two.

In order to extract the forced signal, Cael and Calafat utilise a Bayesian hierarchical energy balance model with historical time series of GMST, radiative forcing, OHC, and the ENSO Index. GMST anomalies spanning 1850-2020 and associated uncertainties are taken from the HadCRUT5 dataset (Morice *et al.*, 2021); the reconstruction of OHC change for 1870-2018 is from (Zanna *et al.*, 2019); the time series and uncertainties of the ENSO index for 1850-2020 are from the Ensemble Oceanic Niño Index (Webb and Magi, 2022); and the ensemble of radiative forcing time series is from (Smith *et al.*, 2021). The Bayesian hierarchical model used to extract the forced temperature response has three levels:

1) Data model: a probability model that describes the distributions of GMST, OHC, and ENSO index,
2) Process model: a probability model that describes the dynamics of the latent processes, conditional on a set of parameters,
3) Parameter model: a prior distribution that describes the uncertainty in the model parameters and encodes the prior knowledge about the processes and parameters.

As such, the posterior distributions are proportional to the product of the three levels that form the hierarchy. Next, I shall describe how individual processes and uncertainties are modelled in this framework developed by Cael and Calafat. Firstly, the data model for the temperature observations can be written as:

$$y_t = \Delta T_t + m + \epsilon_{y,t}, \qquad t = 1, \dots, T$$

Equation 2.3

Where y_t is the global surface temperature observation at year t, ΔT_t is the true latent process, m is an unknown offset, and $\epsilon_{y,t}$ is a zero-mean Gaussian observation error with standard deviation equal to the standard errors provided by HadCRUT5, which vary from year to year (Morice *et al.*, 2021).

Reconstructed changes in ocean heat content, OHC_t^{Rec}, are modelled as a noisy version of the true process, OHC_t:

$$OHC_t^{Rec} = OHC_t + \epsilon_{OHC,t}$$

Equation 2.4

Where $\epsilon_{OHC,t}$ is a zero-mean Gaussian data error with time-varying standard deviation set equal to the standard errors provided in the historical OHC reconstruction by (Zanna *et al.*, 2019).

To capture variability in ΔT_t associated with the El Niño-Southern Oscillation, Cael and Calafat use an observation-based ENSO index, $x_{ENSO,t}^{Obs}$, which is modelled as a noisy version of the true ENSO index, $x_{ENSO,t}$:

$$x_{ENSO,t}^{Obs} = x_{ENSO,t} + \epsilon_{ENSO,t}$$

Equation 2.5

Where, like in equation 2.4, $\epsilon_{ENSO,t}$ is a zero-mean Gaussian data error with time-varying standard deviation equal to the standard errors provided by the data (Webb and Magi, 2022).

The latent process, ΔT_t, in response to radiative forcing, $\Delta T_{F,t}$, is modelled as follows:

$$c\frac{d\Delta T_{F,t}}{dt} = F_t - \lambda_t \Delta T_{F,t} - H_t$$

Equation 2.6

Where F_t is the radiative forcing at time t, λ_t is the climate feedback parameter at time t, and c is the heat capacity of the surface layer in Jm^{-2}K^{-1}. H_t is equal to $\frac{dOHC_t}{dt}$ and, therefore, represents the tendency of the true OHC at time t. The radiative forcing at time t, F_t, is modelled as:

$$F_t \sim N(\mu_{F,t}, \Sigma_F)$$

Equation 2.7

Where $\mu_{F,t}$ is the mean and $\Sigma_F$is the temporal covariance matrix extracted from the ensemble of radiative forcing data (Smith *et al.*, 2021).

Rather than assuming a constant or linear evolution over time, the climate feedback parameter, λ_t, is modelled as a non-parametric process and is assumed to follow a random walk:

$$\lambda_t = \lambda_{t-1} + \epsilon_{\lambda,t}$$

Equation 2.8

Where $\epsilon_{\lambda,t}$ is Gaussian white noise with unknown standard deviation, σ_λ. The initial value of the climate feedback parameter, λ_0, is given by a truncated normal prior $TN(1{,}0.4)[0,\infty]$ following (Andrews *et al.*, 2018).

Meanwhile, the ENSO index is assumed to follow a zero-mean AR1 process:

$$x_{ENSO,t} = \phi_{ENSO} x_{ENSO,t-1} + \epsilon_{ENSO,t}$$

Equation 2.9

Where ϕ_{ENSO} is the AR1 autocorrelation coefficient for the ENSO index and $\epsilon_{ENSO,t}$ is Gaussian white noise with unknown standard deviation, σ_{ENSO}. The effect of ENSO on ΔT, $\Delta T_{I,t}^{ENSO}$, is given by the linear regression:

$$\Delta T_{I,t}^{ENSO} = \beta x_{ENSO,t}$$

Equation 2.10

Where β is the regression coefficient associated with the true ENSO index, $x_{ENSO,t}$. Internal variability that is unrelated to ENSO is captured as a residual term, $\Delta T_{I,t}^{Res}$, that is modelled as an AR1 process:

$$\Delta T_{I,t}^{Res} = \phi_{Res} \Delta T_{I,t-1}^{Res} + \epsilon_{I,t}$$

Equation 2.11

Where ϕ_{Res} is the AR1 autocorrelation coefficient and $\epsilon_{I,t}$ is Gaussian white noise with unknown standard deviation, σ_I.

Finally, reconstructed OHC changes exhibit weak variability with large longer-term changes (Zanna *et al.*, 2019) and, thus, is modelled as following a random walk:

$$H_{t-1} = H_t - \epsilon_{OHC,t}$$

Equation 2.12

$$OHC_t = OHC_{t-1} + H_{t-1}$$

Equation 2.13

Where $\epsilon_{OHC,t}$ is Gaussian white noise with unknown standard deviation, σ_{OHC}. The initial values of OHC_t and H_t are unknown and are modelled with imposed prior distributions.

Using this model, Cael and Calafat separate the forced component of GMST change from natural internal variability and random noise within observations. Their estimates offer an improvement on other published records as their Bayesian hierarchical approach allows them to represent and propagate uncertainty in a more statistically rigorous way. The statistical framework accounts for uncertainty in both the observational data and model uncertainty relating to the underlying equations governing the evolution of model variables. As such, the model yields more realistic estimates of uncertainty and more accurate estimates of modelled variables, including the forced temperature response. Cael and Calafat's forced record is generated independently from WASP and so introduces no circularity when incorporated into the likelihood filter of Methods 2 and 3 of this Chapter.

As in Method 1, the relative success of each simulation in reproducing the observational record is determined by a cost function (equation 2.2) that compares temperature and OHC to the imposed constraints. Due to computer memory capacity concerning the memory allocated to floating point numbers, I am unable to calculate the overall cost function for each ensemble member as a product of the cost functions of all time steps as the small values cause the overall probability to functionally go to zero. Therefore, the time series is split into 10 sections of 17 years each, multiplying the cost functions within each section and taking the 17th root to give each section an equivalent weighting of 1. The overall cost function for each ensemble member is then the product of each section, combined with the OHC constraint.

If the cost function is greater than a prescribed automatic acceptance limit, set at 1.0x10^{-10} for this experiment, then the ensemble member is accepted into the posterior ensemble and weighted by the ratio of the cost function to the automatic acceptance limit. Otherwise, the ensemble member is either rejected or accepted with a weighting of 1 if the cost function was greater than a random number between 0 and the automatic acceptance limit. Method 2 generates a posterior ensemble of 18848 simulations. Ensemble members are then sorted into percentiles for analysis, in the same manner as Method 1.

A limitation of the cost function method is the assumption that individual years are independent from each other, which does not represent reality. Method 3, therefore, attempts to rectify this.

2.2.3 Method 3: Multivariate likelihood function

As in Method 2, the likelihood filter for Method 3 utilises an OHC constraint from (Cheng *et al.*, 2017) and the new forced temperature record (Cael and Calafat, in review). As individual years cannot realistically be assumed to be independent from each other, I investigate a new likelihood function that incorporates first order autocorrelation via means of a covariance matrix, Σ, constructed using posterior samples from the observational time series of Cael and Calafat (in review). Diagonal elements of Σ give the variance within individual time steps across the posterior ensemble and off-diagonal elements give the covariances between time steps. The relative success of each simulation is therefore determined at each time step by the probability density function (PDF) of the multivariate normal distribution at a given point on a d-dimensional space on which the multivariate distribution is defined, given by the following equation:

$$f(x, \mu, \Sigma) = \frac{1}{\sqrt{|\Sigma|(2\pi)^d}} \exp\left(-\frac{1}{2}(x-\mu)\Sigma^{-1}(x-\mu)'\right)$$

Equation 2.14

Where x is the simulated value and μ is the observational best estimate, both 1 x d vectors, and Σ is the d x d covariance matrix. The multivariate normal distribution is a generalisation of the univariate normal distribution to two or more variables. Its two parameters, the mean vector μ and a covariance matrix Σ, are analogous to the mean and variance parameters of a univariate normal distribution.

This method creates computational challenges as the 171-year time series requires a very large covariance matrix of size 171x171. Therefore, when calculating the relative success of a simulation at each timestep the probability can functionally go to infinity or zero due to the presence of very large and very small numbers that go beyond the memory capacity of most standard analysis tools. This numerical instability means that members of the posterior ensemble from Method 3 cannot not be weighted in the same way as Methods 1 and 2 and all ensemble members that exceeded an acceptance limit of 5.0x10^{-8} pass into the posterior ensemble with a weighting of 1. I expect this to be visible in the results. Method 3 generates a posterior ensemble of 7807 simulations from a prior ensemble of 24 million simulations, which are then sorted into percentiles for analysis.

2.3 Results

Here I present the results of the three experimental methods used to extract posterior ensembles from WASP with the aim of constraining the magnitude of Earth's climate feedbacks over multiple timescales, with an emphasis on the multi-decadal feedbacks.

For each method, the main parameters investigated consisted of annual simulated temperature anomalies from 1850 to 2020 compared to observational data; the magnitude for the total climate feedback parameter, λ_{total}, over multiple response timescales; probability density distributions of both fast, λ_{fast}, and multi-decadal, λ_{md}, feedbacks; and analysis of the relationship between λ_{fast} and λ_{md}, feedbacks in the posterior ensembles of WASP.

2.3.1 Method 1: 20-year averages

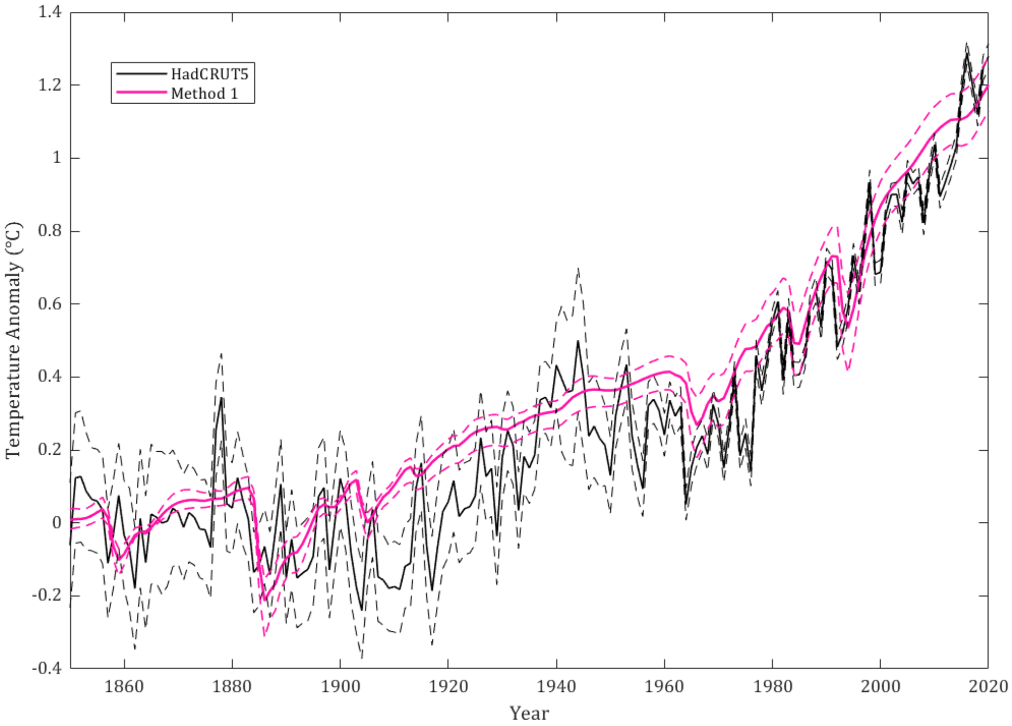

Figure 2.2: *Median annual temperature anomalies from 1850 – 2020 for the WASP posterior ensemble using Method 1 (solid pink) with 95% confidence limits (dashed pink) with 95% confidence limits (dashed pink) and the mean annual temperature anomalies from the HadCRUR5 observational dataset (solid black) with 95% confidence limits (dashed black).*

Figure 2.2 compares the simulated annual temperature anomalies from 1850 to 2020 to the HADCRUT5 observational dataset using Method 1 of likelihood filter to extract the posterior ensemble. Here WASP successfully captures the long-term multi-decadal trend recorded in the observations but fails to simulate the short-term variability. Some significant volcanic eruptions, such as the Krakatoa eruption of 1883, do appear to be captured in the WASP simulation but only to a limited extent. Overall, WASP simulates a median 1.20°C of warming since 1850, which is slightly lower than the mean observational value of 1.28°. Uncertainty is reduced in comparison to the observational dataset over the full time series, with the greatest uncertainty close to the present day where the confidence bands are ~0.16°C.

The disparity in the WASP model's ability to target the multi-decadal trend relative to the short-term trend is further evidenced in Figure 2.3c which depicts λ_{total} over a logarithmic timescale to visualise the multiple response timescales Earth's feedbacks are acting upon. On very short timescales of seconds to minutes, the primary contributor to λ_{total} is the Planck feedback and as such, remains close to -3.3 $Wm^{-2}K^{-1}$. WASP is able to capture this with a high degree of certainty, as illustrated by the narrow confidence bands. Similarly, the confidence bands narrow at the 20-year timescale, indicating a greater degree of certainty of the magnitude of λ_{total} at this timescale compared to1-year (Figure 2.3c: dotted lines). This occurs because the time-windows used in the observational constraint of the Method 1 likelihood filter are of 20-year periods.

Figures 2.3a and 2.3b show the frequency distributions for the magnitude of multi-decadal (a) and fast (b) feedbacks in the posterior ensemble of WASP, extracted using Method 1. This method yields a median estimate of -0.03 $Wm^{-2}K^{-1}$ for λ_{md} and 0.75 $Wm^{-2}K^{-1}$ for λ_{fast} suggesting that the median estimate of Earth's fast feedbacks have a greater amplifying effect than Earth's multi-decadal feedbacks. However, uncertainty is large and therefore limited information can be gleaned from the median. This method also estimates that the magnitude of Earth's multi-decadal feedbacks is in the range of -0.81 $Wm^{-2}K^{-1}$ to 0.97 $Wm^{-2}K^{-1}$ with 66% confidence and in the range of -1.25 $Wm^{-2}K^{-1}$ to 1.67 $Wm^{-2}K^{-1}$ to with 90% confidence. This is a wide range of uncertainty and gives little indication of whether multi-decadal feedbacks have an amplifying or damping effect. This is further evident in Figure 2.3c which shows no overall change in λ_{total} from a 1-year timescale to a 20-year timescale as there is similar likelihood of the multi-decadal feedbacks being amplifying as they are damping. There is less uncertainty surrounding Earth's fast feedbacks using this method with 66% confidence that the magnitude is in the range of 0.18 $Wm^{-2}K^{-1}$ to 1.22 $Wm^{-2}K^{-1}$, and the range of -0.38 $Wm^{-2}K^{-1}$ to1.43 $Wm^{-2}K^{-1}$ with 90% confidence. The frequency distribution of fast feedbacks is positively skewed towards an amplifying effect, and this is supported by the increase in λ_{total} from the timescale of days to months in figure 2.3c which represents increased amplifying.

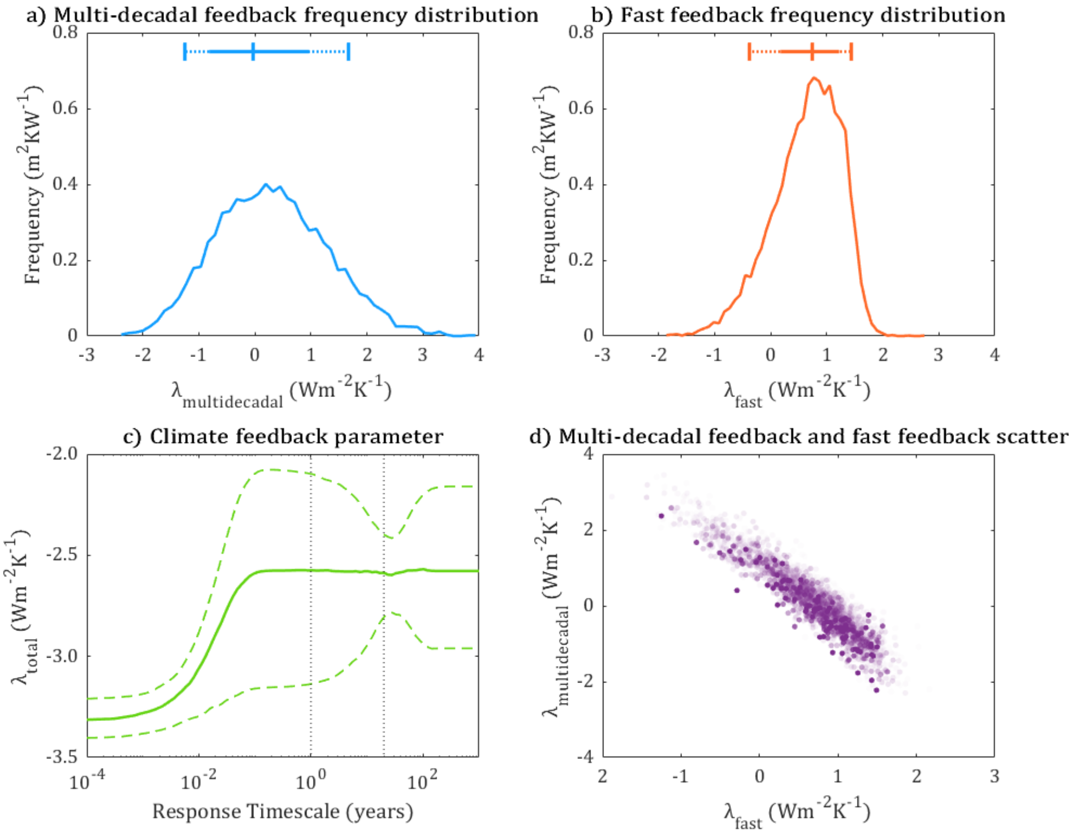

Figure 2.3: *Findings from the WASP posterior ensemble using Method1:* ***a****) Frequency distribution for the magnitude of multi-decadal feedbacks. The blue range indicates the ensemble best estimate, 66% confidence band (solid blue), and 90% confidence band (dotted blue);* ***b****) Frequency distribution for the magnitude of fast feedbacks. The orange range indicates the ensemble best estimate, 66% confidence band (solid orange), and 90% confidence band (dotted orange);* ***c****) λ_{total} over multiple response timescales. Solid green line indicates ensemble best estimate with dashed lines showing 66% confidence limits; and* ***d****) Scatter plot of fast and multi-decadal feedback values in posterior ensemble.*

Finally, figure 2.3d shows the relationship between fast and multi-decadal feedbacks in each ensemble member. Each dot represents an individual simulation, with increased opacity indicating a greater weighting and therefore closer similarity to the observational constraint. The scatter plot indicates a strong correlation between the value of fast and multi-decadal feedbacks in an individual simulation, with an R^2 value of 0.86.

2.3.2 Method 2: 1-year averages

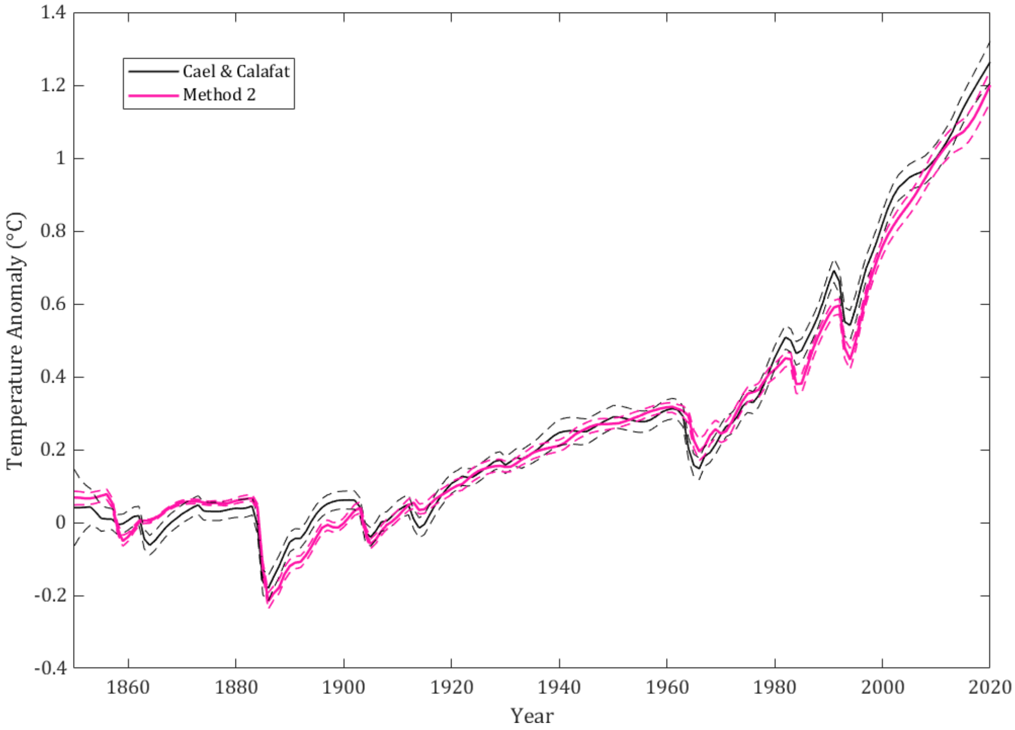

Figure 2.4: *Median annual temperature anomalies from 1850 – 2020 for the WASP posterior ensemble using Method 2 with 66% confidence limits (pink) and the mean forced temperature profile (black) from Cael & Calafat (in review) with 1σ confidence bands.*

Figure 2.4 compares the simulated annual temperature anomalies from 1850 to 2020 to the forced temperature profile extracted from the observational record by Cael and Calafat (in review). Like Method 1, this method estimates a median 1.20°C of warming since 1850, compared to 1.26°C in the forced temperature record, but the uncertainty bands are narrower throughout the time series, reaching no more than ~0.08°C even close to the present day. This method accurately captures the overall long-term temperature trend and successfully captures the inter-annual variability and response to volcanic activity with far greater skill than Method 1.

Figure 2.5a shows the frequency distribution for the magnitude of fast feedbacks in the posterior ensemble of WASP, extracted using Method 2. This method finds a median estimate of 0.88 $Wm^{-2}K^{-1}$ with a 66% confidence interval of 0.43 $Wm^{-2}K^{-1}$ to 1.23 $Wm^{-2}K^{-1}$ and a 90% confidence interval of 0.10 $Wm^{-2}K^{-1}$ to1.39 $Wm^{-2}K^{-1}$. This suggests a high likelihood that Earth's fast feedbacks have an amplifying effect.

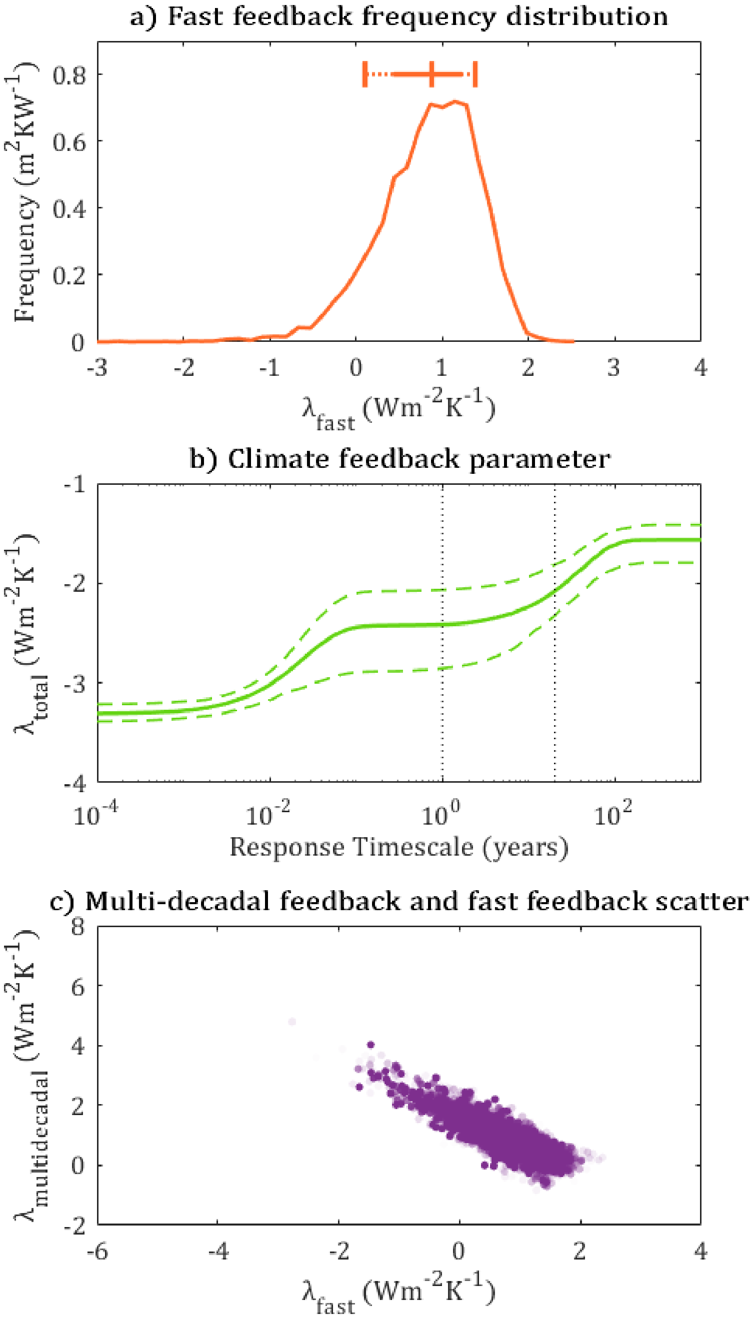

Figure 2.5: *Findings from the WASP posterior ensemble using Method 2:* ***a****) Frequency distribution for the magnitude of fast feedbacks. The orange range indicates the model best estimate, 66% confidence band (solid orange), and 90% confidence band (dotted orange);* ***b****)* λ_{total} *over multiple response timescales. Solid green line indicates ensemble best estimate with dashed lines showing 66% confidence limits; and* ***c****) Scatter plot of fast and multi-decadal feedback in posterior ensemble with opacity representative of weighting and therefore agreement with observations.*

This compares to the estimated magnitude of multi-decadal feedbacks, as depicted in Figure 2.6. Unlike the distribution of fast feedbacks, which was positively skewed, the distribution of multi-decadal feedbacks in WASP shows a negative skew. This method yields a median estimate of 0.85 $Wm^{-2}K^{-1}$ for the magnitude of multi-decadal feedbacks, which is similar to the estimate of fast feedbacks, suggesting they have a similar magnitude. There is a 66% confidence that the magnitude of Earth's multi-decadal feedbacks is in the range of 0.50 $Wm^{-2}K^{-1}$ to 1.25 $Wm^{-2}K^{-1}$ and 90% confidence that is in the range of 0.32 $Wm^{-2}K^{-1}$ to 1.59 $Wm^{-2}K^{-1}$. These similar estimated ranges for fast and multi-decadal feedbacks are supported by the value of λ_{total}, as shown in figure 2.5b where λ_{total} increases in a stepwise manner from ~-3.3 $Wm^{-2}K^{-1}$ at instantaneous timescales, to ~-2.4 $Wm^{-2}K^{-1}$ on monthly to annual timescales, and finally to ~-1.6 $Wm^{-2}K^{-1}$ on multi-decadal to centennial scale timescales. This indicates that Earth's feedbacks become more amplifying on longer timescales. Figure 2.6 also displays the estimated magnitude of multi-decadal feedbacks in the CMIP5 and CMIP6 model ensembles for comparison, as well as the estimated range of values used in the probabilistic assessment of climate sensitivity by Sherwood et al. (2020).

Figure 2.5c highlights the relationship between fast and multi-decadal feedbacks in each individual simulation from the posterior ensemble from method 2. Although weaker than method 1, this method shows a negative correlation between the magnitude of fast and multi-decadal feedbacks in each ensemble member, with an R^2 value of 0.68. This indicates that stronger amplifying fast feedbacks correspond to weaker amplifying multi-decadal feedbacks in a single simulation, and vice versa.

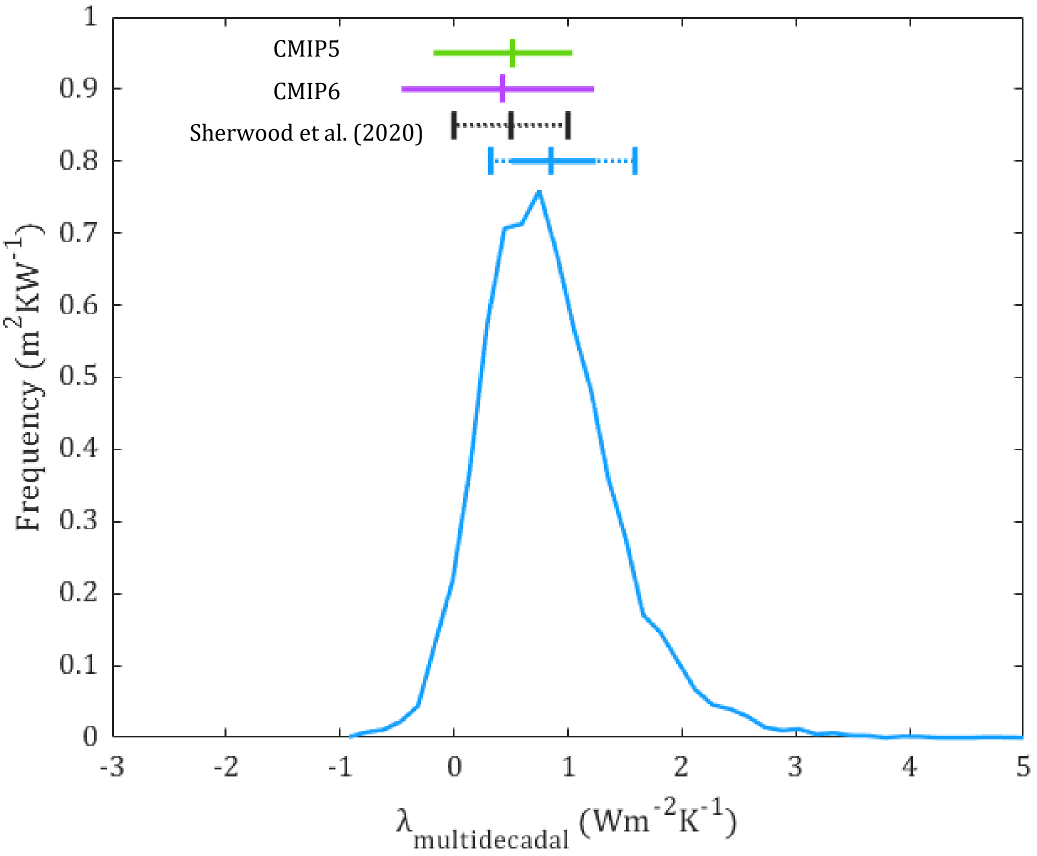

Figure 2.6: *Frequency distribution of the magnitude of multi-decadal feedbacks in the WASP ensemble using Method 2 (blue). The blue range indicates the WASP ensemble best estimate, 66% confidence band (solid blue), and 90% confidence band (dotted blue). The black range indicates the best estimate and 90% confidence limits used by Sherwood et al. (2020) in their probabilistic assessment. The range of best estimates for the pattern effect from multi-decadal feedbacks in the CMIP5 (green) and CMIP6 (purple) ensembles are displayed for comparison (the central markers indicate the overall ensemble best estimates).*

2.3.3 Method 3: Multivariate likelihood function

The simulated annual temperature anomalies from 1850 to 2020 from the posterior ensemble extracted by Method 3 are depicted in Figure 2.7. Whilst the shape is similar to the temperature simulation from Method 2, there is greater uncertainty throughout, as illustrated by the wider confidence bands. Like Method 2, this method estimates a median temperature rise of 1.20°C since 1850, compared to 1.26°C in the forced temperature constraint. However, in places the confidence bands of the simulated time series exceed 0.2°C indicating that temperature is not constrained to the same extent using Method 3 as using Method 2.

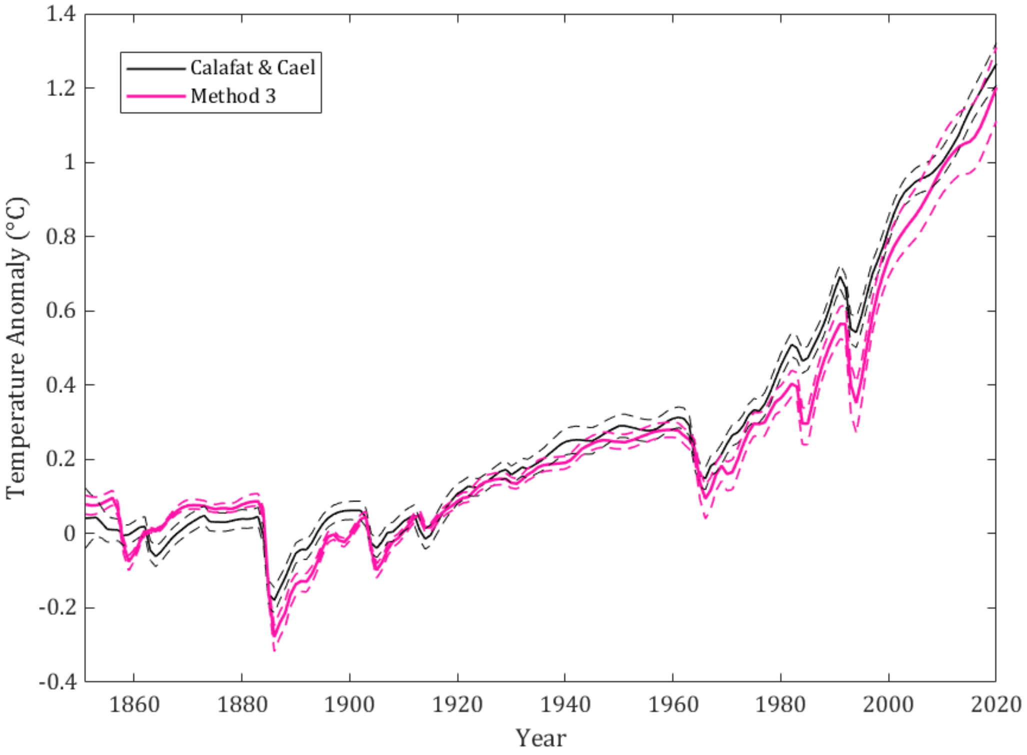

Figure 2.7: *Median annual temperature anomalies from 1850 – 2020 for the WASP posterior ensemble using Method 3 with 66% confidence limits (pink) and the mean forced temperature profile (black) from Cael and Calafat (in review) with 1σ confidence bands.*

Meanwhile, the frequency distributions for the magnitude of fast and multi-decadal feedbacks for Method 3 are depicted in Figure 2.8. This method gives a median estimate of -0.07 Wm^{-2}K^{-1} for λ_{md} indicating a very weak damping effect and 1.98 Wm^{-2}K^{-1} for λ_{fast} which represents a strong amplifying effect. Method 3 also estimates that the magnitude of Earth's multi-decadal feedbacks is in the range of -0.46 Wm^{-2}K^{-1} to 0.31 Wm^{-2}K^{-1} with 66% confidence and in the range of -0.78 Wm^{-2}K^{-1} to 0.60 Wm^{-2}K^{-1} with 90% confidence (Figure 2.8a). This contrasts with the estimates of Earth's fast feedbacks using this method with 66% confidence that the magnitude is in the range of 1.54 Wm^{-2}K^{-1} to 2.39 Wm^{-2}K^{-1}, and the range of 1.20 Wm^{-2}K^{-1} to 2.62 Wm^{-2}K^{-1} with 90% confidence (Figure 2.8b).

These findings are supported by the value of λ_{total} over multiple response timescales, as shown in Figure 2.8c. Here, λ_{total} increases from ~-3.3 Wm^{-2}K^{-1} at instantaneous timescales to ~-1.25 Wm^{-2}K^{-1}at annual timescales, and then decreasing slightly to ~-1.37 Wm^{-2}K^{-1}on multi-decadal to centennial timescales. This indicates a very strong amplifying fast feedback and very weak damping multi-decadal feedback which contrasts significantly from the findings from Method 2. Unlike in Method 2, where the confidence bands for the value of

λ_{total} narrow at multi-decadal timescales compared to annual timescales, in Method 3 the uncertainty is only slightly reduced between response timescales.

Finally, the relationship between fast and multi-decadal feedbacks in Method 3 is shown in Figure 2.8d. The negative correlation between the magnitude of fast and multi-decadal feedback is weakest using Method 3 relative to Methods 1 and 2, with an R^2 value of 0.45. The relationship also appears less linear but because the simulations in Method 3 were all given equal weighting, it is not possible to determine the relative success of each ensemble member in matching the observations and this makes the relationship less clear.

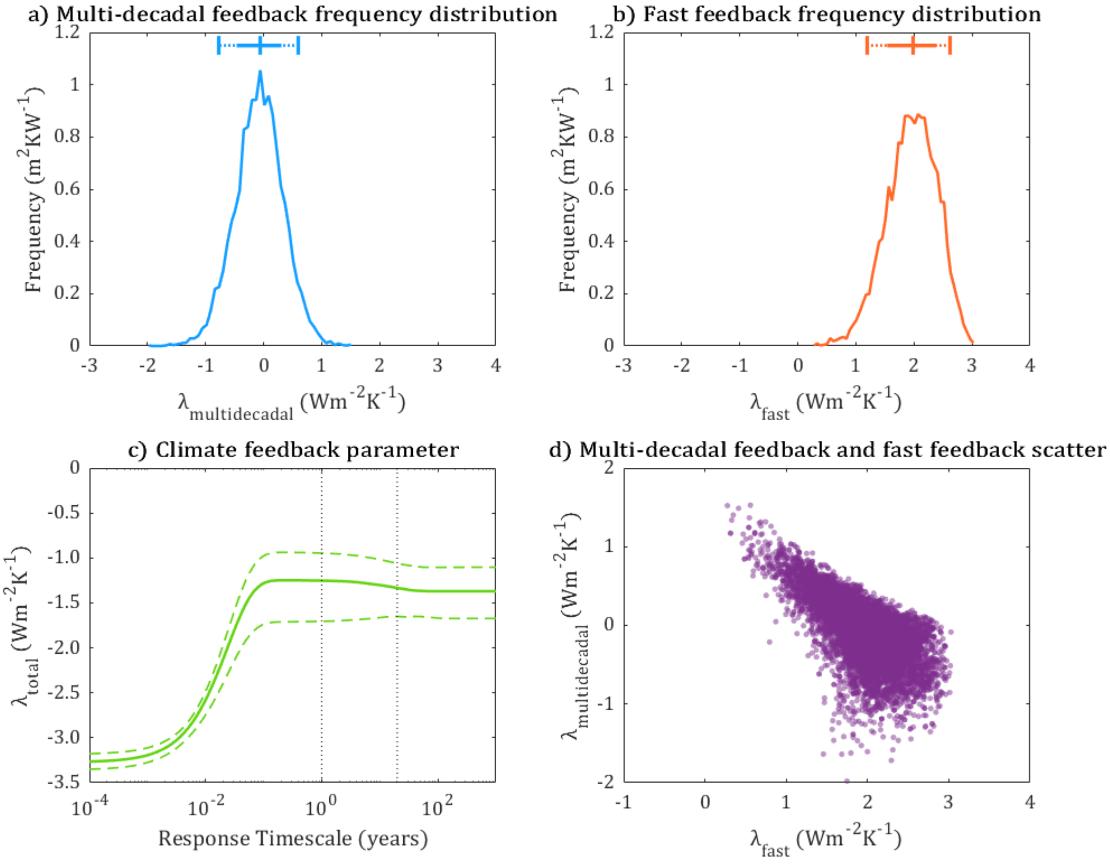

Figure 2.8: *Findings from the WASP posterior ensemble using Method 3:* ***a****) Frequency distribution for the magnitude of multi-decadal feedbacks. The blue range indicates the ensemble best estimate, 66% confidence band (solid blue), and 90% confidence band (dotted blue);* ***b****) Frequency distribution for the magnitude of fast feedbacks. The orange range indicates the ensemble best estimate, 66% confidence band (solid orange), and 90% confidence band (dotted orange);* ***c****) λ_{total} over multiple response timescales. Solid green line indicates ensemble best estimate with dashed lines showing 66% confidence limits; and* ***d****) Scatter plot of fast and multi-decadal feedback values in posterior ensemble.*

2.4 Discussion

The primary objective of this chapter is to constrain the magnitude of Earth's multi-decadal feedbacks with greater statistical certainty and to identify the optimal method of doing so. Of the three methods, Method 2, which utilises a cost function, 1-year averaged temperature anomalies and a forced temperature profile extracted from the HadCRUT5 observational dataset (Cael and Calafat, in review), shows the best agreement between simulated temperature and observations from 1850 to 2020, as shown in Figure 2.9. Both the long-term trend and the short-term inter-annual variability are captured by the WASP ensemble using this method and confidence bands are narrow throughout the time series. This increases trust in the feedback estimates of Method 2 as it most successfully reproduces the observational constraint.

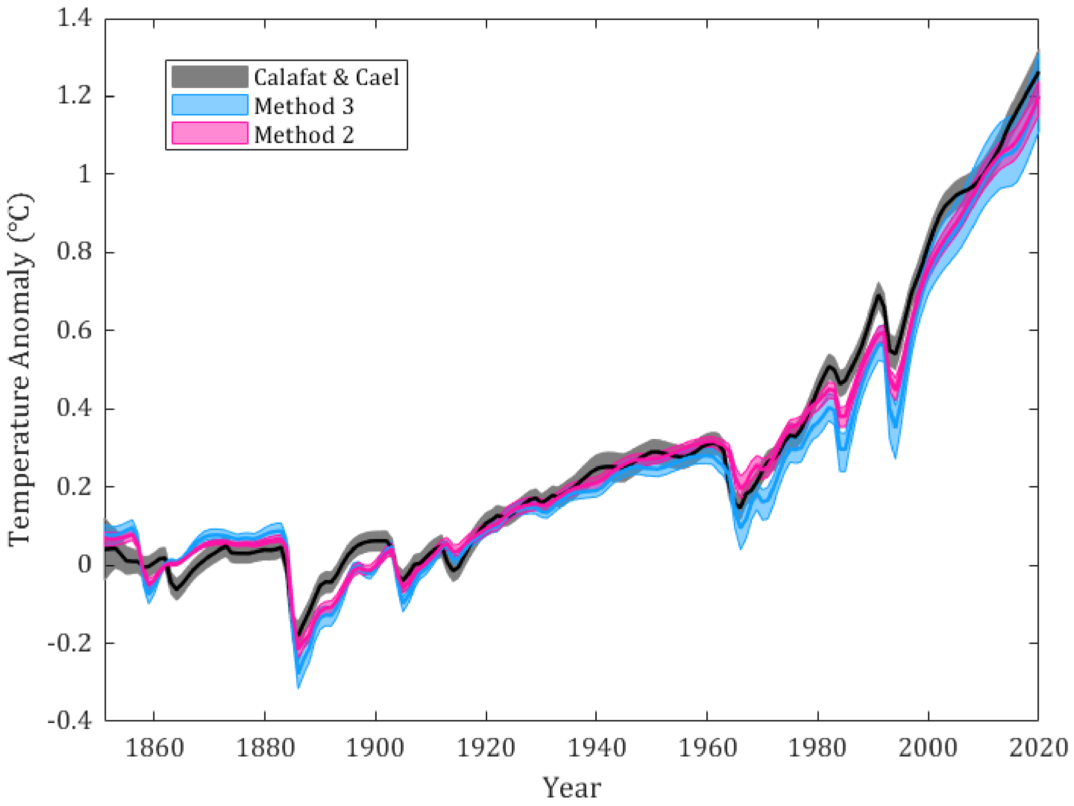

Figure 2.9: *Comparison of temperature anomalies from 1850 – 2020 for Methods 2 and 3 compared to the observational constraint from Calafat & Cael. The solid pink and blue lines indicate median temperature anomalies for Method 2 and Method 3, respectively, with shading indicating 66% confidence limits. Solid black link indicated mean temperature anomalies from forced temperature profile, with 1σ confidence bands (grey shading).*

All three methods slightly underestimate the overall warming that has occurred in the historical period compared to their respective observational constraint, each simulating a median temperature increase of approximately 1.20°C since 1850. At present, the slowest feedbacks included in WASP are multi-decadal feedbacks which functionally operate on a timescale of approximately 20-45 years. However, WASP currently does not adequately capture all the processes that influence Earth's climate beyond this timeframe and therefore the omission of slower feedbacks that operate on timescales longer than 100 years could explain this apparent discrepancy between WASP and the historical record. This is a common problem amongst studies that aim to constrain the strength of climate feedbacks using the historical record (Gregory and Andrews, 2016; Knutti, Rugenstein and Hegerl, 2017; Andrews *et al.*, 2018; Dessler, 2020; Tokarska *et al.*, 2020). Future work shall look to address this.

The underestimation of historical warming in all methods could also be attributed to the use of outdated radiative forcing estimates in this version of WASP which were derived from the 5th Assessment Report (AR5) of the IPCC. The 6th Assessment Report (AR6) revised their estimates of anthropogenic effective radiative forcing (ERF) from 2.3 Wm^{-2} (1.1 – 3.3 Wm^{-2}) in AR5 to 2.72 Wm^{-2} (1.96 – 3.48 Wm^{-2}) in AR6 (Myhre *et al.*, 2013b; Forster *et al.*, 2021). This increase is attributable to the revised higher estimate of ERF from greenhouse gas (GHG) emissions, which is slightly compensated by the revised ERF estimates from aerosol-radiation and aerosol-cloud interactions. The use of the revised AR6 radiative forcing estimates to inform the prior ensembles of WASP would likely have a material impact on the resultant estimates of GMST change in the posterior ensemble and could potentially partly resolve the current underestimation of historical warming. The decision to use AR5 estimates for this study was due to the timing of the publication of AR6, which occurred after work for this chapter had initiated. Future work should seek to explore the implications of the AR6 estimates for WASP's estimates further.

The use of 1-year averages in the likelihood filter proves to have a distinct advantage over 20-year averages in reducing uncertainty. The 90% and 66% confidence ranges are significantly narrower for the frequency distributions of λ_{md} and λ_{fast} using Methods 2 and 3 over Method 1. For example, Method 1 gives a 90% confidence range of 2.93°C for λ_{md} compared to 1.27°C for Method 2 suggesting that the use of 1-year averages allows the magnitude of feedbacks to be more successfully constrained than 20-year averages. This is because the new method requires a simulation to successfully reproduce the inter-annual temperature variation as well as the overall trend in order to be observation consistent. This is supported by the narrow point at the 20-year mark in the graph of λ_{total} over multiple response timescales for Method 1 (Figure 2.3c) which indicates that the magnitude of λ_{total} is well-constrained at this timescale, but poorly constrained otherwise when using Method 1. In contrast, the plot of λ_{total} over multiple response timescales using Method 2 in Figure 2.5b has a narrower range of uncertainty throughout but particularly on inter-annual timescales, representing the use of 1-year averages to constrain feedbacks in Method 2.

Method 2 gives a best estimate for λ_{md} of 0.85 $Wm^{-2}K^{-1}$ which represents a more amplifying effect than the estimates of λ_{md} used in Sherwood et al (2020). This supports the CMIP5 and CMIP6 models that simulate stronger amplifying multi-decadal feedbacks and provides independent evidence that Earth's multi-decadal feedbacks are unlikely to be damping (Andrews, Gregory and Webb, 2015; Dong *et al.*, 2020). This estimate for λ_{md} is comparatively high next to the multi-model means of CMIP5 and CMIP6 but is within the ranges of best estimates from coupled models in the two ensembles. Furthermore, this estimate is similar to other studies that estimate the pattern effect from the historical record; Andrews *et al.* (2022) use 14 atmospheric general circulation models to give an estimate of 0.70 ± 0.47 $Wm^{-2}K^{-1}$ for 1871-2010 when forced with sea surface temperatures (SSTs) from the Atmospheric Model Intercomparison Project (AMIP) II data set . At present, the availability of quantitative estimates of the pattern effect from reduced complexity models is very limited, which prohibits a full systematic comparison. Whilst the estimated 66% confidence intervals for fast and multi-decadal feedbacks are very similar in Method 2, the fast feedbacks display a positive skew and the multi-decadal feedbacks a negative skew, indicating that there is a higher frequency of weaker amplifying fast feedbacks and a higher frequency of stronger amplifying multi-decadal feedbacks relative to each other.

Method 3 provides a very different result. Here fast feedbacks are found to have a much stronger amplifying effect than multi-decadal feedbacks which have a fairly equal likelihood of being weakly amplifying or weakly damping. As supported by λ_{total} over multiple response timescales, Method 3 suggests that climate sensitivity is driven by fast feedbacks that operate on timescales less than a year and that slower feedbacks have very little influence overall, which would imply an almost total lack of a pattern effect. This contradicts the findings of CMIP5 and CMIP6 which suggest a mean change of 0.51 $Wm^{-2}K^{-1}$ and 0.4 $Wm^{-2}K^{-1}$ respectively from multi-annual to centennial timescales indicating amplifying multi-decadal feedbacks (Andrews, Gregory and Webb, 2015; Dong *et al.*, 2020). This contradiction reduces trust in the results of Method 3.

Nevertheless, Method 3 has limitations and therefore could be seen to be less reliable than Method 2 which weights simulations according to their similarity to the observational constraint. Method 3 however, considers all simulations equally likely if they exceed the acceptance limit and so does not distinguish between better and worse performing simulations. This offers an explanation as to why temperature is less constrained over time in Method 3 compared to Method 2. It is also possible that if weighted differently, a clearer distinction could be found between simulations with amplifying multi-decadal feedbacks and those with damping multi-decadal feedbacks.

The use of the multivariate likelihood function in Method 3 aims to address the unrealistic assumption that the temperature of an individual year is independent and uninfluenced by the temperature of the previous year. However, the behaviour of the multi-decadal feedbacks in this method suggests that the covariance matrix is overpowered here and putting too much emphasis on the fast feedbacks that respond in less than 1 year. Future experiments should aim to address the numerical instability of the multivariate likelihood function when working with large covariance matrices so that simulations can be weighted. An investigation into the accuracy of any covariance matrix used in the likelihood function is also recommended.

2.5 Conclusions

This chapter has sought to constrain the magnitude of Earth's feedbacks, with a particular focus on feedbacks that operate on multi-decadal timescales. This has been done using three different experimental methods of extracting a posterior ensemble from WASP, with the aim of comparing the relative success of each method of likelihood filter. Of the three, this study indicates that a likelihood filter comprised of a cost function and 1-year averages is the most effective method at this stage, although not without its limitations. The use of a multivariate likelihood function that introduces covariance between individual years shows promise but there are several numerical and statistical challenges to address before this method proves to be an advantage over the existing cost function.

The new forced temperature profile from Cael and Calafat (in review) provides a substantial improvement as a constraint over the unmodified HadCRUT5 observational dataset as this allows the forced signal to be targeted and the random noise ignored when comparing the relative success of a simulation in reproducing historical temperature change. This allows us to constrain the magnitude of Earth's fast and multi-decadal feedbacks with greater statistical accuracy than previous studies such as Goodwin (2021) and Goodwin & Cael (2020). The use of 1-year averages in the likelihood filter of Methods 2 and 3 also proves an advantage over the 20-year averages used in Method 1 as the filter is able to target both inter-annual and multi-decadal response timescales by ensuring that ensemble members successfully simulate the short-term volcanic response as well as the longer-term trend in order to be included in the posterior ensemble.

Overall, this study finds a best estimate of 0.85 $Wm^{-2}K^{-1}$ for the magnitude of multi-decadal feedbacks with 90% confidence that the value is within the range of 0.32 $Wm^{-2}K^{-1}$ to 1.59 Wm^{-}

$^2K^{-1}$. This provides independent evidence to support the complex models from CMIP5 and CMIP6 that simulate stronger amplifying multi-decadal feedbacks.

Chapter 3 Ice sheet-albedo feedback

The following work was submitted to Geophysical Research Letters on 03/05/2024, was accepted on 29/07/2024, and published on 06/08/2024. It can be cited as:

Booth, A., Goodwin, P., & Cael, B. B. (2024). Ice sheet-albedo feedback estimated from most recent deglaciation. Geophysical Research Letters, 51, e2024GL109953.

3.1 Abstract

Ice sheet feedbacks are underrepresented in model assessments of climate sensitivity and their magnitudes are still poorly constrained. We combine a recently published record of Earth's Energy Imbalance (EEI) with existing reconstructions of temperature, atmospheric composition, and sea level to estimate both the magnitude and timescale of the ice sheet-albedo feedback since the Last Glacial Maximum. This facilitates the first opportunity to quantify this feedback over the most recent deglaciation using a proxy data-driven approach. We find the ice sheet-albedo feedback to be amplifying, increasing the total climate feedback parameter by 42% and reaching an equilibrium magnitude of 0.55 $Wm^{-2}K^{-1}$, with a 66% confidence interval of 0.45 - 0.63 $Wm^{-2}K^{-1}$. The timescale to equilibrium is estimated as 3.6ka (66% confidence: 1.9 - 5.5ka). These results provide new evidence for the timescale and magnitude of the amplifying ice sheet-albedo feedback that will drive anthropogenic warming for millennia to come.

3.2 Plain language summary

During a deglacial transition, ice sheets melt and retreat, decreasing the reflectivity of the land surface and increasing the surface temperature, leading to further melting. It is agreed that this feedback amplifies global warming on millennial timescales, but the exact magnitude and timescale are still very uncertain. This is important because the stronger the feedback, the more sensitive Earth's climate is to carbon dioxide on long timescales. We use proxy data records of the past 25,000 years to quantify the ice sheet-albedo feedback since the Last Glacial Maximum and estimate the time taken for the feedback to reach equilibrium and stabilise. We find that the ice sheet-albedo feedback strongly amplifies warming over thousands of years, increasing our understanding of how human activity today will continue to influence our climate for generations into the future.

3.3 Introduction

Constraining the magnitude of Earth's climate feedbacks has been a high priority for the scientific community in recent years to ensure that our predictions of future climate change are well-informed by accurate estimates of Earth's climate sensitivity. However, slow feedbacks that operate on timescales of more than a century continue to be overlooked in favour of near-term climate impacts. This limits our full understanding of the Earth System and how it may be affected by anthropogenic activity for far longer than a human lifetime (Clark *et al.*, 2016). Ice sheet extent has a considerable influence on the climate on timescales of centuries to millennia, primarily through direct changes to land albedo and indirectly through the alteration of cloud cover over the northern Atlantic and Pacific Oceans (Vizcaíno *et al.*, 2008; Abe-Ouchi *et al.*, 2015; Fyke *et al.*, 2018; Zhu and Poulsen, 2021; Cooper *et al.*, 2024). The IPCC Sixth Assessment Report states with high confidence that it is *'very likely'* that the ice sheet-albedo feedback has an amplifying effect on millennial timescales, but the specific magnitude or exact response timescale is very uncertain (Forster *et al.*, 2021).

As many global climate models are primarily used to predict climate change over the next one to two centuries, ice sheet-climate interactions are often simplified as their influence on climate sensitivity is assumed to be insignificant on these short timescales (Madsen *et al.*, 2022). Fast feedbacks arising from small-scale changes in snow albedo are well represented in global climate models (GCMs) with understanding based on observational data (Box *et al.*, 2012; Fyke *et al.*, 2018; Ryan *et al.*, 2019). However, on longer timescales, the integration of large-scale changes to ice sheet-albedo into a GCM is challenging and no GCM includes a two-way coupled dynamical ice sheet component (e.g. (Smith, George and Gregory, 2021; Schmidt *et al.*, 2023)). When using the deglaciation to estimate present-day climate sensitivity, ice sheet-climate interactions are commonly included as a source of radiative forcing rather than as a feedback mechanism (Rohling *et al.*, 2012b).

The challenge of quantifying the ice sheet-albedo feedback stems from an ongoing struggle to reconstruct ice sheet extent with sufficient temporal resolution and disentangle the relationship between global surface temperatures, ocean heat content, and ice sheet retreat in proxy records (Elderfield *et al.*, 2012; Shakun *et al.*, 2015; Rohling *et al.*, 2021). However, a newly published proxy-based record for Earth's Energy Imbalance (EEI: : (Baggenstos *et al.*, 2019; Shackleton *et al.*, 2023)) since the Last Glacial Maximum (LGM) now allows the calculation of the time evolution of the climate feedback parameter, λ, over the last deglaciation both with and without the ice sheet-albedo feedback included. This progress comes from combining existing reconstructions of surface temperature, atmospheric composition and the albedo effect of changes in ice sheet extent reflected in sea level reconstructions.

This study represents a novel attempt to simultaneously constrain the ice sheet-albedo feedback magnitude and response timescale based on proxy-based evidence and without the need for model-based assumptions of the time evolution of energy imbalance. Earth's most recent deglaciation (~19 – 7ka before present (BP)) offers a unique opportunity to study ice sheet-climate interactions as the period saw the dramatic collapse of the Laurentide and Eurasian ice sheets and a subsequent rise in global sea level by ~120m (Lambeck *et al.*, 2014; Lecavalier *et al.*, 2014; Simms *et al.*, 2019; Quiquet *et al.*, 2021). Global mean surface temperatures increased by approximately 7°C from the onset of the deglaciation to the preindustrial period and this relatively rapid change in temperature provides an excellent testing ground in which to explore climate feedback behaviour (Snyder, 2016; Kaufman *et al.*, 2020; Osman *et al.*, 2021).

3.4 Materials & methods

The total climate feedback parameter, λ_{total}, is the additive combination of j internal feedbacks, $\sum \Delta\lambda_j$, and can be calculated using Earth's most recent deglaciation according to the traditional linear energy budget equation:

$$\lambda_{total} = \frac{\Delta N - \Delta F_{total}}{\Delta T}$$

Equation 3.1

Where λ_{total} is the total effective climate feedback parameter (Wm^{-2}K^{-1}), and takes the sign convention that λ_{total} is negative for a stable climate system, such that individual amplifying feedbacks are positive contributions to λ_{total} and individual damping feedbacks are negative contributions to λ_{total}; ΔN is the net top-of-atmosphere (TOA) energy imbalance anomaly (also referred to as EEI, Wm^{-2}); ΔF_{total} is the sum of i external forcings, $\sum \Delta F_i$, and is therefore the total radiative forcing anomaly (Wm^{-2}); and ΔT is the global surface temperature anomaly (K), all relative to the LGM. The energy imbalance from ice sheet-albedo (Wm^{-2}) can be included in the above energy budget equation in two possible ways: either as F_{alb} and part of the external forcings, $\sum \Delta F_i$, or as λ_{alb} and part of the internal feedbacks, $\sum \Delta\lambda_j$ (e.g. Rohling *et al.* (2012b)). We calculate the magnitude of λ_{total} using both methods.

In either case, the influence of the ice sheet-albedo feedback on spatial patterns of temperature change should not be ignored (Cooper *et al.*, 2024). The total ice sheet feedback is the additive combination of direct and indirect effects on the climate system, but the radiative contribution from indirect pattern effects resulting from changes to ice sheet extent is very difficult to quantify. Therefore, we specifically target the direct influence of albedo change from ice sheet retreat in this study and apply a later adjustment to account for indirect pattern effects. With the time-evolving estimate of λ_{total} that we calculate here, we can constrain the magnitude of the ice sheet-albedo feedback at equilibrium, $\lambda_{alb^{(\infty)}}$, and its timescale.

The recent record for EEI over the last deglaciation by Baggenstos *et al.* (2019), and further analysed by Shackleton et al. (2023), based on noble gas thermometry data from the West Antarctic Ice Sheet Divide and EPICA Dome C ice cores is utilised here to represent a novel proxy-based estimate and uncertainty of ΔN in the above equation 3.1. We display alternative results using the EEI record based on benthic foraminiferal δO18 proxy data from Shackleton *et al.* (2023) in the supplementary material. ΔT is here calculated from Osman et al. (2021) who used model simulations and palaeoclimate proxy data to assimilate a globally resolved record of surface temperature change for the past 24 ka (Osman *et al.*, 2021). $\Delta F_{total}$is comprised of instantaneous radiative forcing records for CO_2, CH_4, and N_2O (greenhouse gases: GHGs) from Köhler *et al.* (2017), atmospheric dust, and ice sheet-albedo change since the LGM. Radiative forcing from atmospheric dust is calculated from the Lambert et al. (2012) dust flux record, which used high resolution ice core data from EPICA Dome C, Antarctica, and is converted using a linear scaling following Rohling et al. (2012a):

$$\Delta F_{dust} = -1.9\log_{10}(\Delta\chi)$$

Equation 3.2

Where $\Delta\chi$ is the change in dust flux (Lambert *et al.*, 2012; Rohling *et al.*, 2012a). An additional ±50% uncertainty was applied to the dust forcing calculation following Rohling et al (2012a) to reflect uncertainty in the relationship between measured quantities and climate forcing. Meanwhile, radiative forcing from ice sheet-albedo change since the LGM is calculated following Rohling et al. (2012a) and Hansen et al. (2008) who established a linear relationship between sea level change, ΔSL (in metres), and subsequent forcing impact in ΔF_{alb}(in Wm^{-2}):

$$\Delta F_{alb} = 0.0308\Delta SL$$

Equation 3.3

Where ΔSL is negative during glacial periods (Hansen, 2008; Rohling *et al.*, 2012a). An additional ±20% uncertainty is applied to the calculation of ice sheet-albedo forcing, ΔF_{alb}, following Rohling et al. (2012a). Sea level data is sourced from Lambeck et al. (2014) who reconstruct global sea level and ice volumes since the LGM (Lambeck *et al.*, 2014). All best estimates and standard deviations are interpolated to an annual temporal frequency for the past 25 ka to capture the LGM and subsequent deglaciation. In the case of ΔF_{dust}, the annual record is smoothed with a 501-year smoothing spline to extract the long-term signal and reduce the influence of random noise. As the focus of this study is the estimation of λ_{total} over the most recent deglaciation, all records are made relative to 18 ka BP to reflect the point at which global temperatures started to increase.

In order to quantify uncertainty, 5000 estimates for λ_{total} are generated, with a different random number coefficient on a normal distribution, N(0,1), for each variable in the energy budget equation (CO_2, N_2O, CH_4, dust, and ice sheet albedo forcing, temperature, and EEI) and each simulation. These coefficients are then applied to each simulation as a multiplier on the standard deviation across all 18001 time steps of each simulation. In this way, a probability distribution of possible values can be generated for each variable, including λ_{total}.

Figure 3.1a compares the change in combined radiative forcing from CO_2, CH_4, and N_2O (GHGs) and dust over the past 18 ka to the change in radiative forcing from GHGs, dust and ice sheet-albedo. When ice sheet-albedo forcing is excluded from forcing, the increase in combined forcing increases steadily, before stabilising around 11 ka BP at 5.0 $\pm$0.5 Wm^{-2}, coinciding with the early Holocene (Fig. 3.1a: blue). A small decrease to 4.1$\pm$0.2 Wm^{-2} at 6.5 ka BP is followed by a gentle increase to 5.1 $\pm$0.4 Wm^{-2} by 3 ka BP and then the sharp rise in the industrial period. This contrasts with the pink curve, which includes the added influence of radiative forcing from ice sheet-albedo change. In this case, total forcing quickly exceeds 5 Wm^{-2} by 13.5 ka BP and maintains an increasing trend throughout the Holocene to stabilise at approximately 8.8 $\pm$0.8 Wm^{-2} in the most recent three millennia before the familiar rapid rise in the industrial period (Fig. 3.1a: pink). This illustrates the notable influence of ice sheet-albedo change on global total radiative forcing over time. The treatment of ice sheet-albedo change as a forcing necessitates the inclusion of ΔF_{alb}, which introduces approximately 1 Wm^{-2} of additional uncertainty by the end of the simulated period (Fig. 3.1a: pink). This highlights the need for more precise records of ice volume change over time as well as improved understanding of the relationship between ice volume and effective radiative forcing from ice sheet changes (Zhu and Poulsen, 2021). We assume that orbital changes in the amount of solar radiation received by the Earth are significantly smaller than this forcing and so are not included in this analysis (Beer, Mende and Stellmacher, 2000; Lisiecki, 2010; Rial, Oh and Reischmann, 2013).

The radiative forcing contribution from ice sheet-albedo change is better illustrated in Figure 3.1b which depicts the difference between the two curves in Figure 3.1a. The total change in radiative forcing from ice sheet retreat (ΔF_{alb}) continuously increases after 18 ka BP until it stabilises at approximately 3.7 $\pm$ 0.4 Wm^{-2} by 6ka BP, according to the proxy record. This value is within the uncertainty range of -3.2 Wm^{-2} of effective radiative forcing (ERF) from land ice sheets at the LGM, estimated by Zhu and Poulsen (2021), lending some confidence to the model used in this study. It should be noted that the calculation of ERF also accounts for ice sheet-climate interactions with the atmospheric temperature profile, water vapour, and clouds, and this contribution should ideally be considered. However, at the time of writing we, the authors, are not aware of the existence of any high resolution, transient record for ERF from GHGs, dust, or ice sheet-albedo over the course of the last deglaciation. Therefore, all references to radiative forcing data in this study refer to instantaneous radiative forcing (IRF), as opposed to ERF which is the preferred measure used in assessments of modern climate sensitivity (Forster *et al.*, 2016; Smith *et al.*, 2020; Forster *et al.*, 2021).

Figure 3.1c depicts the change in Earth's TOA energy imbalance over time, as adapted from Shackleton et al. (2023). There is substantial fluctuation over the past 18 ka, but the overall trend is that of a gentle decrease in EEI over the simulated period, which would indicate that the warming trend since the deglaciation is unforced by changes in the energy budget. Finally, Figure 1d shows the global mean surface temperature anomaly since the deglaciation. We see approximately 7.5 K of warming over the past 18ka, although most of this warming took place in the first 10 ka. The small dip at 12.7ka BP represents the Younger Dryas cold period, the most recent and most severe stadial since the LGM. The return to the warming trend coincides with a spike in EEI and a sharp rise in total radiative forcing, highlighting good temporal agreement between proxy datasets.

To estimate the magnitude of the millennial scale ice sheet-albedo feedback, λ_{total} is calculated in two different ways: by considering ice sheet-albedo change as a forcing rather than a feedback, and therefore included in ΔF_{total} (Eq. 3.1), or as a feedback rather than a forcing and so ice sheet-albedo change is excluded from ΔF_{total}. The difference between these two estimates represents the ice sheet-albedo feedback, λ_{alb} , and is calculated for all time steps in all 5000 simulations. The initial 1.5 ka are excluded from analysis as, during this interval, ΔT remains very close to zero, causing numerical instability (Eq. 3.1) and is too small to provide a reliable estimate for λ.

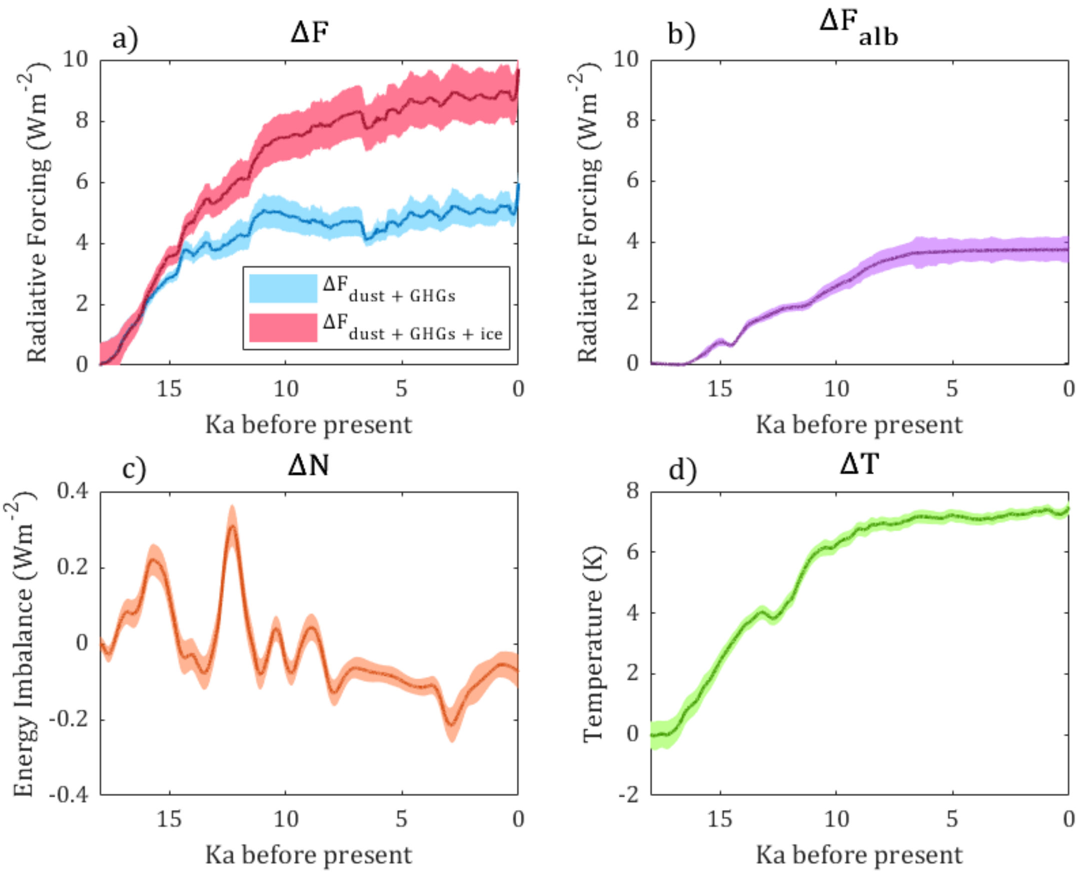

Figure 3.1: *The components of the energy budget equation over the past 18 ka with 1σ uncertainty (shaded areas). All plots are displayed as anomalies relative to 18 ka BP* ***a****) Change in total radiative forcing when forcing from ice sheet-albedo change is included (pink) and excluded (blue)* ***b****) Change in total radiative forcing from ice sheet-albedo change,* ***c****) Change in Earth's Energy Imbalance,* ***d****) Global surface temperature anomaly.*

In order to identify the timescale of the feedback, λ_{alb} is applied to a non-linear regression model according to:

$$\lambda_{alb} = \lambda_{alb(\infty)}(1 - e^{-t/\tau})$$

Equation 3.4

Where λ_{alb} is the estimate of the ice sheet-albedo feedback at timestep, t, and $\lambda_{alb(\infty)}$ is the magnitude of the ice sheet-albedo feedback at equilibrium. τ is the response timescale that λ_{alb} operates over, that is the time taken to reach equilibrium. The above regression model is applied to all 5000 simulations to generate 5000 estimates for $\lambda_{alb(\infty)}$ and τ, which are subsequently analysed. Standard error weighting is found to have no significant impact on the probability distributions for each variable, so it is not used for our main analysis. By its nature, the above equation can yield numerical instabilities where values near very close to zero. Such outliers are removed from the overall ensemble of estimates to prevent erroneous bias. An outlier is defined here as being three or more scaled Median Absolute Deviations from the median.

Finally, we consider how ice sheets influence other feedbacks by altering the spatial pattern of temperature change, utilising proxy-derived estimates from Cooper *et al.* (2024) as a modification applied post-analysis. The total ice sheet feedback, $\lambda_{ice\ sheets}$, is therefore represented by the following equation:

$$\lambda_{ice\ sheets} = \lambda_{alb} + \lambda'$$

Equation 3.5

Where λ' represents the modification to the total feedback resulting from indirect pattern effects. λ' increases the total ice sheet feedback, $\lambda_{ice\ sheets}$, by N(0.37,0.23) Wm^{-2}K^{-1} (Cooper *et al.*, 2024).

3.5 Results

Figure 3.2a shows the total climate feedback parameter, λ_{total}, when ice sheet-albedo change is treated as a forcing (pink) or feedback (blue). Prior to 16ka, there is little difference between the magnitude of λ_{total} of either simulation, each peaking at approximately -1.7 Wm^{-2}K^{-1} and -1.6 Wm^{-2}K^{-1} respectively, supporting the notion that the ice sheet-albedo feedback was small on short timescales, although uncertainty is large. Over the course of the deglaciation, the two simulations diverge due to the influence of the ice sheet-albedo feedback. However, the evolution of λ_{total} follows a similar overall trend in either case; both increase steadily until ~6.5ka BP, before gently decreasing again and stabilising by ~2.5ka BP. When ice sheet-albedo change is included as a forcing, λ_{total} stabilises at approximately -1.2 $\pm$0.1 Wm^{-2}K^{-1}. When ice sheet-albedo change is included as a feedback, λ_{total} stabilises at -0.7 $\pm$0.07 Wm^{-2}K^{-1} in the final 2.5 ka BP.

The difference between the value of λ_{total} when ice sheet-albedo change is treated as either a forcing or feedback gives the climate feedback contribution from ice sheet-albedo change, λ_{alb}, which is displayed over time in Figure 3.2b. There is some fluctuation over time, but the overall trend closes to equilibrium after O(10,000) years. Figure 3.2b also shows the influence of indirect spatial pattern effects: applying the estimates from Cooper et al. (2024) in the form of the modification, λ', results in a mean increase of 67% in the total ice sheet feedback, $\lambda_{alb} + \lambda'$ (grey), compared to the ice sheet-albedo feedback, λ_{alb}, alone (purple). However, the influence of indirect pattern effects from ice sheets is still poorly constrained, and this is highlighted in the substantial additional uncertainty applied to the estimate of the total ice sheet feedback, $\lambda_{alb} + \lambda'$, compared to the estimated magnitude of the ice sheet-albedo feedback, λ_{alb}.

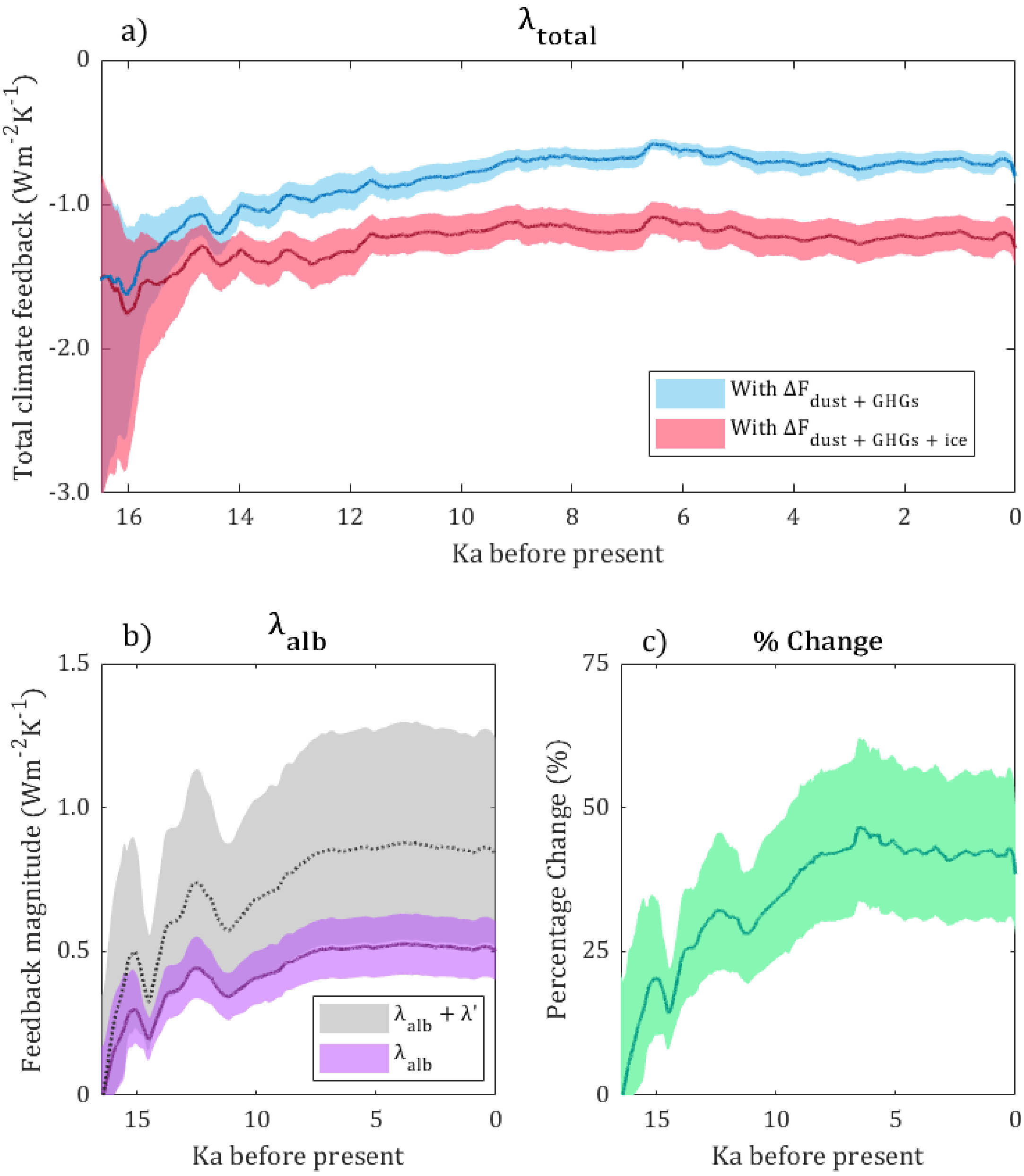

Figure 3.2: *The magnitude of the effective climate feedback parameter, λ, over the past 16.5 ka with 66% confidence interval shaded* ***a****) total climate feedback parameter, λ_{total}, when ice sheet-albedo is assumed to be a forcing (pink) or feedback (blue),* ***b****) ice sheet-albedo feedback, λ_{alb} (purple) and with pattern effect (grey),* ***c****) impact of the ice sheet-albedo feedback, λ_{alb}, on the total climate feedback parameter, λ_{total}, expressed as a percentage change.*

The impact of the ice sheet-albedo feedback, λ_{alb}, on the total climate feedback, λ_{total}, over time is further illustrated in Figure 3.2c which expresses the percentage change in λ_{total}

when λ_{alb} is included in the estimate. As λ_{alb} progresses to equilibrium, its contribution to the magnitude of λ_{total} increases substantially. By the late Holocene (5ka BP to present), the ice sheet-albedo feedback increases the total climate feedback parameter by 42% on average.

The probability distribution of the ice sheet-albedo feedback, λ_{alb}, is depicted in figure 3.3a which shows a best estimate 0.55 Wm^{-2}K^{-1} with a 66% confidence interval of 0.45 - 0.63 Wm^{-2}K^{-1} and 95% confidence interval of 0.33 - 0.77 Wm^{-2}K^{-1}. This represents an amplifying effect, which becomes even larger if the influence of the ice sheets on temperature patterns and nonlocal feedbacks is accounted for, as shown by the grey range. Figure 3.3b, meanwhile, shows the probability distribution of the response timescale, τ, of the ice sheet-albedo feedback, meaning the time taken for the feedback to reach equilibrium following a perturbation. We find a best estimate for τ of 3.6 ka, with a 66% confidence interval of 1.9 ka to 5.5 ka. The 95% confidence interval of 0.5 ka to 9.3 ka reveals a positive skew towards longer timescales.

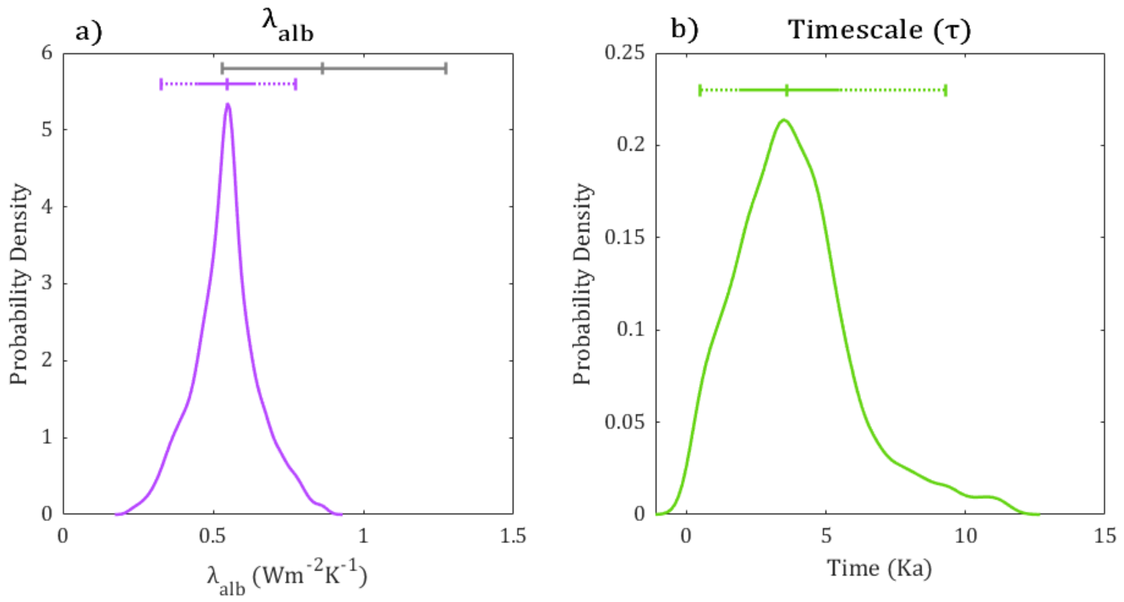

Figure 3.3: *Probability density distributions for **a**) ice sheet-albedo feedback, λ_{alb}, and **b**) the response timescale, τ, for λ_{alb}. Uncertainty intervals are displayed above each graph. Solid line indicates 66% confidence interval, dotted line indicates 95% confidence interval. The best estimate and 66% confidence interval for $\lambda_{alb} + \lambda'$ is given by the grey solid line for comparison (Fig. 3.3a).*

3.6 Discussion & conclusions

The primary aim of this study was to constrain both the magnitude and response timescale of Earth's ice sheet-albedo feedback using proxy records of the last deglaciation. We find that λ_{alb} has a 66% confidence interval of 0.45 - 0.63 $Wm^{-2}K^{-1}$, with a best estimate of 0.55 $Wm^{-2}K^{-1}$ (Fig. 3.3a). The feedback has a 95% confidence interval of 0.33 - 0.77 $Wm^{-2}K^{-1}$ supporting previous work that finds that ice sheet-albedo change has an amplifying effect. Furthermore, we find that the inclusion of the ice sheet-albedo feedback increases the total climate feedback parameter by approximately 42% at equilibrium, providing increased confidence that the amplifying effect of ice sheet retreat is not negligible. This effect becomes even stronger when the additional impact on spatial temperature patterns and non-local feedbacks are considered, increasing the best estimate of the total ice sheet feedback to 0.86 $Wm^{-2}K^{-1}$ with a 66% confidence interval of 0.53 – 1.28 $Wm^{-2}K^{-1}$. Indeed, considerable uncertainty persists around the quantification of the pattern effects resulting from changing ice sheet extent and the inclusion of a modification to account for them in this analysis substantially widens the estimated range. They are however a vital component in the interaction between ice sheets and the wider climate system and further work to increase understanding and improve quantification is required.

Additionally, we find with 66% confidence that λ_{alb} operates on a timescale of 1.9 ka to 5.5 ka, with a best estimate of 3.61 ka (Fig. 3.3b). However, the 95% confidence interval of 0.5 ka to 9.3 ka indicates that considerable uncertainty remains surrounding the exact response timescale of the ice sheet-albedo feedback. This is a limitation of using a single time interval of only 18 ka and certainty could be increased by repeating this experiment using multiple glacial cycles, although the limited availability of long, high resolution proxy records for radiative forcing and EEI may make this challenging with additional uncertainty introduced. However, Shackleton *et al.* (2023) have now extended the EEI record to 150 ka BP, providing new opportunities to do so.

This timescale estimate is applicable to a deglacial transition where ice sheets are experiencing shrinkage. The timescale over which ice sheets grow during a glacial transition and subsequently influence Earth's temperature, are subject to different physical processes and the feedback will behave differently. Furthermore, these findings specifically measure the magnitude of the ice sheet-albedo feedback for the most recent deglaciation. This is important to note as the initial ice sheet extent will differ for other periods of deglaciation. Indeed, the amplifying effect of future ice sheet retreat is likely to be comparatively reduced as the present extent of the Greenland ice sheet is smaller than that of the Laurentide ice sheet. However, ice sheet changes over Antarctica were minimal during the most recent deglaciation, and these could become substantial in the future, contributing to an amplifying ice sheet-albedo feedback regardless of the extent of the northern hemisphere ice sheets. Future work to estimate the ice sheet-albedo feedback using other glaciations and deglaciations in Earth's history could provide interesting insights as more data on these distant palaeoclimate periods is collected. Additionally, this area of research would benefit from a full quantification of ERF and transient pattern effects over the most recent deglaciation to increase the accuracy of estimates of radiative forcing from ice sheet-climate interactions.

This finding has implications for climate sensitivity and the role of ice sheet-climate interactions on long timescales. It is important to reiterate that the climate response to forcing is not constant in time, and instead climate sensitivity and climate feedbacks evolve over time in response to complex interactions between multiple forcings and feedbacks (Zeebe, 2013; Goodwin, 2018; Rohling *et al.*, 2018; Cael *et al.*, 2022; Cael *et al.*, 2023). Although the ice sheet-albedo feedback will have a negligible influence on climate sensitivity and warming in the 21st century, its influence is substantial on millennial timescales which could have a substantial impact on all components of the Earth System, particularly the biosphere (Lenton *et al.*, 2006; Stone and Lunt, 2013; Willeit *et al.*, 2014; Cabré, Marinov and Leung, 2015; Bao *et al.*, 2021; Spencer and Christy, 2023). This highlights the importance of accounting for slow climate feedbacks like that of ice sheet-albedo change in evaluations of climate sensitivity (Cooper *et al.*, 2024) as well as the value of measures like Earth System Sensitivity that take these processes into account (Lunt *et al.*, 2010; Knutti and Rugenstein, 2015; Clark *et al.*, 2016; Knutti, Rugenstein and Hegerl, 2017; Golledge *et al.*, 2019). Finally, these findings further highlight the increasing urgency for an effective climate change mitigation strategy to avoid serious long-term consequences for our planet and its ecosystems.

Chapter 4 Background state & ice sheet feedback on long timescales

4.1 Introduction

Over the past decade, it has become widely accepted that the magnitude of Earth's climate sensitivity is partly dependent on the background climate state, and is in fact highly likely to be greater in warmer climates than cooler climates as a consequence of non-linearities in the response of cloud feedbacks to warming (Caballero and Huber, 2013; von der Heydt and Ashwin, 2017; Farnsworth *et al.*, 2019; Zhu, Poulsen and Tierney, 2019; Anagnostou *et al.*, 2020; Cael and Goodwin, 2023). Therefore, the warmer the mean climate, the greater the warming required to re-balance the energy budget following a perturbation, such as anthropogenic forcing. This also means that estimates of climate sensitivity and feedback strength calculated from a specific cooler time period, such as the Last Glacial Maximum (LGM), cannot be automatically applied to studies of future climate change, which will be warmer.

Climate sensitivity, a quantitative measure of the earth system response to external forcing, is a function of the total effective climate feedback parameter, λ_{total} (Wm^{-2}K^{-1}), which expresses the overall change in the outgoing TOA radiation per unit of GMST change (Charney *et al.*, 1979). The IPCC 6th assessment report gives a best estimate with medium confidence for the total effective climate feedback parameter, λ_{total}, of -1.16 Wm^{-2}K^{-1}, with a very likely range of -1.81 to -0.51 Wm^{-2}K^{-1}, which is more negative (less sensitive) than the ensemble means of CMIP5 (-1.08 Wm^{-2}K^{-1}) and CMIP6 (-1.03 Wm^{-2}K^{-1}) (Forster *et al.*, 2021). The magnitude of λ_{total} remains uncertain because it cannot be measured directly and instead must be inferred from indirect evidence about Earth's energy budget or multiple components of the earth system. The spatially- and temporally- heterogeneous relationship between individual feedbacks and forcings in the earth system, as well as the role of potential tipping points, further increase the complexity of the challenge to quantify λ_{total} (Knutti and Rugenstein, 2015; Armstrong McKay *et al.*, 2022).

Despite the consensus that a relationship between feedback strength and the background state exists, understanding of the exact nature of this relationship is still incomplete, with changes in both temperature and atmospheric CO_2 concentration considered key drivers and the specific roles of individual feedbacks still being debated (Bjordal *et al.*, 2020; Bloch-Johnson *et al.*, 2021; Xu and Koll, 2024). In their recent study, Bloch-Johnson *et al.* (2021) identified a non-linear relationship between Equilibrium Climate Sensitivity (ECS: see Chapter 1) and atmospheric CO_2 concentration, and found that a feedback-temperature dependence explained 69% of the sensitivity increase, primarily attributable to the response of the long-wave clear-sky feedback. This highlights the need to improve understanding of how both λ_{total} and individual feedbacks are influenced by temperature change. Here I utilise a conceptual energy balance model (EBM) to explore the latitudinal behaviour of λ_{total} under multiple mean climate states, both warmer and colder than the pre-industrial period, in order to quantify the relationship between feedback strength and temperature. In their 2024 paper, Booth, Goodwin and Cael quantify the magnitude of the ice sheet-albedo feedback, λ_{alb}, using the most recent deglaciation, from the LGM to the pre-industrial period (see Chapter 3). However, as noted, due to the nature of state dependence, this estimate cannot be directly applied to a warmer climate state, such as from the present day into the future. I therefore use this same EBM to evaluate how the geometry of the planet will reduce the ice sheet-albedo feedback and thus calculate an adjusted estimate for λ_{alb} applicable to future climate change from the present day.

Traditionally, the magnitude of λ_{total} ($Wm^{-2}K^{-1}$), is calculated using temporal changes in global or regional temperature (e.g. Dessler (2013)) and calculated using the following equation:

$$\lambda_{total} = \frac{\Delta(S_{out} + L_{out})}{\Delta T}$$

Equation 4.1

Where $\Delta(S_{out} + L_{out})$ is the total change in the outgoing shortwave and longwave radiation at the TOA (Wm^{-2}) over a given time interval, and ΔT is the global surface temperature anomaly (K). However, temporal variations in GMST are small for the historical period, on the order of just 1 K. Instead, I build on work by Goodwin and Williams (2023) and explore zonal latitudinal variations in λ_{total} with temperature which are much larger, thereby substantially improving the signal-to-noise ratio. By evaluating how λ_{total} varies spatially as the climate warms, this method has the added advantage of enabling the investigation of polar amplification, the phenomenon whereby the temperature response to forcing is greater at higher latitudes than low latitudes (Smith *et al.*, 2019). Polar amplification over both poles has been observed in historical observations, simulations of future climate, and paleoclimate reconstructions (Serreze and Barry, 2011; Pithan and Mauritsen, 2014; Nummelin, Li and Hezel, 2017; Forster *et al.*, 2021; Lee *et al.*, 2021). Polar amplification is thought to be driven by a combination of local feedbacks, particularly the surface albedo feedback, and changes in poleward heat transport (Huang, Xia and Tan, 2017; Previdi, Smith and Polvani, 2021). As both the magnitude and spatial patterns of energy transport changes and local feedbacks are thought to experience background state-dependence, polar amplification is also likely to be affected by the climate mean state. Therefore, in addition to exploring the relationship between temperature and global feedback strength, this study shall also investigate polar amplification and zonal changes in feedback strength under multiple mean states.

Furthermore, I utilise the knowledge gained regarding the relationship between temperature and feedback strength to then explore the implications of state dependence for long term future warming according to the Shared Socioeconomic Pathways (SSPs) which represent possible futures for our planet. The SSPs are part of an established scenario framework based on five narratives of plausible demographic, economic, and political global developments which would result in different future emissions (Riahi *et al.*, 2017). While the baseline SSP scenarios assume a lack of new future climate policy, they can be combined with mitigation targets defined by radiative forcing levels (Wm^{-2}) by the year 2100 (Gidden *et al.*, 2019). I utilise four illustrative scenarios in this study: SSP1-1.9, which assumes a world focused on sustainable development with 1.9 Wm^{-2} by the year 2100; SSP1-2.6, which also imagines a sustainable future but with 2.6 Wm^{-2} by the year 2100; SSP2-4.5, which imagines a world where socioeconomic trends follow historical patterns with 4.5 Wm^{-2} of radiative forcing by the year 2100; and SSP4-6.0, which assumes an increasingly divided and unequal world with 6.0 Wm^{-2} of radiative forcing by the year 2100.

In order to explore the implications of state dependence for long term climate change, I extend each of these SSPs beyond the year 2100 and project GMST until the year 9000 using the WASP model (see Chapter 1). Due to the significant role of ice sheets in global climate on millennial timescales, I also incorporate the adjusted estimate of the ice sheet-albedo feedback, λ_{alb}, based on the findings from Booth, Goodwin and Cael (2024), to also explore the influence of this key slow feedback on long-term warming, alongside state dependence.

4.2 Methodology

Here I set out the key methodology for this chapter. On a practical level, this chapter builds upon the work of Chapter 3 and applies the estimate for the magnitude of the ice sheet-albedo feedback into the future. Work is organised into the following stages:

i. An EBM is used to amend the estimate of λ_{alb} for the LGM (from Chapter 3) to future relevance by accounting for difference in background climate mean state.
ii. Using the EBM to explore changes in feedback strength with background state also facilitates the exploration of polar amplification under multiple mean states.

iii. The adjusted estimate of λ_{alb}, now appropriate for the present day, is applied to the WASP model (see Chapter 1 and 2) to project long term future warming under multiple SSP scenarios.

4.2.1 Extension to the Energy Balance Model

This work utilises an EBM, originally published by Goodwin and Williams (2023), which is explained in greater detail in section 1.3.2 of Chapter 1. Since the publication of Goodwin and Williams (2023), the EBM has been extended in several ways. In particular, the model redefines the albedo of a cloudy sky, $\alpha_{cloudy\ sky}$, so that clouds act to: reflect a fraction of the incident solar radiation into space; allow some radiation to pass through; and reflect a fraction of the outgoing shortwave radiation back downwards towards the Earth surface (Goodwin *et al.*, 2023). The model adopts an infinite series approach (e.g. Taylor et al., 2007) to calculate the global net upwards shortwave radiation above a cloudy sky as well as considering the separate directed and diffuse beams of shortwave radiation:

$$\alpha_{cloudy\ sky}(\phi) \approx \alpha_{cloud:dir}(\phi) + \overline{\alpha_{clear\ sky}}(\phi) \times \frac{\left(1-\alpha_{cloud:dir}(\phi)\right) \times \left(1-\overline{\alpha_{cloud}}\right)}{\left(1-\overline{\alpha_{clear\ sky}}(\phi) \times \overline{\alpha_{cloud}}\right)}$$

Equation 4.2

Where $\alpha_{cloudy\ sky}(\phi)$ is the zonal- and annual-mean albedo of cloudy sky with latitude; $\alpha_{cloud:dir}(\phi)$ is the local cloud albedo for directed solar radiation with latitude; $\overline{\alpha_{cloud}}$ is the global- and annual-mean albedo of cloud; and $\overline{\alpha_{clear\ sky}}(\phi)$ is the planetary albedo for clear sky conditions if the all of Earth's surface was the same as the surface at a given latitude. $\alpha_{cloud:dir}$ and $\overline{\alpha_{cloud}}$ are determined from observationally-based values of $\alpha_{cloudy\ sky}$, $\alpha_{clear\ sky}$, and $\overline{\alpha_{clear\ sky}}$, assuming that $\alpha_{cloud:dir}$ varies with latitude according to the solar zenith angle effect.

Furthermore, in order to account for the fact role of water vapour content from the surface to the TOA as a greenhouse gas, the model also includes an approximation of zonal- and annual-mean clear sky emissivity, $\varepsilon_{clear\ sky}$, as a function of surface temperature, T_s, surface radiative humidity, H_{rel}, and the height of the tropopause, z_{trop}, as follows:

$$\varepsilon_{clear\ sky} \approx A + B\ln H_{rel} + Cz_{trop} + \frac{D}{T_s}$$

Equation 4.3

Where A, B, C, and D are coefficients (Appendix C) based on the fitted relationship with observed climatology (Jones *et al.*, 1999; Hersbach *et al.*, 2018; Morice *et al.*, 2021; Mateus, Mendes and Pires, 2022; Goodwin *et al.*, 2023).

4.2.2 Multiple mean states

To simulate a pre-industrial steady state, the values for $\kappa_{eff}(\phi)$, $f_{CA}(\phi)$, $f_{CI}(\phi)$, and $R_{solar}(\phi)$ (Figure 1.7) are imposed in the above EBM and set the initial temperature is set to $T_s(\phi) = 273.25\ K$ for all latitudes. The heat capacity is set as $c = 4.2 \times 10^8$ JK^{-1}m^{-2} which corresponds to a 150m deep surface ocean mixed layer covering 70% of Earth's surface. For all simulations, the model is run to an initial steady state that represents the pre-industrial mean climate state.

For this study, I run 40 simulations to calculate: the global, $\overline{T_s}$, and zonal-mean surface temperature, $T_s(\phi)$; and the global, λ_{total}, and zonal effective climate feedback parameter, λ_ϕ, under multiple mean states. From a pre-industrial baseline ($\delta F = 0$), I run 20 simulations of a warmer world ($\delta F > 0$) and 20 simulations of a cooler world ($\delta F < 0$), with a step-wise change between each simulation. Each step constitutes an incremental change of 1 Wm^{-2} of radiative forcing. The model first calculates zonal values for surface temperature and climate feedback for each latitudinal band, with λ_{total} calculated as the area-weighted mean of all zonal estimates. I also calculate the global effective climate sensitivity, S, for all mean climate states, defined as the negative reciprocal of λ_{total}. S expresses the magnitude of climate feedbacks in terms of surface temperature change per unit of radiative forcing and as such is a useful variable for accessible communication.

Polar amplification of surface temperature is calculated for both the Northern and Southern Hemispheres for each mean state according to the following basic equation:

$$Polar\ Amplification = \frac{\Delta T_s(> 65°\ N\ or\ S)}{\Delta T_s(equatorial\ band)}$$

Equation 4.4

Where the equatorial band is defined as the zonal-mean between 15°S and 15°N.

4.2.3 Modelling state dependence and long-term warming

In order to quantify the relationship between λ_{total} and global mean surface temperature, $\overline{T_s}$, and therefore gain insight into the nature of background state dependence, I plot the ratio change in λ_{total} for all mean states relative to when $\overline{T_s} = 0$, against the global mean surface temperature anomaly, $\Delta\overline{T_s}$, as shown in Figure 4.1, and find the quadratic equation of best fit between the variables. The ratio change represents the change in λ_{total} for a warmer or colder mean state, relative to 'present day' conditions. As such, a higher 'ratio change' value indicates that λ_{total} is greater than present day, and vice versa. This relationship is specific to the simplified representation of the climate within the EBM. The best fit relationship is as follows:

$$\lambda_{total} = 0.0004986\Delta\overline{T_s}^{\,2} - 0.01148\Delta\overline{T_s} + 1.0157$$

Equation 4.5

The above equation 4.5 is then incorporated into the WASP model (see Chapter 1) in order to explore the implications of this relationship on future warming.

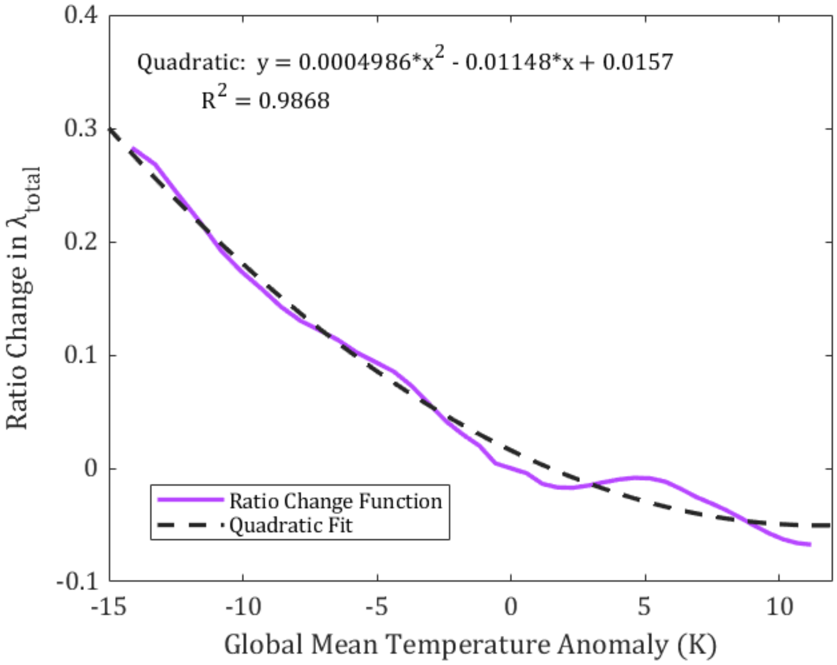

Figure 4.1: *Ratio change in λ_{total} for all mean states relative to when $\overline{T_s} = 0$, against the global mean surface temperature anomaly, $\Delta\overline{T_s}$ (solid purple), plotted with the quadratic best fit relationship (dashed black). R^2 value displayed as indicator of fit.*

Additionally, I incorporate the key findings from Booth, Goodwin and Cael (2024) relating to the long-term ice sheet-albedo feedback, λ_{alb}, which operates on a response timescale of approximately 3.6 ka (see Chapter 3). This study found a best estimate for the magnitude of λ_{alb} of 0.55 $Wm^{-2}K^{-1}$, indicating that λ_{alb} increased the equilibrium magnitude of λ_{total} by approximately 42%. However, this estimate only applies to a deglacial transition, where initial ice extent is large, and therefore the amplifying effect of future ice sheet retreat is likely to be smaller. As such, I adjust the estimate of λ_{alb} using the latitudinal EBM to reflect the reduced ice sheet extent at the pre-industrial compared to the LGM. As a simplified representation of the Earth system, the EBM is best placed to model large-scale ice sheet changes as opposed to high resolution cloud processes and as such is an appropriate tool for this adjustment. The adjustment is based on the CESM2 estimate of effective radiative forcing (ERF) for the LGM of -5.2 Wm^{-2} from Zhu and Poulsen (2021). I apply this estimate to the above energy balance model to estimate the change in λ_{total} from $\delta F = 0$ to $\delta F = -5.2$ Wm^{-2}. I apply this adjustment to calculate a new, reduced estimate for the magnitude of λ_{alb} at the pre-industrial era of 0.31 ±0.09 Wm^{-2}K^{-1}. This best estimate and uncertainty are used as the basis for randomly-generated, normally-distributed input parameters for the ice sheet-albedo feedback within the prior ensemble.

In order to explore long-term future warming, I modify the WASP model so it is capable of running and storing long time series on O(10,000) years. In doing so, I reduce the number of time steps to 2 per year and run the model to the year 9000 with decadal outputs. I explore future warming under multiple SSP scenarios: SSP1-1.9, SSP1-2.6, SSP2-4.5, and SSP4-6.0. Each SSP scenario follows the prescribed radiative forcing and atmospheric CO_2 concentration pathways used in the Reduced Complexity Model Intercomparison Project (Nicholls *et al.*, 2020a; Nicholls *et al.*, 2020b; Nicholls *et al.*, 2021). For each scenario, I run the model in two modes: where equation 4.5 (representing state dependence) and the ice sheet-albedo feedback are included; and where neither are included, in order to quantify the impact on future warming. I generate a prior ensemble of 5 million simulations for each scenario and each mode, producing posterior ensembles of approximately 3500 simulations each. Each ensemble member is given a weighting dependent on relative agreement with the automatic acceptance limit imposed on the cost function (see Chapters 1 and 2).

4.3 Results

4.3.1 Surface temperature

Figure 4.2 depicts the relationship between global mean surface temperature anomaly, $\Delta\overline{T_s}$, and the anomaly in the radiative forcing from carbon dioxide relative to pre-industrial levels, δF in the latitudinal EBM. A decrease of 20 W/m^2 in radiative forcing results in approximately 14.1 K of cooling, compared to only 11.2 K of warming for an increase in radiative forcing of 20 W/m^2. The relationship between radiative forcing and temperature is therefore non-linear and gently slopes with increasing radiative forcing. This indicates that with each increasing unit of radiative forcing from CO_2, there is a diminishing impact on global mean temperature which reflects the changing extent of the cryosphere. With global warming, the cryosphere shrinks, reducing the amplifying potential of the snow and ice albedo feedback and resulting in the relationship of diminishing returns with global temperature.

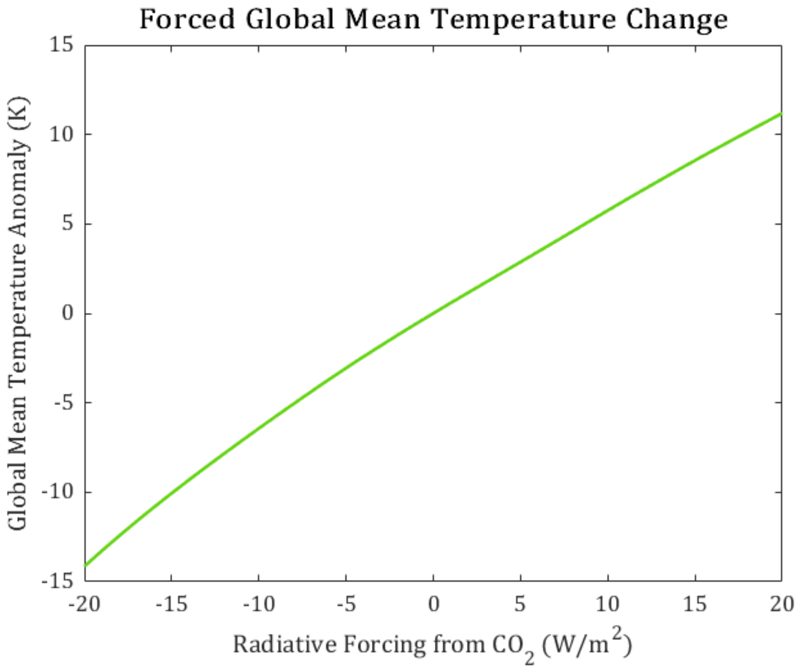

Figure 4.2: *Global mean temperature anomaly with change in radiative forcing from CO_2.*

4.3.2 Climate feedback parameter

Figure 4.3 depicts the relationship between the global mean temperature anomaly, $\Delta\overline{T_s}$, and the total climate feedback parameter, λ_{total} (figure 4.3a), and effective climate sensitivity, S (figure 4.3b) in the latitudinal EBM. The two variables are negative reciprocals of each other, explaining the similarity between the two plots. The relationships between temperature change and both λ_{total} and S are distinctly non-linear with two obvious peaks at approximately -5 K and +6 K temperature change. Overall, there is a change in the magnitude of λ_{total} of approximately 0.7 $Wm^{-2}K^{-1}$ for a temperature change of approximately 25.6 K. The trend is reversed for S which shows an overall change of ~0.34 KWm^{-2} for the same interval of temperature change.

It should be noted here that the model variables of λ_{total} and S are not perfect representations of reality, and some aspects are not considered in the calculation of these variables. Nevertheless, the behaviour of these variables in the model can give us valuable information about key earth system feedbacks. The overall decrease in S with warming shown here may initially be confusing for some readers who may expect higher estimates for climate sensitivity in warmer mean climatic states (Caballero and Huber, 2013; von der Heydt and Ashwin, 2017; Farnsworth *et al.*, 2019; Zhu, Poulsen and Tierney, 2019; Anagnostou *et al.*, 2020; Cael and Goodwin, 2023). In the case of this model, the decrease in S reflects the reduction in the global mean clear-sky surface albedo as surface cover changes from sea/land-ice to ocean/ vegetation. The rate of increase accelerates at higher mean temperatures as the sea/land ice area per unit of latitude shrinks for higher latitudinal bands. With a smaller cryosphere, the Earth indeed becomes less sensitive to perturbation as the relative influence of the snow and ice albedo feedback is minimised. Crucially, for each stepwise change in radiative forcing from CO_2, the model is run to equilibrium and timescale is ignored, as opposed to a transient system where feedback magnitude evolves over time.

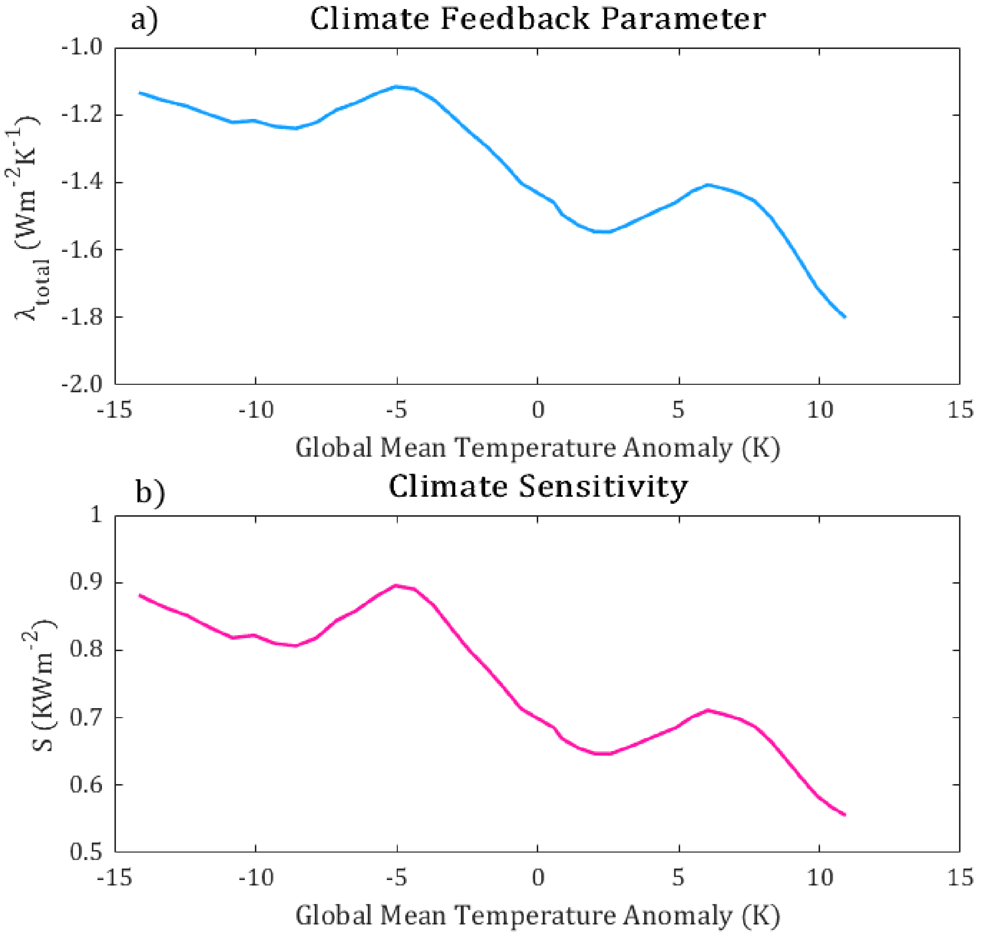

Figure 4.3: *Relationship between **a**) total climate feedback parameter and **b**) effective climate sensitivity, S, with the global mean temperature anomaly relative to a pre-industrial equivalent baseline. In this study, λ and S do not reflect a present-day real world, but rather are correct for small perturbations in a theoretical climate state that is initially equilibrated at the given radiative forcing.*

Whilst figure 4.3 explores λ as a global mean, figure 4.4 depicts eight illustrative distributions of the effective climate feedback parameter, λ, by latitude, with varying degrees of change in radiative forcing relative to pre-industrial levels in the latitudinal EBM. Scenarios are colour-coded such that deeper shades of red indicate an increase in radiative forcing and blue indicates a decrease. In all radiative forcing scenarios, the magnitude of λ in the low to mid latitudes shows minimal change with a magnitude of approximately -1.8 $Wm^{-2}K^{-1}$ at the equator, -2.03 ±0.05 $Wm^{-2}K^{-1}$ at Southern Hemisphere mid-latitudes, and -2.2 ±0.5 $Wm^{-2}K^{-1}$ for mid-latitudes in the Northern Hemisphere. The difference in λ between the low and mid latitudes reflects the presence of the Intertropical Convergence Zone of heavy cloud over the equatorial band which slightly increases sensitivity to temperature change relative to the clear sky conditions of the mid latitudes.

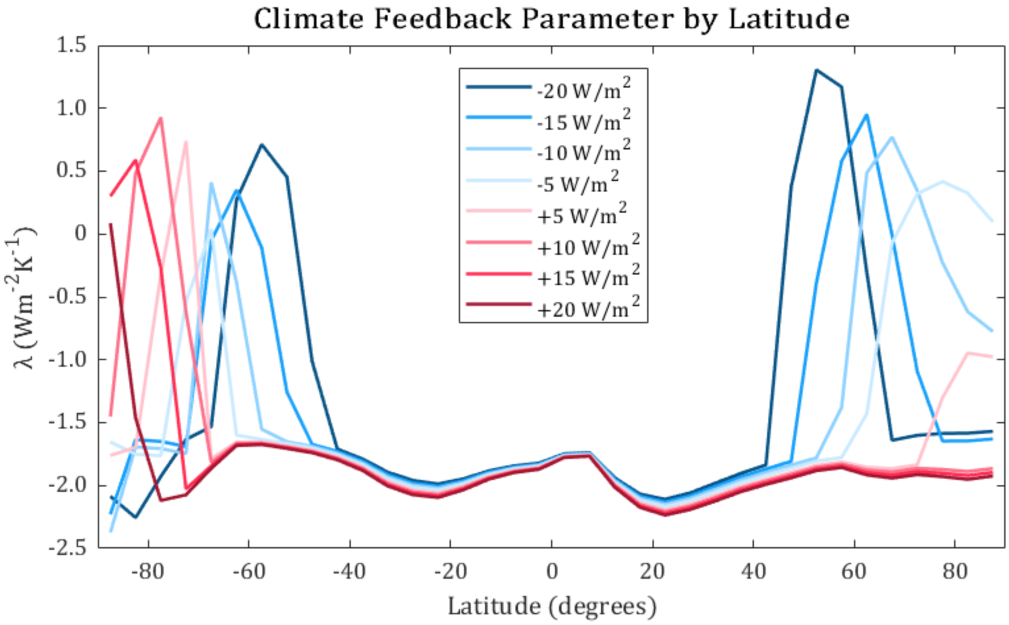

Figure 4.4: *Effective climate feedback parameter by latitude for eight sample simulations. Colour indicates the equilibrated climate mean state with a change in radiative forcing relative to a pre-industrial climate state. Red colours indicates an increase in radiative forcing (warmer mean state), and blue a decrease (cooler mean state). Darkness of colour represents the magnitude of anomaly.*

In both hemispheres, there is a sharp increase in λ in the high latitudes, the position of which shifts poleward with increasing radiative forcing and mean temperature. This poleward shift reflects the changing ice and snow extent with temperature and the subsequent impact on surface albedo. Where the value of λ increases, this indicates a high sensitivity to temperature change in the latitudinal bands that transition between ice growth and melting with small swings in surface temperature. In the colder climates (reduced radiative forcing: dark blue, figure 4.4), λ returns to its baseline level at the South Pole, indicating the stability of the Antarctic ice sheets; temperature rise would need to be significant to trigger any melting at these latitudes meaning sensitivity to temperature change is limited. However, as the global mean background temperature increases, the southern hemisphere ice sheets become more sensitive to small temperature variations as they shift closer to a melting threshold and possible collapse, as evidenced by the rise in λ at high southern latitudes under the warmer climate scenarios (increased radiative forcing: dark red, figure 4.4).

Contrastingly, this differs in the Northern Hemisphere. There is a steep increase in λ at 45-70°N in the coldest climates (blue: figure 4.4), to reflect the changing extent of snow and ice cover south of the Arctic Circle, but in warmer mean climates (red: figure 4.4) the northern hemisphere is increasingly insensitive to temperature change as Arctic sea ice and high latitudinal snow cover such a small area that the influence over global climate is increasingly limited. Indeed, the Arctic is expected to be consistently ice-free in summer by the mid-21st century according to most emission trajectories (Notz and Community, 2020; Kim *et al.*, 2023; Jahn, Holland and Kay, 2024).

4.3.3 Polar amplification

Figure 4.5 shows the relative temperature change at high latitudes relative to the equator in both the northern and southern hemispheres for different background mean global temperatures above and below the pre-industrial baseline, in the latitudinal EBM. In the northern hemisphere, the polar amplification factor is highest (~3.3: green, figure 4.5) for a temperature anomaly of -5 to -6 K, which mirrors the first peak shown in figure 4.3, and is consistent with reconstructed temperatures at the LGM (Annan and Hargreaves, 2013; Tierney *et al.*, 2020b; Annan, Hargreaves and Mauritsen, 2022). This peak represents the point at which northern hemisphere snow and ice extent is particularly sensitive to small changes in temperature and is undergoing rapid melting, driving an amplifying snow and ice albedo feedback which increases the relative temperature difference between high and low latitudes in the north. For increasing temperatures, polar amplification in the northern hemisphere rapidly declines to a factor of ~2 for a temperature anomaly greater than +4 K. This reduction reflects the shrinking extent of the cryosphere in the northern hemisphere with warming that decreases the amplification of polar temperature relative to the equator. The fact that the EBM finds Northern Hemisphere polar amplification peaking at an LGM state is consistent with the extensive literature demonstrating the major contribution of Northern Hemisphere ice sheets to the most recent deglacial transition, building confidence in the model skill (Batchelor *et al.*, 2019; Obase, Abe-Ouchi and Saito, 2021; Quiquet *et al.*, 2021; Bouttes *et al.*, 2023).

On the other hand, the southern hemisphere shows a different trend. In cooler background climates, polar amplification is relatively low as the southern hemisphere cryosphere is stable and insensitive to small temperature variations. However, as the background climate warms, the high latitudes begin to undergo increasingly high rates of temperature change compared to the equator, eventually reaching a peak of ~3.7 for a temperature anomaly of +5.5 K (figure 4.5: purple), which matches the second peak in figure 4.3. At this point, the southern hemisphere cryosphere is experiencing its fastest rate of collapse and melting rates are high, driving a strong temperature difference between high and low latitudes. In increasingly warm background climates, polar amplification in the southern hemisphere begins to decline again as the cryosphere shrinks and has a declining influence on global climate sensitivity (figure 4.3b).

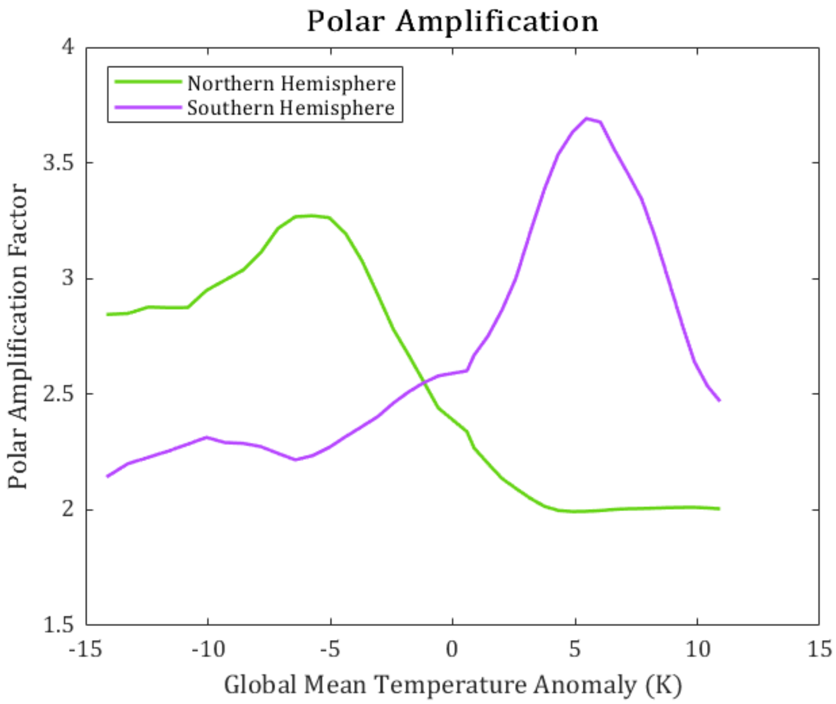

Figure 4.5: *Polar amplification factor for the Northern Hemisphere (green) and Southern Hemisphere (purple) according to the global mean temperature anomaly relative to a pre-industrial climate state.*

4.3.4 Implications for future warming

In this study I utilise the adjusted estimate for λ_{alb} and equation 4.5 to generate a posterior ensemble of WASP projections of future warming. Figure 4.6 displays the WASP projections of GMST anomalies relative to the pre-industrial era from 1850 to the year 9000 based on four illustrative SSP scenarios and highlights the implications of state dependence and the ice sheet-albedo feedback on the trajectory of future warming. In all scenarios, the radiative forcing pathway is prescribed until the year 2300 and so the trajectory of projected warming is almost identical for both modes until this point. All scenarios simulate a rapid rise in global temperatures from the year 1850 until the mid-21st century, as consistent with observed warming. Figure 4.6a shows SSP1-1.9 which predicts a median peak warming of 1.5 K to occur around the year 2030 before rapid cooling over the next century and then gently stabilising at a median temperature anomaly of approximately 0.9 K by the year 2400. Similarly, figure 4.6b depicts SSP1-2.6 which simulates a median peak warming of 1.8 K around 2050 before quickly cooling to 1.4 K by the year 2400. As expected, figures 4.6c and

4.6d show considerably higher peak warming and stabilisation at higher mean temperatures than the more sustainable scenarios. In figure 4,6c, SSP2-4.5 finds a median peak warming of 2.9 K at the year 2200, with a decrease to 2.7 K by 2400. In SSP4-6.0, depicted in figure 4.6d, temperatures reach a median of 3.8 K by 2200, with a small decrease to 3.7 K by the year 2500 before both modes begin to increase very gently in temperature again.

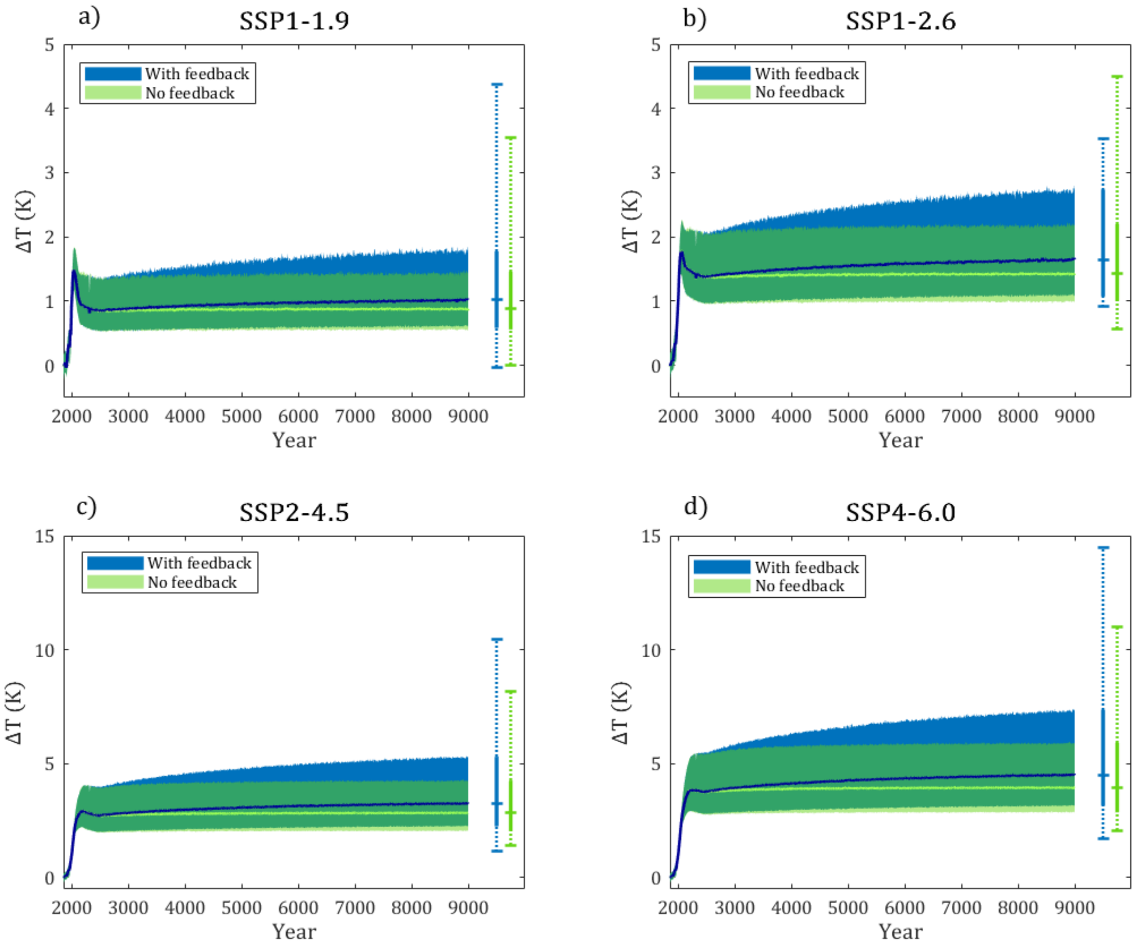

Figure 4.6: *WASP projections of future warming using Shared Socioeconomic Pathways both with state dependence and ice sheet-albedo feedback (blue), and without state dependence nor feedback (green)* **a**) *SSP1-1.9,* **b**) *SSP1-2.6,* **c**) *SSP2-4.5,* **d**) *SSP4-6.0. Ranges to the right of each plot indicate the best estimate (central tick), 66% confidence interval (solid line) and 95% confidence interval (dotted line) at the year 9000 for each scenario.*

Beyond the year 2300, the influence of the ice sheet-albedo feedback is evident in all scenarios with the model runs that include the feedback (Figure 4.6: blue) showing gently increases temperatures over the millennia, whilst model runs that do not include the ice sheet-albedo feedback (Figure 4.6: green) display minimal temperature change beyond the year 2500. SSP1-1.9 estimates a median temperature anomaly of 1.0 K by the year 9000, with a 66% confidence interval of 0.58 – 1.8 K and a 95% confidence interval of 0 – 4.4 K when the ice sheet-albedo feedback is included (Figure 4.6a: blue). This compares to a best estimate of 0.88 K by the year 9000 when the feedback is not included, with a 66% confidence interval of 0.56 – 1.5 K and 95% confidence interval of 0 – 3.5 K (Figure 4.6a: green). SSP1-2.6 estimates a median temperature anomaly of 1.6 K by the year 9000, with a 66% confidence interval of 1.0 – 2.7 K and a 95% confidence interval of 0.91 – 3.5 K when the ice sheet-albedo feedback is included (Figure 4.6b: blue). This compares to a best estimate of 1.4 K by the year 9000 when the feedback is not included, with a 66% confidence interval of 1.0 – 2.2 K and 95% confidence interval of 0.57 – 4.5 K (Figure 4.6b: green).

SSP2-4.5 estimates a median temperature anomaly of 3.2 K by the year 9000, with a 66% confidence interval of 2.3 – 5.3 K and a 95% confidence interval of 1.1 – 10.5 K when the ice sheet-albedo feedback is included (Figure 4.6c: blue). This compares to a best estimate of 2.8 K by the year 9000 when the feedback is not included, with a 66% confidence interval of 2.1 – 4.3 K and 95% confidence interval of 1.4 – 8.2 K (Figure 4.6c: green). SSP4-6.0 estimates a median temperature anomaly of 4.5 K by the year 9000, with a 66% confidence interval of 3.1 – 7.4 K and a 95% confidence interval of 1.7 – 14.5 K when the ice sheet-albedo feedback is included (Figure 4.6d: blue). This compares to a best estimate of 3.9 K by the year 9000 when the feedback is not included, with a 66% confidence interval of 2.9 – 5.9 K and 95% confidence interval of 2.1 – 11.0 K (Figure 4.6d: green).

Table 4-1: *Impact of ice sheet-albedo feedback and state dependence on WASP projections of future warming, according to four Shared Socioeconomic Pathways expressed as the absolute GMST difference (ΔT) and percentage difference in GMST (%) between the two modes at the calendar years 3000, 5000, 7000, and 9000. Both the ensemble best estimate (50th percentile) and 66% confidence interval (17th to 83rd percentile) are displayed.*

SSP	Percentile	Year 3000		Year 5000		Year 7000		Year 9000	
		ΔT (K)	%	ΔT (K)	%	ΔT (K)	%	ΔT (K)	%
1-1.9	17th	0.03	+5.1	0.04	+6.6	0.05	+8.3	0.02	+4.1
	50th	0.05	+5.4	0.07	+8.4	0.13	+14.7	**0.14**	**+16.3**
	83rd	0.10	+7.7	0.16	+11.3	0.26	+18.2	0.31	+21.3
1-2.6	17th	0.04	+4.5	0.06	+6.4	0.08	+8.6	0.07	+7.3
	50th	0.05	+3.8	0.11	+8.0	0.17	+12.1	**0.22**	**+15.4**
	83rd	0.12	+5.8	0.30	+13.9	0.40	+18.4	0.53	+24.3
2-4.5	17th	0.08	+3.9	0.16	+7.8	0.15	+7.4	0.20	+9.5
	50th	0.08	+2.9	0.25	+8.7	0.33	+11.6	**0.41**	**+14.3**
	83rd	0.21	+5.1	0.65	+15.6	0.83	+19.5	1.04	+24.4
4-6.0	17th	0.10	+3.4	0.19	+6.8	0.22	+7.5	0.28	+9.9
	50th	0.09	+2.3	0.32	+8.1	0.46	+11.5	**0.58**	**+14.7**
	83rd	0.26	+4.6	0.85	+14.8	1.17	+19.9	1.43	+24.1

The difference between the ensembles with the ice sheet-albedo feedback and without is made more explicit in table 4.1 which shows both the absolute- and percentage-change between the two ensemble modes at specific years into the future. All scenarios find increased long term future warming when the ice sheet-albedo feedback is included, with an increasing differential over time. Under SSP1-1.9, the ice sheet-albedo feedback increases median GMST change by 16.3% by the year 9000, which equates to a difference of 0.14 K. The impact on the 83rd percentile is greater, with a percentage change of 21.3%, compared to the change in the 17th percentile, which is just 4.1%, suggesting greater uncertainty at the upper bound of the range when the feedback is included. The narrative is similar for the other SSP scenarios. Under SSP1-2.6, the ice sheet-albedo feedback increases the median GMST change by 15.4% (0.22 K), and the impact on the upper bound (24.3%) is greater than the lower bound (7.3%). The additional median warming caused by the feedback is estimated at 0.41 K (14.3%) for SSP2-4.5, and 0.58 K (14.7%) for SSP4-6.0, whilst the percentage change in the upper and lower bounds shows a similar trend to SSP1-1.9 and SSP1-2.6.

4.4 Discussion

4.4.1 The impact of background state on climate feedbacks and polar amplification

By evaluating the spatial trends in the magnitude of λ_{total} using latitudinal variations in GMST, we gain crucial insights into the role of the cryosphere in driving changes in climate feedback strength under multiple mean states. I find that the relationship between background mean state and the global climate feedback parameter is distinctly non-linear and this is likely linked to the changing latitudinal extent of the cryosphere. The two peaks observable in λ_{total} (Figure 4.3a), S (Figure 4.3b), and polar amplification of the southern hemisphere (Figure 4.5: purple) and northern hemisphere (Figure 4.5: green) all occur at approximately $\Delta\overline{T}_S = -5\ K$ and $\Delta\overline{T}_S = 6\ K$ which correspond to the global temperatures at which the cryosphere is most sensitive to small zonal temperature variations in the model (Goodwin and Williams, 2023). This also aligns with estimated GMST at the LGM according to palaeoclimate reconstructions (Tierney *et al.*, 2020b; Annan, Hargreaves and Mauritsen, 2022). At zonal- and annual mean temperatures of approximately $\Delta T_S \leq -5\ K$, the cryosphere entirely dominates the clear-sky albedo across all seasons, whilst at approximately $\Delta T_S \geq 6\ K$, there is functionally no Northern Hemisphere cryosphere within the model as it no longer affects the annual mean clear-sky albedo. The Southern Hemisphere has drastically reduced by $\Delta T_S \geq 10\ K$ (Figure 4.4). These turning points are clearly reflected in the results and this highlights the notable influence that zonal changes in the cryosphere can have on global sensitivity to temperature change. Where the cryosphere is close to a melting threshold, it is most sensitive to temperature fluctuation, and this increases the magnitude of local climate feedbacks. However, beyond this critical threshold, the impact of the cryosphere on both local feedbacks and the global total climate feedback parameter is relatively reduced as the smaller ice extent has a diminishing influence on the global climate. This result further highlights the need to better understand possible tipping points in the earth system, especially involving Greenland and West Antarctic ice sheets, which carry the risk of major sea level rise, resulting in devastating impacts for societies, economies, and ecosystems worldwide (Box *et al.*, 2022; Dietz and Koninx, 2022; Lenton *et al.*, 2024).

The important role of the cryosphere in the global climate system and vulnerability of the polar regions to climate change is further supported here by modelled evolution in polar amplification with change in background state in the latitudinal EBM (Figure 4.5). Polar amplification of the northern hemisphere rapidly reduces at $\Delta\overline{T_s} > -4\ K$ as the critical melting threshold has been crossed, and the northern cryosphere begins to shrink. The increased sensitivity to temperature fluctuation in the northern hemisphere compared to the southern hemisphere is likely a consequence of the presence of sea ice within the Arctic Ocean which has been shown to be more susceptible to melting than snow cover or the land based ice sheet of the Antarctic, and the cooling effect of the Antarctic Circumpolar Current which limits the poleward transport of heat in across the Southern Ocean (Letterly, Key and Liu, 2018; Holland, Nicholls and Basinski, 2020). The model's ability to recreate the weakening of Northern Hemisphere polar amplification in warmer climates provides independent verification of the role of ice sheets in glacial-interglacial transitions, and increased confidence in the use of the EBM to calculate an adjusted value for the strength of the ice sheet-albedo feedback for the present-day climate state. Whilst polar amplification of the southern hemisphere is low at cooler mean states, this reflects the stability of the Antarctic ice sheet. Once $\Delta\overline{T_s} > 6\ K$, the southern cryosphere also begins to experience extensive collapse and decline with an accompanying decline in influence on global climate sensitivity at equilibrium, and polar amplification also declines as a result. The latitudinal shift in the zonal climate feedback parameter under cooler and warmer mean states (Figure 4.4) further supports this.

4.4.2 Implications for long term climate change

By utilising the findings from the EBM to project long term temperature change using the WASP model, we can see how a state-dependent ice sheet-albedo feedback could amplify human-induced climate change for millennia to come. The inclusion of the feedback increases GMST by an average of 15% across all scenarios, which translates to a substantial level of warming for the high emission scenarios (Table 4.1). This reiterates the necessity of reaching net zero emissions as soon as possible and for climate change mitigation to be prioritised as a matter of urgency to avoid the consequences of the higher risk, high emission scenarios. It should be noted that the future projections depicted in this study reflect the global mean, and warming is expected to be amplified at the poles. Indeed, for a global temperature anomaly of ~ 5.5 K, which is compatible with SSP4-6.0, the EBM expects the southern hemisphere to experience a polar amplification factor of ~3.7, which would translate to a local temperature increase of more than 20 K compared to the pre-industrial era (Figure 4.5). Such a dramatic temperature rise could carry the possible risk of the destabilisation of not only the West Antarctic Ice Sheet, but potentially the East Antarctic Ice Sheet which holds 52m sea-level-equivalent (Armstrong McKay *et al.*, 2022; Stokes *et al.*, 2022). Considerable uncertainty persists surrounding the sensitivity of the East Antarctic Ice Sheet and more research is needed to better understand this low-likelihood but high-impact tipping point.

4.5 Conclusions

As simplified representations of the earth system, the results from WASP and the EBM used in this study do not perfectly reflect reality but do provide useful insights into the relationships between components of Earth's climate system and Earth's energy budget. Whilst these results suggest a non-linear decrease in the magnitude of the global climate feedback parameter in warmer mean states, this reflects the dominance of the cryosphere within the model, and the diminishing influence of the snow-albedo feedback as ice extent is reduced with warming. An exploration of the climate feedback parameter by latitude shows a more nuanced picture, with local climate feedbacks becoming more amplifying when close to critical melting thresholds.

Understanding the relationship between temperature and feedback strength is important for the accurate prediction of future climate change and my results provide new evidence for how an amplifying ice sheet-albedo feedback would increase long-term warming under all SSP scenarios. The influence of state-dependence is minimal relative to the ice sheet-albedo feedback in this model, but uncertainty is large on long timescales. Further work to explore and constrain other slow feedbacks and the potential impact of different tipping points is required to increase confidence in long term climate predictions.

Chapter 5 Conclusions

5.1 Summary

The overarching narrative of this thesis has focused on several under-investigated aspects of earth system dynamics with the aim of improving understanding and reducing uncertainty surrounding climate sensitivity via the quantification of the climate feedback parameter. Work has been structured around three objectives that have formed the basis of the three central chapters of this thesis:

Objective 1:

Constrain the magnitude of Earth's fast and multi-decadal feedbacks and quantify the pattern effect through probabilistic assessment

Objective 2:

Explore and constrain the magnitude of Earth's slow ice sheet-albedo feedback in the context of the most recent deglaciation

Objective 3:

Investigate Earth's climate feedbacks under different background mean climate states and explore the implications of the ice sheet-albedo feedback for long term climate change

---

This section shall bring together the key findings from Chapters 2, 3, and 4 for discussion in the context of the original research objectives. The spatial and temporal heterogeneity of Earth's climate feedbacks has been a central theme of this thesis. The assumption that climate sensitivity or any individual feedback is constant over time or space has been accepted as false by the research community and we now face the challenge of disentangling the immense non-linear complexity of the earth system so we can better understand and anticipate the future of our planet. This thesis has aimed to contribute towards this endeavour.

5.1.1 Fast and multi-decadal feedbacks

Chapter 2 was motivated by the findings of two studies, Goodwin (2021) and Goodwin and Cael (2020), who used the WASP model (see Chapter 1) to undertake a probabilistic assessment of Earth's feedbacks over multiple timescales using observations of GMST and OHC anomalies as likelihood filters. They found two peaks in the posterior probability distributions of the fast and multi-decadal feedbacks (Figure 2.1), meaning that the statistical plausibility of Earth's multi-decadal feedbacks being damping could not be ruled out, based on observational evidence. I aimed to build on their methodology to constrain the magnitude of Earth's multi-decadal feedbacks further, and in doing do, further constrain the magnitude of Earth's faster inter-annual feedbacks.

I repeated the method utilised by Goodwin (2021) and Goodwin and Cael (2020) (Method 1) and compared the results to the posterior ensembles extracted by two alternative methods of likelihood filter to ascertain the optimal statistical method of constraining Earth's fast and multi-decadal feedbacks using the WASP model. Instead of the HadCRUT5 observational dataset used in Method 1 (Morice *et al.*, 2021), the alternative methods (Methods 2 and 3) used a new forced temperature profile from Cael and Calafat (in review) as a temperature constraint. This record proved to be a substantial improvement as a constraint over the unmodified HadCRUT5 dataset as it meant that a simulation could be compared directly to the forced signal when determining agreement with historical temperature change, without the influence of random noise. Methods 2 and 3 further improved on Method 1 by utilising 1-year averages for the temperature anomalies in the likelihood filter, rather than the 20-year averages used in previous studies. This ensured that simulations would only be considered observation-consistent if they reproduced both the longer anthropogenic warming trend and the rapid inter-annual cooling response to volcanic activity. By targeting multiple timescales in the likelihood filter, Methods 2 and 3 successfully constrained the magnitude of Earth's fast and multi-decadal feedbacks with increased statistical certainty compared to Method 1.

The likelihood filter utilised by Goodwin (2021) and Goodwin and Cael (2020) in their probabilistic assessment incorporated a cost function that was used to determine consistency between a simulation and the chosen observational constraint. For the purpose of evaluation, this same cost function was used in both Methods 1 and 2, with each ensemble member weighted by the ratio of the cost function to a prescribed automatic assessment limit, meaning that simulations that more closely matched the observations were given a greater weighting in the posterior ensemble. However, the cost function assumes that each time step is independent, and this is a limitation as in reality, the global average temperature of one year will influence the global average temperature of the following year. Therefore, Method 3 aimed to rectify this by utilising a multivariate likelihood function to extract the posterior ensemble rather than a cost function. The covariance matrix that formed the basis of this likelihood function was based on observational data and ensured that individual years were no longer considered independent which offers a theoretical improvement in the statistical methodology. However, in practice, the computational challenges created by the new multivariate likelihood function meant that simulations from Method 3 could not be weighted in the same way as Methods 1 and 2 and all posterior ensemble members are considered equally likely. As expected, this had an impact on the results. Firstly, the results of Method 3 would suggest fast, inter-annual feedbacks are the driving amplifying influence on climate sensitivity, and that slower multi-decadal feedbacks are much weaker in magnitude and with limited consequence for global climate sensitivity (Figure 2.3). This directly contradicts the findings of CMIP5 and CMIP6 and all evidence pointing towards a significant multi-decadal pattern effect (Andrews, Gregory and Webb, 2015; Dong *et al.*, 2020; Zhou *et al.*, 2021; Chao, Muller and Dessler, 2022). It is therefore likely that the covariance matrix used in the multivariate likelihood function of Method 3 is overpowered and overemphasises the influence of fast feedbacks that operate on timescales of less than a year. Furthermore, Method 3 indicated a fairly equal likelihood of multi-decadal feedbacks being amplifying or damping, thereby offering limited improvement on Method 1 in this regard. If the computational challenges of the multivariate likelihood function could be overcome so that ensemble members could be weighted according to their agreement with the observed constraints, this could provide some improvement in accuracy.

Overall, Method 2, which utilised a cost function, 1-year averaged temperature anomalies, and the extracted forced temperature profile as a constraint, showed the greatest agreement between simulated and observed temperatures over the historical period. Method 2 successfully captured both the long-term trend and short-term inter-annual variability with narrow confidence bands throughout. This method gave a median estimate of 0.85 $Wm^{-2}K^{-1}$ for the magnitude of multi-decadal feedbacks, with a 66% confidence interval of 0.50 – 1.25 $Wm^{-2}K^{-1}$ (Figure 2.6) which supports the CMIP5 and CMIP6 models that simulate stronger amplifying multi-decadal feedbacks. Furthermore, Method 2 estimated that Earth's fast feedbacks have a median magnitude of 0.88 $Wm^{-2}K^{-1}$ with a 66% confidence interval of 0.43 – 1.23 $Wm^{-2}K^{-1}$ (Figure 2.5a). Although the range of magnitudes of fast and multi-decadal feedbacks were found to be similarly amplifying, there was a negative correlation between the two terms across the ensemble meaning that stronger fast feedbacks were accompanied by weaker multi-decadal feedbacks, and vice versa (Figure 2.5c). Nevertheless, all methods underestimated the total warming experienced during the historical period, a problem common amongst assessments of climate feedbacks based on the historical record (Gregory and Andrews, 2016; Knutti, Rugenstein and Hegerl, 2017; Dessler, 2020; Tokarska *et al.*, 2020; Meyssignac *et al.*, 2023; Mutton *et al.*, 2024). It is likely that the lack of slow feedbacks that operate on timescales longer than 20 years in this version of the WASP model could be to blame here and as such, later chapters of this thesis aimed to investigate Earth's slow feedbacks with the intention of rectifying this limitation. Future work should also update the radiative forcing estimates utilised in the prior ensembles of the WASP model to explore the implications for magnitude of Earth's fast and multi-decadal feedbacks.

5.1.2 Ice sheet-albedo feedback

Many studies have identified the limitations of the underrepresentation of Earth's slow feedbacks in assessments of climate sensitivity (Lunt *et al.*, 2010; von der Heydt *et al.*, 2016; Sherwood *et al.*, 2020; Tierney *et al.*, 2020a; Fabiano *et al.*, 2024). The instrumental record is too short to fully capture feedbacks that operate on timescales of more than a few decades, and this has repeatedly led to an underestimation of climate sensitivity when constrained by the historical observational record alone (Knutti, Rugenstein and Hegerl, 2017; Gregory *et al.*, 2020). Furthermore, it is important to consider how human activity could influence the global climate beyond the end of the 21st Century; excessive short-term thinking throughout the 20th Century has been a major factor in causing the climate emergency we now find ourselves in and we cannot afford to repeat the mistakes of previous generations and not consider the long-term future of our planet (Martínez Montero *et al.*, 2024). Chapters 3 and 4 of this thesis were therefore motivated by the desire to increase understanding of earth system dynamics on centennial to millennial timescales.

In particular, Chapter 3 aimed to calculate a quantitative estimate for the magnitude of the ice sheet-albedo feedback and the response timescale that this feedback operates over, using probabilistic assessment of proxy records for Earth's most recent deglaciation (Lambert *et al.*, 2012; Lambeck *et al.*, 2014; Köhler *et al.*, 2017; Baggenstos *et al.*, 2019; Osman *et al.*, 2021; Shackleton *et al.*, 2023). This estimate was generated under the assumption that the energy imbalance caused by ice sheet-albedo change can be considered either an internal feedback or an external source of radiative forcing within the energy budget equation. Under this premise, the magnitude of the total climate feedback parameter, λ_{total}, can be calculated either way, with the difference representing the magnitude of the ice sheet-albedo feedback, λ_{alb}. Using this methodology, a best estimate of 0.55 $Wm^{-2}K^{-1}$ was generated, with a 66% confidence interval of 0.45 - 0.63 $Wm^{-2}K^{-1}$ and a 95% confidence interval of 0.33 - 0.77 $Wm^{-2}K^{-1}$, indicating a distinctly amplifying effect (Figure 3.3a). Furthermore, the ensemble indicated that the inclusion of ice sheet-albedo feedback increases λ_{total} by ~42% at equilibrium (Figure 3.2c). When the radiative contribution of indirect pattern effects from ice sheet retreat were also accounted for, based on estimates from Cooper *et al.* (2024), the best estimate for the total ice sheet feedback increased to 0.86 $Wm^{-2}K^{-1}$, with a 66% confidence interval of 0.53 – 1.28 $Wm^{-2}K^{-1}$ (Figure 3.3a). Such a strong amplifying effect would have significant consequences for all components of the earth system on millennial timescales, highlighting the importance of ice sheets for the global climate. Of course, the precise radiative contribution of indirect ice sheet-climate interactions are very difficult to quantify, and their inclusion introduced considerable uncertainty to the assessment, highlighting the need for more data to fully quantify ERF and indirect pattern effects for this and other time periods in Earth's past.

Efforts to constrain the response timescale of the ice sheet-albedo feedback were limited by the use of a single time interval of just 18 ka, and the 66% confidence interval could only be constrained to 1.9 ka to 5.5 ka, with a best estimate of 3.6 ka (Figure 3.3b). However, the constraint benefits of evidence from multiple glacial cycles might be somewhat counteracted by the additional uncertainty that would be introduced from proxy records for further into Earth's history which tend to lack the high temporal resolution of the past 25 ka. There will be increasing opportunities to constrain the response timescale of ice sheet feedbacks as new records for radiative forcing and EEI are published.

Both the magnitude and timescale estimates generated in Chapter 3 are specifically applicable to the most recent deglacial transition as the initial ice sheet extent is an important factor in determining the relative influence of ice sheets on the global climate. I concluded that is likely that λ_{alb} will be weaker in the future as the extent of the Northern Hemisphere ice sheets is substantially smaller today than at the LGM, although the potential future significance of the Southern Hemisphere ice sheets cannot be ruled out. As the estimates generated in Chapter 3 could not be directly applied to the present day, Chapter 4 sought to calculate an adjusted estimate for λ_{alb} which could be applied to projections of future climate change so to explore the potential influence of ice sheets on long timescales into the future. Assuming -5.2 Wm^{-2} ERF for the LGM (Zhu and Poulsen, 2021), an adjusted estimate of 0.31 ±0.09 $Wm^{-2}K^{-1}$ for λ_{alb} was calculated using an EBM which was then used as an input parameter for the WASP prior ensemble. The results indicated that the ice sheet-albedo feedback increased GMST change by an average of 15% by the year 9000 across the four SSP scenarios modelled which translates to substantial warming for higher emission scenarios. The SSP scenarios are only prescribed until the year 2300 and so this study assumed no further human intervention beyond this point. This is of course a simplification, and we have very little understanding of how human civilisation will have evolved this far into the future and how the landscape of GHG emissions would change as a result, but the value of this result is not in producing a perfect prediction of the future, but rather to demonstrate the relative influence of the cryosphere on global temperatures and climate sensitivity. As both Figure 4.6 and Table 4.1 show, the ice sheet-albedo feedback was found to increase GMST change by the year 3000 by varying degrees across all ensembles suggesting that ice sheet retreat could start to amplify warming, however minimally, within the next few hundred years. One must again note the spatial heterogeneity of Earth's feedbacks and predicted warming; a small change in global mean temperature could still have significant impacts on regional and local scales (Mahlstein, Daniel and Solomon, 2013; Hansen and Sato, 2016; Arnell *et al.*, 2019). These findings emphasise the potential long-term consequences of following a high emission pathway with high cumulative emitted carbon and therefore the need to prioritise the goal of Net Zero in order to avoid high risk, low likelihood impacts for our planet (Allen *et al.*, 2009; IPCC, 2013; Matthews *et al.*, 2018; IPCC, 2021; Wood *et al.*, 2023).

5.1.3 Background state and latitudinal variation

Early chapters of this thesis centred primarily on the temporal heterogeneity of Earth's climate feedbacks with particular focus on global mean trends. There is however another key characteristic of Earth system dynamics that should be considered; feedbacks are not spatially-constant and certain feedbacks are intrinsically tied to latitudinal variation. Therefore, in addition to exploring the long-term implications of the ice sheet-albedo feedback for global temperatures under multiple future scenarios, Chapter 4 also utilised a conceptual EBM to explore the latitudinal behaviour of the total climate feedback parameter, and thus climate sensitivity, under multiple mean climate states, both warmer and colder than the present. As a simple model, the EBM is especially well-placed to investigate large-scale trends related to snow and ice albedo, providing crucial insights into the influence of the cryosphere on zonal and global feedback behaviour. Results from the EBM indicated that the relationship between the magnitude of λ_{total} and the background mean state is distinctly non-linear and strongly tied to changes in the latitudinal extent of the cryosphere, as evidenced by how global λ_{total} increased at global temperature anomalies where the cryosphere is most sensitive to small temperature fluctuations in the model (Figure 4.3a). The poleward latitudinal shift in local feedback strength with increasing temperature and radiative forcing further supported this (Figure 4.4). Furthermore, this result suggests that local snow and ice feedbacks will have a relatively strong amplifying influence in the immediate future as large areas of our Northern cryosphere are currently very close to their melting threshold (IPCC, 2019; Boers and Rypdal, 2021; Bochow *et al.*, 2023; ICCI, 2024). As temperatures increase further, we can therefore expect local feedbacks within the Southern cryosphere to become more powerful and more influential in driving global climate sensitivity as parts of Antarctica near their melting points (Rosier *et al.*, 2021; Lau *et al.*, 2023). This is supported by the rise in polar amplification within the Southern Hemisphere with global temperature anomalies of up to +6 K observable in Figure 4.5.

It should be reiterated that the EBM used in Chapter 4 is a simple representation of the earth system and the relative influence of surface albedo on global climatology is perhaps overpowered. This explains why the EBM found an overall decrease in both the modelled total climate feedback parameter, λ_{total}, and climate sensitivity, S, in warmer climates, which is not consistent with the many studies that predict higher climate sensitivity in warmer background states (Caballero and Huber, 2013; von der Heydt and Ashwin, 2017; Farnsworth *et al.*, 2019; Zhu, Poulsen and Tierney, 2019; Anagnostou *et al.*, 2020; Cael and Goodwin, 2023). Chapter 4 instead suggested that this decrease indicates that the overall contribution of snow and ice feedbacks to global climate sensitivity would decline with warming due to shrinkage of the cryosphere. Similarly, the EBM indicated that polar amplification of the Northern Hemisphere would decrease in warmer climates which is consistent with studies that predict a sea ice-free Arctic Ocean within the next few decades (Notz and Community, 2020; Kim *et al.*, 2023; Jahn, Holland and Kay, 2024).

5.1.4 Synthesis

This thesis has sought to reduce uncertainty surrounding the climate feedbacks with a consideration of the inherent heterogeneity in the temporal and spatial evolution of both the total climate feedback parameter and constituent components of this key parameter. Chapter 2 improved on previous studies to generate probabilistic estimates of the magnitude of both the fast and multi-decadal feedbacks with improved statistical certainty. Chapter 3 utilised proxy records to generate a probabilistic estimate of the magnitude and equilibrium response timescale of a key slow feedback: the ice sheet-albedo feedback. Finally, Chapter 4 estimated the magnitude of the total climate feedback parameter under multiple mean climate states both warmer and colder than today in order to gain insights into the state dependence of λ_{total}. Chapter 4 also used this gained knowledge to generate an adjusted estimate of the ice sheet-albedo feedback for the present day and applied this estimate to probabilistic projections of long-term warming under multiple emission pathways. As such, each chapter investigates a different aspect of Earth’s complex system of climate feedbacks, providing quantitative estimates, and contributing to the collective understanding of climate feedbacks and, therefore, climate sensitivity.

Naturally, this work is but a glimpse into the immense complexity of the system and there are numerous other components and factors to consider when attempting to understand climate sensitivity. Nonetheless, it should be noted that this work found each of the fast, multi-decadal, and slow ice sheet-albedo feedbacks to amplify warming and, in each case, this amplifying influence is substantial. I hope that the results from this thesis aid future efforts to understand our climate system and predict its future changes.

5.2 Policy implications & final remarks

The need to improve the quantification of climate sensitivity and key climate feedbacks goes beyond intellectual curiosity. There is an urgent necessity to develop greater certainty in our understanding of earth system dynamics to accurately anticipate the global and regional impacts of climate change on human populations and confidently prepare adaptation and mitigation plans accordingly. A key take away from the work of this thesis is the inevitability of ice sheet retreat over the next few centuries. The slow equilibrium timescales involved in ice sheet feedbacks are such that some impacts are now irreversible for centuries to millennia, even if we rapidly reach net negative emissions (IPCC, 2019; Gregory, George and Smith, 2020; Van Breedam, Goelzer and Huybrechts, 2020; Fox-Kemper *et al.*, 2021). Of course, this does not automatically mean that complete ice sheet collapse is now unavoidable, but we must be prepared for the consequences of some ice mass loss (Pattyn *et al.*, 2018; Hill, Gudmundsson and Chandler, 2024; Seroussi *et al.*, 2024).

The complete loss of the cryosphere would have severe implications for both human and natural ecosystems worldwide, and any degree of ice sheet retreat will have implications for other components of the earth system. Ice sheets interact with the local and global climate system through more ways than just albedo: meltwater output directly influences global ocean circulation; ice sheets affect local precipitation, temperature and wind patterns; and changes in ice mass can cause isostatic readjustment of the underlying lithosphere (Fyke *et al.*, 2018). As noted in Chapter 3, the interactions between ice sheets and the climate system can themselves compound the amplifying effect of ice sheet-albedo changes and further increase warming. Glacier river runoff supplies water for billions of people; as glaciers retreat, freshwater runoff may initially increase, but this supply will decline over time with potentially devastating impacts for water availability and food production for the regions that depend on this resource (Prasch, Mauser and Weber, 2013; Zhang *et al.*, 2015; Haeberli and Weingartner, 2020). Strong water management policies will be required to prevent water poverty, food scarcity, and increased water-related conflict (IPCC, 2019). Many regions are also dependent on the cryosphere for their livelihoods and cultural identity and cryosphere shrinkage is expected to have regional socioeconomic impacts (Xiao, Wang and Qin, 2015; Rasul and Molden, 2019; Tschakert *et al.*, 2019).

Perhaps the most concerning implication of ice sheet retreat for many human populations is global sea level rise from the transfer of previously land-based ice to the oceans, which will be compounded by thermal expansion as a result of ocean warming (Gregory *et al.*, 2019; Van Breedam, Goelzer and Huybrechts, 2020; Klose *et al.*, 2024). As of 2020, approximately 267 million people live within 2 metres above sea level, a number that is only expected to grow, with a disproportionate number located within tropical Asia and considered highly vulnerable to coastal flood risk (Hooijer and Vernimmen, 2021). In addition to coastal flooding, rising sea levels also increase the risk of: salinisation of coastal aquifers and agricultural land, exacerbating food insecurity; loss of coastal ecosystems such as tidal wetlands, coral reefs, and seagrasses; increased storm intensity and frequency; and coastal erosion with damage to property and infrastructure (Cazenave and Cozannet, 2014; Hinkel *et al.*, 2015; Mentaschi *et al.*, 2018; Elneel *et al.*, 2024; Mohanty, Mohapatra and Mohanty, 2024; Wang *et al.*, 2024). Like feedbacks, climate risks are interlinked and with each degree of additional warming, the likelihood of compound and cascading risks increases (Zscheischler *et al.*, 2018; IPCC, 2019). Multiple potential hazards should be studied in tandem to produce comprehensive risk management strategies for vulnerable regions with an emphasis on building community resilience (Gallina *et al.*, 2016; Lawrence, Blackett and Cradock-Henry, 2020; Simpson *et al.*, 2023).

This thesis has highlighted the ongoing uncertainty surrounding tipping points within the earth system; several high impact, low likelihood climate impacts resulting from abrupt climate responses cannot be ruled out at this stage, which strongly recommends a precautionary approach towards climate change mitigation policy (Brovkin *et al.*, 2021; Ritchie *et al.*, 2021; Wunderling *et al.*, 2024). At present, global climate finance is heavily targeted towards climate change mitigation (IPCC, 2022). This is not altogether a bad thing and strong mitigation policies will be required to reach net zero emissions, but it is important to acknowledge the need for adaptation and capacity-building for regions facing unavoidable impacts of climate change, and properly allocate funding accordingly (Mostafa, Rahman and Huq, 2016; Eriksen *et al.*, 2021). Whilst scientific efforts to further constrain climate sensitivity shall continue, some uncertainty will always persist and this should not be used as an excuse to further delay decisive action; the economic and human cost of historical inaction is already too high and the window of opportunity to secure a liveable future for all is narrow and closing (Sanderson and O’Neill, 2020; UNFCCC, 2023).

Appendix A

Prior distributions of model input parameters for WASP, used in Chapter 2 and 4.

	Input Parameter	**Prior Distribution**
λ_{Planck}	Planck feedback	Normal, μ = 3.2Wm^{-2}, σ = 0.2Wm^{-2}
λ_{fast}	Fast feedbacks	Uniform, min = -3.0Wm^{-2}, max = 1.0Wm^{-2}
τ_{fast}	Response timescale of fast feedbacks	Normal, μ = 8.9 days, σ = 0.4 days
λ_{md}	Multi-decadal feedbacks	Uniform, min = -3.0Wm^{-2}, max = 3.0Wm^{-2}
τ_{md}	Response timescale of multi-decadal feedbacks	Uniform, min = 20 years, max = 45 years
α_{CO2}	Radiative forcing coefficient for log change in CO_2	Normal, μ = 5.35Wm^{-2}, σ = 0.27Wm^{-2}
	Dimensionless uncertainty in N_2O radiative forcing	Normal, μ = 1.0, σ = 0.05
	Dimensionless uncertainty in CH_4 radiative forcing	Normal, μ = 1.0, σ = 0.07
	Dimensionless uncertainty in halocarbon radiative forcing	Normal, μ = 1.0, σ = 0.05
	Radiative forcing coefficient for volcanic aerosols	Normal, μ = -19.0Wm^{-2}, σ = -0.5Wm^{-2}
$\gamma_{SO_x}E_{SO_x}$	Radiative forcing from SO_x aerosols in 2020	Normal, μ = -0.31Wm^{-2}, σ = 0.11Wm^{-2}
$\gamma_{BC}E_{BC}$	Radiative forcing from black carbon aerosols in 2010	Normal, μ = 0.18Wm^{-2}, σ = 0.07Wm^{-2}
$\gamma_{NO_x}E_{NO_x}$	Radiative forcing from NO_x aerosols in 2010	Normal, μ = -0.032Wm^{-2}, σ = 0.016Wm^{-2}
$\gamma_{SOA}E_{NMVOC}$	Radiative forcing from Volatile Organic Compound aerosols in 2010	Normal, μ = -0.06Wm^{-2}, σ = 0.09Wm^{-2}
$\gamma_{OC}E_{OC}$	Radiative forcing from organic carbon in 2010	Normal, μ = -0.03Wm^{-2}, σ = 0.01Wm^{-2}
$\gamma_{NH_3}E_{NH_3}$	Radiative forcing from NH_3 aerosols in 2010	Normal, μ = -0.048Wm^{-2}, σ = 0.024Wm^{-2}
$-R_{aci:2011}$	Radiative forcing from indirect aerosol effects in 2010	Skew-normal, μ = -0.55Wm^{-2}, σ = 0.37Wm^{-2}, skew = -2.0
	Carbon exchange timescale between atmosphere and surface ocean mixed layer	Uniform, min = 0.5 years, max = 1.0 years

	Tracer exchange timescale surface ocean mixed layer to upper thermocline	Uniform, min = 5 years, max = 40 years
	Tracer exchange timescale surface ocean mixed layer to intermediate water	Uniform, min = 15 years, max = 60 years
	Tracer exchange timescale surface ocean mixed layer to deep ocean	Uniform, min – 100 years, max = 500 years
	Tracer exchange timescale surface ocean mixed layer to bottom water	Uniform, min = 400 years, max = 1500 years
$\boldsymbol{I_b}$	Atmosphere-ocean buffered carbon inventory	Uniform, min = 3100PgC, max = 3500PgC
$\boldsymbol{r_1}$	Ratio of surface warming at equilibrium: global near surface to global sea surface	Uniform, min = 0.20, max = 1.5
$\boldsymbol{r_2}$	Ratio of global whole-ocean warming to global sea surface warming at equilibrium	Uniform, min = 0.1, max = 1.0

Appendix B

Supplementary material for Chapter 3, which accompanied the following publication:

Booth, A., Goodwin, P., & Cael, B. B. (2024). Ice sheet-albedo feedback estimated from most recent deglaciation. Geophysical Research Letters, 51, e2024GL109953.

Introduction

Here we repeat our methodology from the main text, but using the record for Earth's Energy Imbalance (EEI) based on benthic δ18O data from Shackleton *et al.* (2023), instead of Baggenstos *et al.* (2019), and show there is minimal difference in the results regardless of which dataset is used as ΔN to calculate λ_{total}, λ_{alb}, or τ. We display the results using the alternative dataset for comparison with figures 1, 2 and 3 in the main text.

Text S1.

Figure S1a, b, and d use identical data to Figure 1a, b, and d in the main text, whilst Figure S1c displays the change in Earth's top-of-atmosphere energy imbalance, ΔN, over the past 18 ka, using data from Shackleton *et al.* (2023). The overall trend in ΔN shown in Figure S1c is very similar to that of Figure 1c, but with slightly greater uncertainty, slightly greater fluctuation from ~ 7.5 ka BP to present, and slightly reduced amplitude in the peaks and troughs over the full time series.

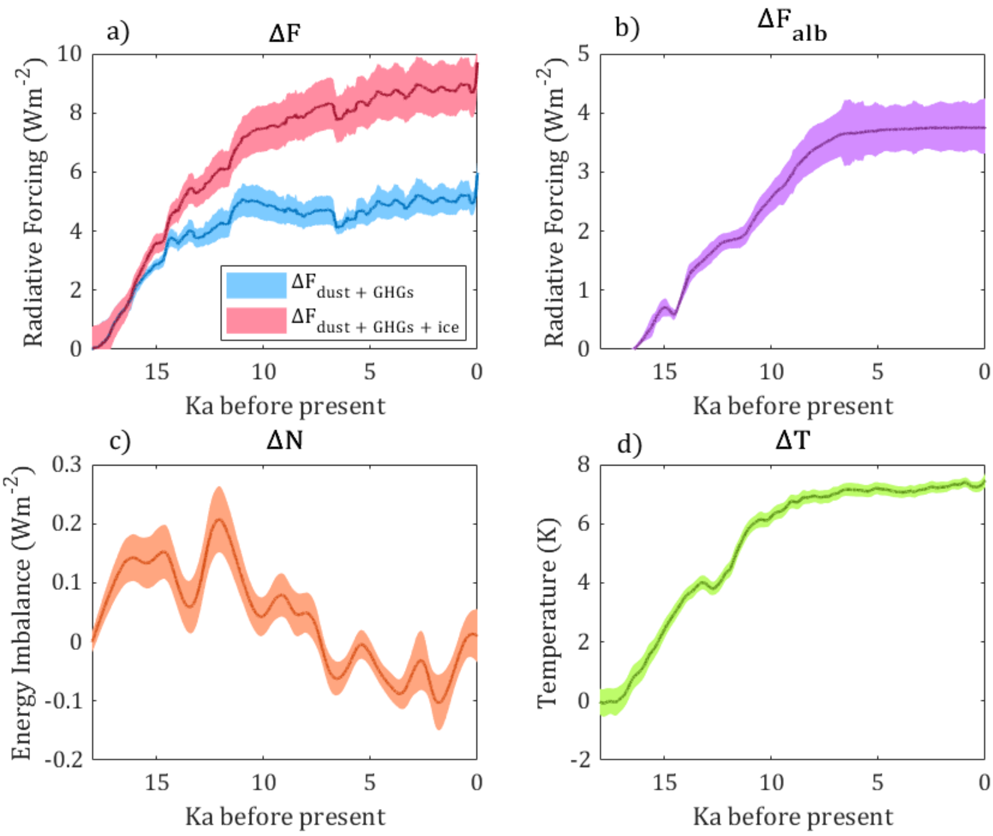

Figure S1. The components of the energy budget equation over the past 18 ka with 66% confidence intervals (shaded areas). All plots are displayed as anomalies relative to 18 ka BP **a)** Change in total radiative forcing when forcing from ice sheet-albedo change is included (pink) and excluded (blue) **b)** Change in total radiative forcing from ice sheet-albedo change, **c)** Change in Earth's Energy Imbalance, **d)** Global surface temperature anomaly.

Text S2.

Figure S2a shows the total climate feedback parameter, λ_{total}, when ice sheet-albedo change is treated as either a forcing (pink) or feedback (blue). Overall, both the overall trend and magnitude is almost identical to that shown in Figure 2a, which uses a different dataset to represent ΔN, indicating that the choice of dataset makes a negligible impact on the results. The same is the case for Figure S2b versus Figure 2b and Figure S2c versus Figure 2c, which are very similar.

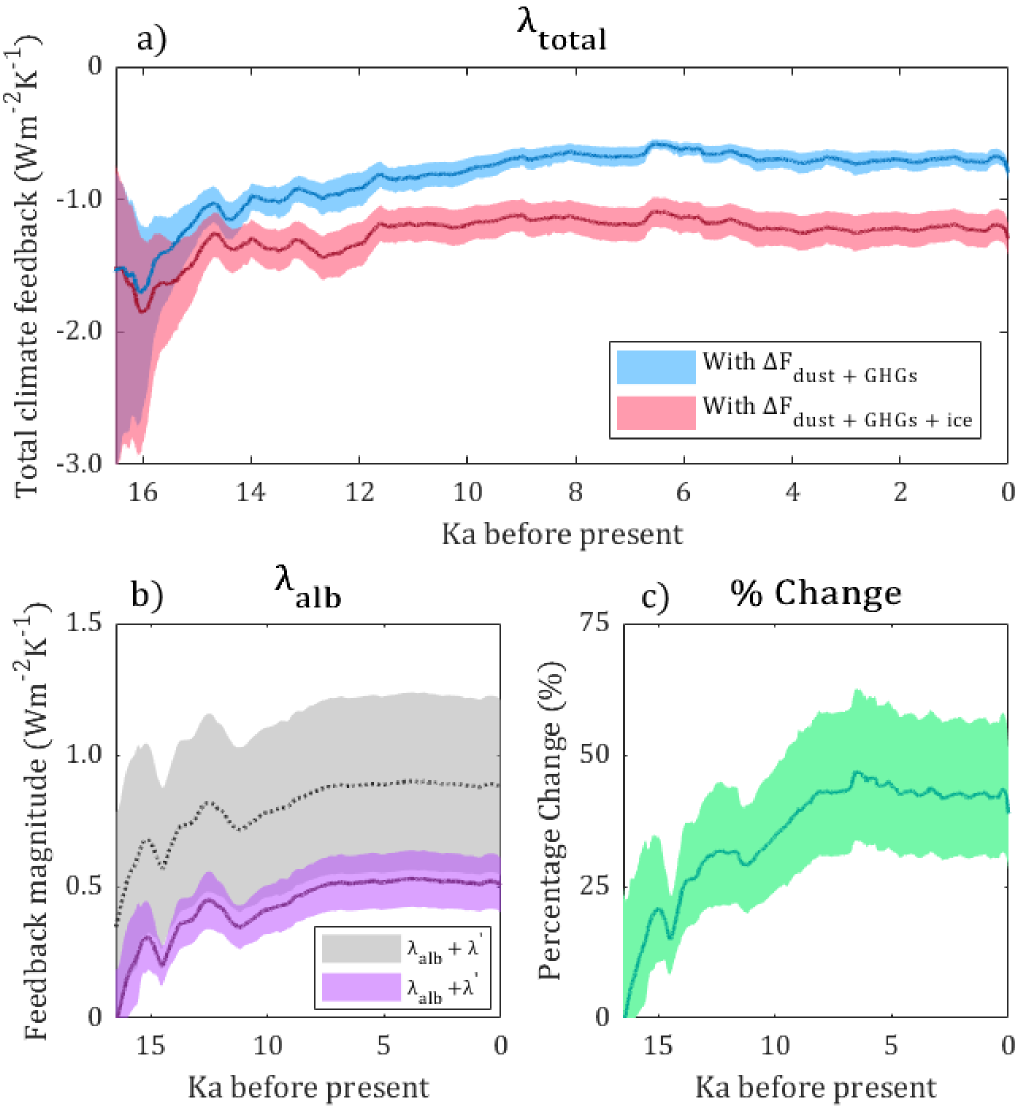

Figure S2. The magnitude of the effective climate feedback parameter, λ, over the past 16.5 ka with 66% confidence interval shaded **a)** total climate feedback parameter, $\boldsymbol{\lambda_{total}}$, when ice sheet-albedo is assumed to be a forcing (pink) or feedback (blue), **b)** ice sheet-albedo feedback, $\boldsymbol{\lambda_{alb}}$ (purple) and with pattern effect (grey), **c)** impact of the ice sheet-albedo feedback, $\boldsymbol{\lambda_{alb}}$, on the total climate feedback parameter, $\boldsymbol{\lambda_{total}}$, expressed as a percentage change.

Text S3.

Figure S3 displays the probability distributions for the magnitude (Figure S3a) and the response timescale (Figure S3b) of the ice sheet-albedo feedback, when ΔN is represented by data from Shackleton et al. (2023). For the magnitude of λ_{alb}, we find a best estimate of 0.55 Wm^{-2}K^{-1} with a 66% confidence interval of 0.45 – 0.64 Wm^{-2}K^{-1} and a 95% confidence interval of 0.32 – 0.77 $Wm^{-2}K^{-1}$. For the response timescale of the feedback, τ, we find a best estimate of 3.6 ka, with a 66% confidence interval of 1.8 ka to 5.6 ka and a 95% confidence interval of 0.5 ka to 9.7 ka.

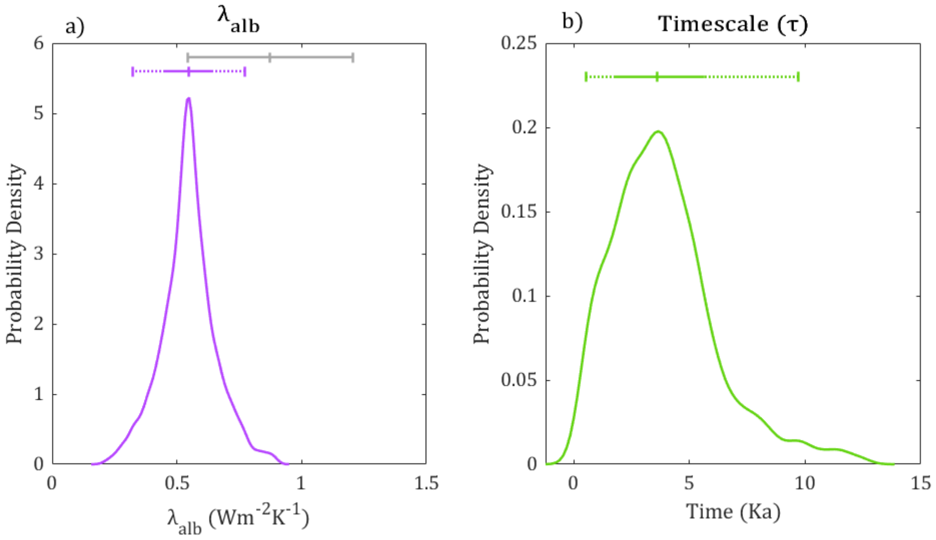

Figure S3. Probability density distributions for a) ice sheet-albedo feedback, $\boldsymbol{\lambda_{alb}}$, and b) the response timescale, τ, for $\boldsymbol{\lambda_{alb}}$. Uncertainty intervals are displayed above each graph. Solid line indicates 66% confidence interval, dotted line indicates 95% confidence interval. The best estimate and 66% confidence interval for $\boldsymbol{\lambda_{alb}} + \boldsymbol{\lambda'}$ is given by the grey solid line for comparison (Fig. S3a).

Appendix C

Coefficients used for statistical model fit for Equation 4.3 in Chapter 4. From supplementary material of Goodwin *et al.* (2023).

Coeff.	Estimate	SE	t-stat	p-value
A	0.272	0.122	2.22	0.0337
B	-0.0897	0.0212	-4.24	0.0001792
C (km^{-1})	-0.00329	0.00089	-3.70	0.000816
D (K)	242.96	10.01	24.27	3.55×10^{-22}

List of References

Abe-Ouchi, A. *et al.* (2015) 'Ice-sheet configuration in the CMIP5/PMIP3 Last Glacial Maximum experiments', *Geosci. Model Dev.*, 8(11), pp. 3621-3637.

Abrams, J.F. *et al.* (2023) 'Committed Global Warming Risks Triggering Multiple Climate Tipping Points', *Earth's Future*, 11(11), p. e2022EF003250.

Allen, M.R. *et al.* (2009) 'Warming caused by cumulative carbon emissions towards the trillionth tonne', *Nature*, 458(7242), pp. 1163-1166.

Allen, M.R., O.P. Dube, W. Solecki, F. Aragón-Durand, W. Cramer, S. Humphreys, M. Kainuma, J. Kala, N. Mahowald, Y. Mulugetta, R. Perez, M. Wairiu, and K. Zickfeld (2018) 'Framing and Context', in Masson-Delmotte, V., P. Zhai, H.-O. Pörtner, D. Roberts, J. Skea, P.R. Shukla, A. Pirani, W. Moufouma-Okia, C. Péan, R. Pidcock, S. Connors, J.B.R. Matthews, Y. Chen, X. Zhou, M.I. Gomis, E. Lonnoy, T. Maycock, M. Tignor, and T. Waterfield (ed.) *Global Warming of 1.5°C. An IPCC Special Report on the impacts of global warming of 1.5°C above pre-industrial levels and related global greenhouse gas emission pathways, in the context of strengthening the global response to the threat of climate change, sustainable development, and efforts to eradicate poverty*.

Anagnostou, E. *et al.* (2020) 'Proxy evidence for state-dependence of climate sensitivity in the Eocene greenhouse', *Nature Communications*, 11(1), p. 4436.

Andrews, T. *et al.* (2022) 'On the Effect of Historical SST Patterns on Radiative Feedback', *Journal of Geophysical Research: Atmospheres*, 127(18), p. e2022JD036675.

Andrews, T. *et al.* (2018) 'Accounting for Changing Temperature Patterns Increases Historical Estimates of Climate Sensitivity', *Geophysical Research Letters*, 45(16), pp. 8490-8499.

Andrews, T., Gregory, J.M. and Webb, M.J. (2015) 'The Dependence of Radiative Forcing and Feedback on Evolving Patterns of Surface Temperature Change in Climate Models', *Journal of Climate*, 28(4), pp. 1630-1648.

Annan, J.D. (2015) 'Recent Developments in Bayesian Estimation of Climate Sensitivity', *Current Climate Change Reports*, 1(4), pp. 263-267.

Annan, J.D. and Hargreaves, J.C. (2006) 'Using multiple observationally-based constraints to estimate climate sensitivity', *Geophysical Research Letters*, 33(6).

Annan, J.D. and Hargreaves, J.C. (2013) 'A new global reconstruction of temperature changes at the Last Glacial Maximum', *Clim. Past*, 9(1), pp. 367-376.

Annan, J.D. and Hargreaves, J.C. (2017) 'On the meaning of independence in climate science', *Earth Syst. Dynam.*, 8(1), pp. 211-224.

Annan, J.D. and Hargreaves, J.C. (2020) 'Bayesian deconstruction of climate sensitivity estimates using simple models: implicit priors and the confusion of the inverse', *Earth Syst. Dynam.*, 11(2), pp. 347-356.

Annan, J.D., Hargreaves, J.C. and Mauritsen, T. (2022) 'A new global surface temperature reconstruction for the Last Glacial Maximum', *Clim. Past*, 18(8), pp. 1883-1896.

Armour, K.C. (2017) 'Energy budget constraints on climate sensitivity in light of inconstant climate feedbacks', *Nature Climate Change*, 7(5), pp. 331-335.

Armstrong McKay, D.I. *et al.* (2022) 'Exceeding 1.5°C global warming could trigger multiple climate tipping points', *Science*, 377(6611), p. eabn7950.

Arnell, N.W. *et al.* (2019) 'Global and regional impacts of climate change at different levels of global temperature increase', *Climatic Change*, 155(3), pp. 377-391.

Arrhenius, S. (1897) 'On the Influence of Carbonic Acid in the Air upon the Temperature of the Earth', *Publications of the Astronomical Society of the Pacific*, 9, p. 14.

Ashwin, P. and von der Heydt, A.S. (2020) 'Extreme Sensitivity and Climate Tipping Points', *Journal of Statistical Physics*, 179(5), pp. 1531-1552.

Baez, J.C. and Tweed, D. (2013) 'Monte Carlo Methods in Climate Science', *Math Horizons*, 21(2), pp. 5-8.

Baggenstos, D. *et al.* (2019) 'Earth’s radiative imbalance from the Last Glacial Maximum to the present', *Proceedings of the National Academy of Sciences*, 116(30), pp. 14881-14886.

Bao, Z. *et al.* (2021) 'The sensitivity of vegetation cover to climate change in multiple climatic zones using machine learning algorithms', *Ecological Indicators*, 124, p. 107443.

Batchelor, C.L. *et al.* (2019) 'The configuration of Northern Hemisphere ice sheets through the Quaternary', *Nature Communications*, 10(1), p. 3713.

Bayes, T. and Price (1763) 'LII. An essay towards solving a problem in the doctrine of chances. By the late Rev. Mr. Bayes, F. R. S. communicated by Mr. Price, in a letter to John Canton, A. M. F. R. S', *Philosophical Transactions of the Royal Society of London*, 53, pp. 370-418.

Beer, J., Mende, W. and Stellmacher, R. (2000) 'The role of the sun in climate forcing', *Quaternary Science Reviews*, 19(1), pp. 403-415.

Bjordal, J. *et al.* (2020) 'Equilibrium climate sensitivity above 5 °C plausible due to state-dependent cloud feedback', *Nature Geoscience*, 13(11), pp. 718-721.

Bloch-Johnson, J. *et al.* (2021) 'Climate Sensitivity Increases Under Higher CO2 Levels Due to Feedback Temperature Dependence', *Geophysical Research Letters*, 48(4), p. e2020GL089074.

Bochow, N. *et al.* (2023) 'Overshooting the critical threshold for the Greenland ice sheet', *Nature*, 622(7983), pp. 528-536.

Boers, N. and Rypdal, M. (2021) 'Critical slowing down suggests that the western Greenland Ice Sheet is close to a tipping point', *Proceedings of the National Academy of Sciences*, 118(21), p. e2024192118.

Booth, A., Goodwin, P. and Cael, B.B. (2024) 'Ice Sheet-Albedo Feedback Estimated From Most Recent Deglaciation', *Geophysical Research Letters*, 51(15), p. e2024GL109953.

Bouttes, N. *et al.* (2023) 'Deglacial climate changes as forced by different ice sheet reconstructions', *Clim. Past*, 19(5), pp. 1027-1042.

Box, J.E. *et al.* (2012) 'Greenland ice sheet albedo feedback: thermodynamics and atmospheric drivers', *The Cryosphere*, 6(4), pp. 821-839.

Box, J.E. *et al.* (2022) 'Greenland ice sheet climate disequilibrium and committed sea-level rise', *Nature Climate Change*, 12(9), pp. 808-813.

Bradley, A.T. and Hewitt, I.J. (2024) 'Tipping point in ice-sheet grounding-zone melting due to ocean water intrusion', *Nature Geoscience*, 17(7), pp. 631-637.

Brovkin, V. *et al.* (2021) 'Past abrupt changes, tipping points and cascading impacts in the Earth system', *Nature Geoscience*, 14(8), pp. 550-558.

Bryan, S.P. and Marchitto, T.M. (2008) 'Mg/Ca–temperature proxy in benthic foraminifera: New calibrations from the Florida Straits and a hypothesis regarding Mg/Li', *Paleoceanography*, 23(2).

Caballero, R. and Huber, M. (2013) 'State-dependent climate sensitivity in past warm climates and its implications for future climate projections', *Proceedings of the National Academy of Sciences*, 110(35), pp. 14162-14167.

Cabré, A., Marinov, I. and Leung, S. (2015) 'Consistent global responses of marine ecosystems to future climate change across the IPCC AR5 earth system models', *Climate Dynamics*, 45(5), pp. 1253-1280.

Cael, B. and Calafat, F. (in review) *Climate sensitivity & resistance since the Industrial Revolution*.

Cael, B.B. *et al.* (2023) 'Energy budget diagnosis of changing climate feedback', *Science Advances*, 9(16), p. eadf9302.

Cael, B.B. *et al.* (2022) 'Climate nonlinearities: selection, uncertainty, projections, and damages', *Environmental Research Letters*, 17(8), p. 084025.

Cael, B.B. and Goodwin, P. (2023) 'State-dependence of Cenozoic thermal extremes', *Communications Earth & Environment*, 4(1), p. 88.

Calafat, F. and Cael, B.B. (Submitted) 'Bayesian diagnosis of climate feedback evolution and forced temperature response', *Geophysical Research Letters*.

Caldwell, P.M. *et al.* (2014) 'Statistical significance of climate sensitivity predictors obtained by data mining', *Geophysical Research Letters*, 41(5), pp. 1803-1808.

Caldwell, P.M., Zelinka, M.D. and Klein, S.A. (2018) 'Evaluating Emergent Constraints on Equilibrium Climate Sensitivity', *Journal of Climate*, 31(10), pp. 3921-3942.

Caldwell, P.M. *et al.* (2016) 'Quantifying the Sources of Intermodel Spread in Equilibrium Climate Sensitivity', *Journal of Climate*, 29(2), pp. 513-524.

Callendar, G.S. (1938) 'The artificial production of carbon dioxide and its influence on temperature', *Quarterly Journal of the Royal Meteorological Society*, 64(275), pp. 223-240.

Cazenave, A. and Cozannet, G.L. (2014) 'Sea level rise and its coastal impacts', *Earth's Future*, 2(2), pp. 15-34.

Chalk, T.B. *et al.* (2017) 'Causes of ice age intensification across the Mid-Pleistocene Transition', *Proceedings of the National Academy of Sciences*, 114(50), pp. 13114-13119.

Chao, L.-W. and Dessler, A.E. (2021) 'An Assessment of Climate Feedbacks in Observations and Climate Models Using Different Energy Balance Frameworks', *Journal of Climate*, 34(24), pp. 9763-9773.

Chao, L.-W., Muller, J.C. and Dessler, A.E. (2022) 'Impacts of the Unforced Pattern Effect on the Cloud Feedback in CERES Observations and Climate Models', *Geophysical Research Letters*, 49(2), p. e2021GL096299.

Charney, J.G. *et al.* (1979) *Carbon dioxide and climate: a scientific assessment*. National Academy of Sciences, Washington, DC.

Cheng, L. *et al.* (2017) 'Improved estimates of ocean heat content from 1960 to 2015', *Science Advances*, 3(3), p. e1601545.

Clark, P.U., Alley, R.B. and Pollard, D. (1999) 'Northern Hemisphere Ice-Sheet Influences on Global Climate Change', *Science*, 286(5442), pp. 1104-1111.

Clark, P.U. *et al.* (2016) 'Consequences of twenty-first-century policy for multi-millennial climate and sea-level change', *Nature Climate Change*, 6(4), pp. 360-369.

Cooper, V.T. *et al.* (2024) 'Last Glacial Maximum pattern effects reduce climate sensitivity estimates', *Science Advances*, 10(16), p. eadk9461.

Covey, C., Sloan, L.C. and Hoffert, M.I. (1996) 'Paleoclimate data constraints on climate sensitivity: The paleocalibration method', *Climatic Change*, 32(2), pp. 165-184.

Cowtan, K. *et al.* (2015) 'Robust comparison of climate models with observations using blended land air and ocean sea surface temperatures', *Geophysical Research Letters*, 42(15), pp. 6526-6534.

Cox, P.M., Huntingford, C. and Williamson, M.S. (2018) 'Emergent constraint on equilibrium climate sensitivity from global temperature variability', *Nature*, 553(7688), pp. 319-322.

Dai, A. *et al.* (2020) 'Improved methods for estimating equilibrium climate sensitivity from transient warming simulations', *Climate Dynamics*, 54(11), pp. 4515-4543.

Danabasoglu, G. and Gent, P. (2009) 'Equilibrium Climate Sensitivity: Is It Accurate to Use a Slab Ocean Model?', *Journal of Climate - J CLIMATE*, 22, pp. 2494-2499.

Dessler, A.E. (2013) 'Observations of Climate Feedbacks over 2000–10 and Comparisons to Climate Models', *Journal of Climate*, 26(1), pp. 333-342.

Dessler, A.E. (2020) 'Potential Problems Measuring Climate Sensitivity from the Historical Record', *Journal of Climate*, 33(6), pp. 2237-2248.

Dessler, A.E., Mauritsen, T. and Stevens, B. (2018) 'The influence of internal variability on Earth's energy balance framework and implications for estimating climate sensitivity', *Atmos. Chem. Phys.*, 18(7), pp. 5147-5155.

Dietz, S. and Koninx, F. (2022) 'Economic impacts of melting of the Antarctic Ice Sheet', *Nature Communications*, 13(1), p. 5819.

Dong, Y. *et al.* (2020) 'Inter-model spread in the pattern effect and its contribution to climate sensitivity in CMIP5 and CMIP6 models', *Journal of Cimate*.

Elderfield, H. *et al.* (2012) 'Evolution of Ocean Temperature and Ice Volume Through the Mid-Pleistocene Climate Transition', *Science*, 337(6095), pp. 704-709.

Elneel, L. *et al.* (2024) 'Exploring Key Aspects of Sea Level Rise and Their Implications: An Overview', *Water*, 16(3), p. 388.

Eriksen, S. *et al.* (2021) 'Adaptation interventions and their effect on vulnerability in developing countries: Help, hindrance or irrelevance?', *World Development*, 141, p. 105383.

Etminan, M. *et al.* (2016) 'Radiative forcing of carbon dioxide, methane, and nitrous oxide: A significant revision of the methane radiative forcing', *Geophysical Research Letters*, 43(24), pp. 12,614-12,623.

Fabiano, F. *et al.* (2024) 'Multi-centennial evolution of the climate response and deep-ocean heat uptake in a set of abrupt stabilization scenarios with EC-Earth3', *Earth Syst. Dynam.*, 15(2), pp. 527-546.

Farnsworth, A. *et al.* (2019) 'Climate Sensitivity on Geological Timescales Controlled by Nonlinear Feedbacks and Ocean Circulation', *Geophysical Research Letters*, 46(16), pp. 9880-9889.

Fine, R.A. *et al.* (2017) 'A new look at ocean ventilation time scales and their uncertainties', *Journal of Geophysical Research: Oceans*, 122(5), pp. 3771-3798.

Flores, B.M. *et al.* (2024) 'Critical transitions in the Amazon forest system', *Nature*, 626(7999), pp. 555-564.

Forster, P. *et al.* (2021) 'The Earth's Energy Budget, Climate Feedbacks, and Climate Sensitivity', in Masson-Delmotte, V., P. Zhai, A. Pirani, S.L. Connors, C. Péan,, S. Berger, N.C., Y. Chen, L. Goldfarb, M.I. Gomis, M. Huang, K. Leitzell, E. Lonnoy, J.B.R. Matthews, T.K. and Maycock, T.W., O. Yelekçi, R. Yu, and B. Zhou (eds.) *Climate Change 2021: The Physical Science Basis. Contribution of Working Group I to the Sixth Assessment Report*

of the Intergovernmental Panel on Climate Change. Cambridge, United

Kingdom and New York, NY, USA: Cambridge University Press.

Forster, P.M. *et al.* (2016) 'Recommendations for diagnosing effective radiative forcing from climate models for CMIP6', *Journal of Geophysical Research: Atmospheres*, 121(20), pp. 12,460-12,475.

Fox-Kemper, B. *et al.* (2021) 'Ocean, Cryosphere and Sea Level Change', in Masson-Delmotte, V. *et al.* (eds.) *Climate Change 2021 – The Physical Science Basis: Working Group I Contribution to the Sixth Assessment Report of the Intergovernmental Panel on Climate Change*. Cambridge: Cambridge University Press, pp. 1211-1362.

Friedrich, T. *et al.* (2016) 'Nonlinear climate sensitivity and its implications for future greenhouse warming', *Science Advances*, 2(11), p. e1501923.

Fyke, J. *et al.* (2018) 'An Overview of Interactions and Feedbacks Between Ice Sheets and the Earth System', *Reviews of Geophysics*, 56(2), pp. 361-408.

Gallina, V. *et al.* (2016) 'A review of multi-risk methodologies for natural hazards: Consequences and challenges for a climate change impact assessment', *Journal of Environmental Management*, 168, pp. 123-132.

Gettelman, A. *et al.* (2019) 'High Climate Sensitivity in the Community Earth System Model Version 2 (CESM2)', *Geophysical Research Letters*, 46(14), pp. 8329-8337.

Gidden, M.J. *et al.* (2019) 'Global emissions pathways under different socioeconomic scenarios for use in CMIP6: a dataset of harmonized emissions trajectories through the end of the century', *Geosci. Model Dev.*, 12(4), pp. 1443-1475.

Glaubke, R.H. (2022) 'Taking the temperature of ancient oceans with foraminiferal Mg/Ca', *Nature Reviews Earth & Environment*, 3(6), pp. 359-359.

Gleckler, P.J., Taylor, K.E. and Doutriaux, C. (2008) 'Performance metrics for climate models', *J. Geophys. Res.*, 113.

Golledge, N.R. *et al.* (2019) 'Global environmental consequences of twenty-first-century ice-sheet melt', *Nature*, 566(7742), pp. 65-72.

Goodwin, P. (2016) 'How historic simulation–observation discrepancy affects future warming projections in a very large model ensemble', *Climate Dynamics*, 47(7), pp. 2219-2233.

Goodwin, P. (2018) 'On the Time Evolution of Climate Sensitivity and Future Warming', *Earth's Future*, 6(9), pp. 1336-1348.

Goodwin, P. (2021) 'Probabilistic projections of future warming and climate sensitivity trajectories', *Oxford Open Climate Change*, 1(1).

Goodwin, P. and Cael, B.B. (2020) 'Bayesian estimation of Earth's climate sensitivity and transient climate response from observational warming and heat content datasets', *Earth Syst. Dynam. Discuss.*, 2020, pp. 1-23.

Goodwin, P. *et al.* (2023) 'Climate feedbacks with latitude derived from climatological data and theory', *EGUsphere [preprint]*, 2023, pp. 1-40.

Goodwin, P. and Williams, R.G. (2023) 'On the Arctic Amplification of surface warming in a conceptual climate model', *Physica D: Nonlinear Phenomena*, 454, p. 133880.

Gregory, J.M. and Andrews, T. (2016) 'Variation in climate sensitivity and feedback parameters during the historical period', *Geophysical Research Letters*, 43(8), pp. 3911-3920.

Gregory, J.M. *et al.* (2020) 'How accurately can the climate sensitivity to CO2 be estimated from historical climate change?', *Climate Dynamics*, 54(1), pp. 129-157.

Gregory, J.M. *et al.* (2016) 'Small global-mean cooling due to volcanic radiative forcing', *Climate Dynamics*, 47(12), pp. 3979-3991.

Gregory, J.M., George, S.E. and Smith, R.S. (2020) 'Large and irreversible future decline of the Greenland ice sheet', *The Cryosphere*, 14(12), pp. 4299-4322.

Gregory, J.M. *et al.* (2019) 'Concepts and Terminology for Sea Level: Mean, Variability and Change, Both Local and Global', *Surveys in Geophysics*, 40(6), pp. 1251-1289.

Gregory, J.M. *et al.* (2004) 'A new method for diagnosing radiative forcing and climate sensitivity', *Geophysical Research Letters*, 31(3).

Grose, M.R. *et al.* (2018) 'What Climate Sensitivity Index Is Most Useful for Projections?', *Geophysical Research Letters*, 45(3), pp. 1559-1566.

Haeberli, W. and Weingartner, R. (2020) 'In full transition: Key impacts of vanishing mountain ice on water-security at local to global scales', *Water Security*, 11, p. 100074.

Hall, A. *et al.* (2019) 'Progressing emergent constraints on future climate change', *Nature Climate Change*, 9(4), pp. 269-278.

Hansen, J. (2008) 'Target atmospheric CO2: Where should humanity aim?', *Open Atmos. Sci. J.*, 2, pp. 217-231.

Hansen, J. and Sato, M. (2016) 'Regional climate change and national responsibilities', *Environmental Research Letters*, 11(3), p. 034009.

Hansen, J. *et al.* (2005) 'Efficacy of climate forcings', *Journal of Geophysical Research: Atmospheres*, 110(D18).

Hansen, J.E. and Takahashi, T. (1984) 'Climate processes and climate sensitivity', *Washington DC American Geophysical Union Geophysical Monograph Series*, 29.

He, H. *et al.* (2023) 'State dependence of CO₂ forcing and its implications for climate sensitivity', *Science*, 382(6674), pp. 1051-1056.

Hegerl, G. and Zwiers, F. (2011) 'Use of models in detection and attribution of climate change', *WIREs Climate Change*, 2(4), pp. 570-591.

Hegerl, G.C. *et al.* (2006) 'Climate sensitivity constrained by temperature reconstructions over the past seven centuries', *Nature*, 440(7087), pp. 1029-1032.

Hersbach, H. *et al.* (2018) 'Essential climate variables for assessment of climate variability from 1979 to present', *Copernicus Climate Change Service (C3S) Data Store (CDS)*.

Hill, E.A., Gudmundsson, G.H. and Chandler, D.M. (2024) 'Ocean warming as a trigger for irreversible retreat of the Antarctic ice sheet', *Nature Climate Change*, 14(11), pp. 1165-1171.

Hinkel, J. *et al.* (2015) 'Sea-level rise scenarios and coastal risk management', *Nature Climate Change*, 5(3), pp. 188-190.

Holland, D.M., Nicholls, K.W. and Basinski, A. (2020) 'The Southern Ocean and its interaction with the Antarctic Ice Sheet', *Science*, 367(6484), pp. 1326-1330.

Hooijer, A. and Vernimmen, R. (2021) 'Global LiDAR land elevation data reveal greatest sea-level rise vulnerability in the tropics', *Nature Communications*, 12(1), p. 3592.

Hope, C. (2015) 'The $10 trillion value of better information about the transient climate response', *Philosophical Transactions of the Royal Society A: Mathematical, Physical and Engineering Sciences*, 373(2054), p. 20140429.

Huang, Y., Xia, Y. and Tan, X. (2017) 'On the pattern of CO2 radiative forcing and poleward energy transport', *Journal of Geophysical Research: Atmospheres*, 122(20), pp. 10,578-10,593.

Huber, M., Beyerle, U. and Knutti, R. (2014) 'Estimating climate sensitivity and future temperature in the presence of natural climate variability', *Geophysical Research Letters*, 41(6), pp. 2086-2092.

ICCI (2024) *State of the Cryosphere 2024 – Lost Ice, Global Damage*. Stockholm, Sweden: (ICCI), I.C.C.I.

Inglis, G.N. *et al.* (2020) 'Global mean surface temperature and climate sensitivity of the early Eocene Climatic Optimum (EECO), Paleocene–Eocene Thermal Maximum (PETM), and latest Paleocene', *Clim. Past*, 16(5), pp. 1953-1968.

IPCC (2013) *Climate Change 2013: The Physical Science Basis. Contribution of Working Group I to the Fifth Assessment Report of the Intergovernmental Panel on Climate Change*.

IPCC (2019) *IPCC Special Report on the Ocean and Cryosphere in a Changing Climate*. Cambridge, UK and New York, NY, USA: Press, C.U.

IPCC (2021) *Climate Change 2021: The Physical Science Basis. Contribution of Working Group I to the Sixth Assessment Report of the Intergovernmental Panel on Climate Change*. Cambridge, United Kingdom and New York, NY, USA: Press, C.U.

IPCC (2022) *Climate Change 2022: Impacts, Adaptation, and Vulnerability. Contribution of Working Group II to the Sixth Assessment Report of the Intergovernmental Panel on Climate Change*. Cambridge, UK and New York, NY, USA: Press, C.U.

Jahn, A., Holland, M.M. and Kay, J.E. (2024) 'Projections of an ice-free Arctic Ocean', *Nature Reviews Earth & Environment*, 5(3), pp. 164-176.

Jeevanjee, N. *et al.* (2021) 'An Analytical Model for Spatially Varying Clear-Sky CO2 Forcing', *Journal of Climate*, 34(23), pp. 9463-9480.

Johansson, D.J.A. *et al.* (2015) 'Equilibrium climate sensitivity in light of observations over the warming hiatus', *Nature Climate Change*, 5(5), pp. 449-453.

Jones, P.D. *et al.* (1999) 'Surface air temperature and its changes over the past 150 years', *Reviews of Geophysics*, 37(2), pp. 173-199.

Kamae, Y. *et al.* (2016) 'Recent progress toward reducing the uncertainty in tropical low cloud feedback and climate sensitivity: a review', *Geoscience Letters*, 3(1), p. 17.

Karl, T.R. *et al.* (2015) 'Possible artifacts of data biases in the recent global surface warming hiatus', *Science*, 348(6242), pp. 1469-1472.

Kaufman, D. *et al.* (2020) 'Holocene global mean surface temperature, a multi-method reconstruction approach', *Scientific Data*, 7(1), p. 201.

Kim, Y.-H. *et al.* (2023) 'Observationally-constrained projections of an ice-free Arctic even under a low emission scenario', *Nature Communications*, 14(1), p. 3139.

Klose, A.K. *et al.* (2024) 'The long-term sea-level commitment from Antarctica', *The Cryosphere*, 18(9), pp. 4463-4492.

Knutti, R., Baumberger, C. and Hirsch Hadorn, G. (2019) 'Uncertainty Quantification Using Multiple Models—Prospects and Challenges', in Beisbart, C. and Saam, N.J. (eds.) *Computer Simulation Validation: Fundamental Concepts, Methodological Frameworks, and Philosophical Perspectives*. Cham: Springer International Publishing, pp. 835-855.

Knutti, R. and Hegerl, G.C. (2008) 'The equilibrium sensitivity of the Earth's temperature to radiation changes', *Nature Geoscience*, 1(11), pp. 735-743.

Knutti, R. and Rugenstein, M.A.A. (2015) 'Feedbacks, climate sensitivity and the limits of linear models', *Philosophical Transactions of the Royal Society A: Mathematical, Physical and Engineering Sciences*, 373(2054), p. 20150146.

Knutti, R., Rugenstein, M.A.A. and Hegerl, G.C. (2017) 'Beyond equilibrium climate sensitivity', *Nature Geoscience*, 10(10), pp. 727-736.

Knutti, R. and Tomassini, L. (2008) 'Constraints on the transient climate response from observed global temperature and ocean heat uptake', *Geophysical Research Letters*, 35(9).

Köhler, P. *et al.* (2015) 'On the state dependency of the equilibrium climate sensitivity during the last 5 million years', *Clim. Past*, 11(12), pp. 1801-1823.

Köhler, P. *et al.* (2017) 'A 156 kyr smoothed history of the atmospheric greenhouse gases CO2, CH4, and N2O and their radiative forcing', *Earth Syst. Sci. Data*, 9(1), pp. 363-387.

Kroese, D.P. *et al.* (2014) 'Why the Monte Carlo method is so important today', *WIREs Computational Statistics*, 6(6), pp. 386-392.

Kutzbach, J.E. *et al.* (2013) 'The dependence of equilibrium climate sensitivity on climate state: Applications to studies of climates colder than present', *Geophysical Research Letters*, 40(14), pp. 3721-3726.

Lambeck, K. *et al.* (2014) 'Sea level and global ice volumes from the Last Glacial Maximum to the Holocene', *Proceedings of the National Academy of Sciences*, 111(43), pp. 15296-15303.

Lambert, F. *et al.* (2012) 'Centennial mineral dust variability in high-resolution ice core data from Dome C, Antarctica', *Clim. Past*, 8(2), pp. 609-623.

Lau, S.C.Y. *et al.* (2023) 'Genomic evidence for West Antarctic Ice Sheet collapse during the Last Interglacial', *Science*, 382(6677), pp. 1384-1389.

Lawrence, J., Blackett, P. and Cradock-Henry, N.A. (2020) 'Cascading climate change impacts and implications', *Climate Risk Management*, 29, p. 100234.

Lecavalier, B.S. *et al.* (2014) 'A model of Greenland ice sheet deglaciation constrained by observations of relative sea level and ice extent', *Quaternary Science Reviews*, 102, pp. 54-84.

Lee, J.-Y. *et al.* (2021) 'Future Global Climate: Scenario-based Projections and Near-term Information', in Intergovernmental Panel on Climate, C. (ed.) *Climate Change 2021 – The Physical Science Basis: Working Group I Contribution to the Sixth Assessment Report of the Intergovernmental Panel on Climate Change*. Cambridge: Cambridge University Press, pp. 553-672.

Lenton, T.M. *et al.* (2024) 'Remotely sensing potential climate change tipping points across scales', *Nature Communications*, 15(1), p. 343.

Lenton, T.M. *et al.* (2008) 'Tipping elements in the Earth's climate system', *Proceedings of the National Academy of Sciences*, 105(6), pp. 1786-1793.

Lenton, T.M. *et al.* (2019) 'Climate tipping points—too risky to bet against', *Nature*, 575(7784), pp. 592-595.

Lenton, T.M. *et al.* (2006) 'Millennial timescale carbon cycle and climate change in an efficient Earth system model', *Climate Dynamics*, 26(7), pp. 687-711.

Letterly, A., Key, J. and Liu, Y. (2018) 'Arctic climate: changes in sea ice extent outweigh changes in snow cover', *The Cryosphere*, 12(10), pp. 3373-3382.

Levermann, A. *et al.* (2012) 'Potential climatic transitions with profound impact on Europe: Review of the current state of six ‘tipping elements of the climate system'', *Climatic Change*, 110, pp. 845-878.

Lisiecki, L.E. (2010) 'Links between eccentricity forcing and the 100,000-year glacial cycle', *Nature Geoscience*, 3(5), pp. 349-352.

Lowenstein, T.K. and Hönisch, B. (2012) 'The Use of Mg/Ca as a Seawater Temperature Proxy', *The Paleontological Society Papers*, 18, pp. 85-100.

Lunt, D.J. *et al.* (2010) 'Earth system sensitivity inferred from Pliocene modelling and data', *Nature Geoscience*, 3(1), pp. 60-64.

Madsen, M.S. *et al.* (2022) 'The role of an interactive Greenland ice sheet in the coupled climate-ice sheet model EC-Earth-PISM', *Climate Dynamics*, 59(3), pp. 1189-1211.

Mahlstein, I., Daniel, J.S. and Solomon, S. (2013) 'Pace of shifts in climate regions increases with global temperature', *Nature Climate Change*, 3(8), pp. 739-743.

Markwick, P. (2007) 'The palaeogeographic and palaeoclimatic significance of climate proxies for data-model comparisons', *Deep-time perspectives on climate change: marrying the signal from computer models and biological proxies*, pp. 251-312.

Martínez-Botí, M.A. *et al.* (2015) 'Plio-Pleistocene climate sensitivity evaluated using high-resolution CO2 records', *Nature*, 518(7537), pp. 49-54.

Martínez Montero, M. *et al.* (2024) 'Lost options commitment: how short-term policies affect long-term scope of action', *Oxford Open Climate Change*, 4(1).

Mateus, P., Mendes, V.B. and Pires, C.A.L. (2022) 'Global Empirical Models for Tropopause Height Determination', *Remote Sensing*, 14(17), p. 4303.

Matthews, H.D. *et al.* (2018) 'Focus on cumulative emissions, global carbon budgets and the implications for climate mitigation targets', *Environmental Research Letters*, 13(1), p. 010201.

Mauritsen, T. and Pincus, R. (2017) 'Committed warming inferred from observations', *Nature Climate Change*, 7(9), pp. 652-655.

McFarlane, N. (2011) 'Parameterizations: representing key processes in climate models without resolving them', *WIREs Climate Change*, 2(4), pp. 482-497.

Meehl, G.A. *et al.* (2020) 'Context for interpreting equilibrium climate sensitivity and transient climate response from the CMIP6 Earth system models', *Science Advances*, 6(26), p. eaba1981.

Mentaschi, L. *et al.* (2018) 'Global long-term observations of coastal erosion and accretion', *Scientific Reports*, 8(1), p. 12876.

Meraner, K., Mauritsen, T. and Voigt, A. (2013) 'Robust increase in equilibrium climate sensitivity under global warming', *Geophysical Research Letters*, 40(22), pp. 5944-5948.

Meyssignac, B. *et al.* (2023) 'Time-variations of the climate feedback parameter λ are associated with the Pacific Decadal Oscillation', *Communications Earth & Environment*, 4(1), p. 241.

Mohanty, A., Mohapatra, A.G. and Mohanty, S.K. (2024) 'Climate Change Impacts on Mangroves: Need for Resilience Mechanisms', in Padmakumar, V. and Shanthakumar, M. (eds.) *Mangroves in a Changing World: Adaptation and Resilience*. Cham: Springer Nature Switzerland, pp. 45-70.

Morice, C.P. *et al.* (2021) 'An Updated Assessment of Near-Surface Temperature Change From 1850: The HadCRUT5 Data Set', *Journal of Geophysical Research: Atmospheres*, 126(3), p. e2019JD032361.

Mostafa, M., Rahman, M.F. and Huq, S. (2016) 'Climate adaptation funding: Getting the money to those who need it', *Bulletin of the Atomic Scientists*, 72(6), pp. 396-401.

Mutton, H. *et al.* (2024) 'Feedbacks, Pattern Effects, and Efficacies in a Large Ensemble of HadGEM3-GC3.1-LL Historical Simulations', *Journal of Geophysical Research: Atmospheres*, 129(15), p. e2024JD041137.

Myhre, G. *et al.* (2013a) 'Radiative forcing of the direct aerosol effect from AeroCom Phase II simulations', *Atmos. Chem. Phys.*, 13(4), pp. 1853-1877.

Myhre, G. *et al.* (2013b) *Anthropogenic and Natural Radiative Forcing*. Cambridge, United Kingdom and New York, NY, USA.

Nicholls, Z. *et al.* (2021) 'Reduced Complexity Model Intercomparison Project Phase 2: Synthesizing Earth System Knowledge for Probabilistic Climate Projections', *Earth's Future*, 9(6), p. e2020EF001900.

Nicholls, Z. *et al.* (2020a) *Reduced complexity model intercomparison project phase 1: Protocol, results and initial observations*.

Nicholls, Z.R.J. *et al.* (2020b) 'Reduced Complexity Model Intercomparison Project Phase 1: introduction and evaluation of global-mean temperature response', *Geosci. Model Dev.*, 13(11), pp. 5175-5190.

Notz, D. and Community, S. (2020) 'Arctic Sea Ice in CMIP6', *Geophysical Research Letters*, 47(10), p. e2019GL086749.

Nummelin, A., Li, C. and Hezel, P.J. (2017) 'Connecting ocean heat transport changes from the midlatitudes to the Arctic Ocean', *Geophysical Research Letters*, 44(4), pp. 1899-1908.

Obase, T., Abe-Ouchi, A. and Saito, F. (2021) 'Abrupt climate changes in the last two deglaciations simulated with different Northern ice sheet discharge and insolation', *Scientific Reports*, 11(1), p. 22359.

Olson, R. *et al.* (2013) 'What is the effect of unresolved internal climate variability on climate sensitivity estimates?', *Journal of Geophysical Research: Atmospheres*, 118(10), pp. 4348-4358.

Osman, M.B. *et al.* (2021) 'Globally resolved surface temperatures since the Last Glacial Maximum', *Nature*, 599(7884), pp. 239-244.

Otto, A. *et al.* (2013) 'Energy budget constraints on climate response', *Nature Geoscience*, 6(6), pp. 415-416.

Papoulis, A. and Saunders, H. (1989) 'Probability, random variables and stochastic processes'.

Pattyn, F. *et al.* (2018) 'The Greenland and Antarctic ice sheets under 1.5 °C global warming', *Nature Climate Change*, 8(12), pp. 1053-1061.

Pfister, P.L. and Stocker, T.F. (2017) 'State-Dependence of the Climate Sensitivity in Earth System Models of Intermediate Complexity', *Geophysical Research Letters*, 44(20), pp. 10,643-10,653.

Pithan, F. and Mauritsen, T. (2014) 'Arctic amplification dominated by temperature feedbacks in contemporary climate models', *Nature Geoscience*, 7(3), pp. 181-184.

Prasch, M., Mauser, W. and Weber, M. (2013) 'Quantifying present and future glacier melt-water contribution to runoff in a central Himalayan river basin', *The Cryosphere*, 7(3), pp. 889-904.

Previdi, M., Smith, K.L. and Polvani, L.M. (2021) 'Arctic amplification of climate change: a review of underlying mechanisms', *Environmental Research Letters*, 16(9), p. 093003.

Quiquet, A. *et al.* (2021) 'Climate and ice sheet evolutions from the last glacial maximum to the pre-industrial period with an ice-sheet–climate coupled model', *Clim. Past*, 17(5), pp. 2179-2199.

Raitzsch, M. *et al.* (2018) 'Boron isotope-based seasonal paleo-pH reconstruction for the Southeast Atlantic – A multispecies approach using habitat preference of planktonic foraminifera', *Earth and Planetary Science Letters*, 487, pp. 138-150.

Raju, K.S. and Kumar, D.N. (2020) 'Review of approaches for selection and ensembling of GCMs', *Journal of Water and Climate Change*, 11(3), pp. 577-599.

Rasul, G. and Molden, D. (2019) 'The Global Social and Economic Consequences of Mountain Cryospheric Change', *Frontiers in Environmental Science*, 7.

Riahi, K. *et al.* (2017) 'The Shared Socioeconomic Pathways and their energy, land use, and greenhouse gas emissions implications: An overview', *Global Environmental Change*, 42, pp. 153-168.

Rial, J.A., Oh, J. and Reischmann, E. (2013) 'Synchronization of the climate system to eccentricity forcing and the 100,000-year problem', *Nature Geoscience*, 6(4), pp. 289-293.

Richardson, M. *et al.* (2016) 'Reconciled climate response estimates from climate models and the energy budget of Earth', *Nature Climate Change*, 6(10), pp. 931-935.

Ritchie, P.D.L. *et al.* (2021) 'Overshooting tipping point thresholds in a changing climate', *Nature*, 592(7855), pp. 517-523.

Rohling, E.J. *et al.* (2018) 'Comparing Climate Sensitivity, Past and Present', *Annual Review of Marine Science*, 10(1), pp. 261-288.

Rohling, E.J. *et al.* (2012a) 'Sea Surface and High-Latitude Temperature Sensitivity to Radiative Forcing of Climate over Several Glacial Cycles', *Journal of Climate*, 25(5), pp. 1635-1656.

Rohling, E.J. *et al.* (2012b) 'Making sense of palaeoclimate sensitivity', *Nature*, 491(7426), pp. 683-691.

Rohling, E.J. *et al.* (2021) 'Sea level and deep-sea temperature reconstructions suggest quasi-stable states and critical transitions over the past 40 million years', *Science Advances*, 7(26), p. eabf5326.

Rohrschneider, T., Stevens, B. and Mauritsen, T. (2019) 'On simple representations of the climate response to external radiative forcing', *Climate Dynamics*, 53(5), pp. 3131-3145.

Rose, B.E.J. *et al.* (2014) 'The dependence of transient climate sensitivity and radiative feedbacks on the spatial pattern of ocean heat uptake', *Geophysical Research Letters*, 41(3), pp. 1071-1078.

Rosier, S.H.R. *et al.* (2021) 'The tipping points and early warning indicators for Pine Island Glacier, West Antarctica', *The Cryosphere*, 15(3), pp. 1501-1516.

Rugenstein, M. *et al.* (2020) 'Equilibrium Climate Sensitivity Estimated by Equilibrating Climate Models', *Geophysical Research Letters*, 47(4), p. e2019GL083898.

Ryan, J.C. *et al.* (2019) 'Greenland Ice Sheet surface melt amplified by snowline migration and bare ice exposure', *Science Advances*, 5(3), p. eaav3738.

Sanderson, B.M. and O'Neill, B.C. (2020) 'Assessing the costs of historical inaction on climate change', *Scientific Reports*, 10(1), p. 9173.

Scherrenberg, M.D.W. *et al.* (2023) 'Modelling feedbacks between the Northern Hemisphere ice sheets and climate during the last glacial cycle', *Clim. Past*, 19(2), pp. 399-418.

Schlund, M. *et al.* (2020) 'Emergent constraints on equilibrium climate sensitivity in CMIP5: do they hold for CMIP6?', *Earth Syst. Dynam.*, 11(4), pp. 1233-1258.

Schmidt, G.A. *et al.* (2023) 'Anomalous Meltwater From Ice Sheets and Ice Shelves Is a Historical Forcing', *Geophysical Research Letters*, 50(24), p. e2023GL106530.

Schmittner, A. *et al.* (2011) 'Climate Sensitivity Estimated from Temperature Reconstructions of the Last Glacial Maximum', *Science*, 334(6061), pp. 1385-1388.

Schwartz, S.E. (2012) 'Determination of Earth’s Transient and Equilibrium Climate Sensitivities from Observations Over the Twentieth Century: Strong Dependence on Assumed Forcing', *Surveys in Geophysics*, 33(3), pp. 745-777.

Seeley, J.T. and Jeevanjee, N. (2021) 'H2O Windows and CO2 Radiator Fins: A Clear-Sky Explanation for the Peak in Equilibrium Climate Sensitivity', *Geophysical Research Letters*, 48(4), p. e2020GL089609.

Seroussi, H. *et al.* (2024) 'Evolution of the Antarctic Ice Sheet Over the Next Three Centuries From an ISMIP6 Model Ensemble', *Earth's Future*, 12(9), p. e2024EF004561.

Serreze, M.C. and Barry, R.G. (2011) 'Processes and impacts of Arctic amplification: A research synthesis', *Global and Planetary Change*, 77(1), pp. 85-96.

Shackleton, S. *et al.* (2023) 'Benthic δ18O records Earth’s energy imbalance', *Nature Geoscience*, 16(9), pp. 797-802.

Shaffer, G. *et al.* (2016) 'Deep time evidence for climate sensitivity increase with warming', *Geophysical Research Letters*, 43(12), pp. 6538-6545.

Shakun, J.D. *et al.* (2015) 'An 800-kyr record of global surface ocean δ18O and implications for ice volume-temperature coupling', *Earth and Planetary Science Letters*, 426, pp. 58-68.

Sherwood, S.C. *et al.* (2015) 'Adjustments in the Forcing-Feedback Framework for Understanding Climate Change', *Bulletin of the American Meteorological Society*, 96(2), pp. 217-228.

Sherwood, S.C. and Forest, C.E. (2024) 'Opinion: Can uncertainty in climate sensitivity be narrowed further?', *Atmos. Chem. Phys.*, 24(4), pp. 2679-2686.

Sherwood, S.C. *et al.* (2020) 'An Assessment of Earth's Climate Sensitivity Using Multiple Lines of Evidence', *Reviews of Geophysics*, 58(4).

Simms, A.R. *et al.* (2019) 'Balancing the last glacial maximum (LGM) sea-level budget', *Quaternary Science Reviews*, 205, pp. 143-153.

Simpson, N.P. *et al.* (2023) 'Adaptation to compound climate risks: A systematic global stocktake', *iScience*, 26(2), p. 105926.

Skeie, R. *et al.* (2014) 'A lower and more constrained estimate of climate sensitivity using updated observations and detailed radiative forcing time series', *Earth System Dynamics*, 5, pp. 139–175.

Skeie, R.B. *et al.* (2018) 'Climate sensitivity estimates – sensitivity to radiative forcing time series and observational data', *Earth Syst. Dynam.*, 9(2), pp. 879-894.

Smith, C.J. *et al.* (2023) 'Climate uncertainty impacts on optimal mitigation pathways and social cost of carbon', *Environmental Research Letters*, 18(9), p. 094024.

Smith, C.J. *et al.* (2018) 'FAIR v1.3: a simple emissions-based impulse response and carbon cycle model', *Geosci. Model Dev.*, 11(6), pp. 2273-2297.

Smith, C.J. *et al.* (2020) 'Effective radiative forcing and adjustments in CMIP6 models', *Atmos. Chem. Phys.*, 20(16), pp. 9591-9618.

Smith, C.J. *et al.* (2021) *The Earth’s Energy Budget, Climate Feedbacks, and Climate Sensitivity Supplementary Material*.

Smith, D.M. *et al.* (2019) 'The Polar Amplification Model Intercomparison Project (PAMIP) contribution to CMIP6: investigating the causes and consequences of polar amplification', *Geosci. Model Dev.*, 12(3), pp. 1139-1164.

Smith, R.S., George, S. and Gregory, J.M. (2021) 'FAMOUS version xotzt (FAMOUS-ice): a general circulation model (GCM) capable of energy- and water-conserving coupling to an ice sheet model', *Geosci. Model Dev.*, 14(9), pp. 5769-5787.

Snyder, C.W. (2016) 'Evolution of global temperature over the past two million years', *Nature*, 538(7624), pp. 226-228.

Sømme, T., Helland-Hansen, W. and Granjeon, D. (2009) 'Impact of eustatic amplitude variations on shelf morphology, sediment dispersal, and sequence stratigraphic interpretation: Icehouse versus greenhouse systems: REPLY', *Geology*, 37, pp. 587-590.

Spencer, R.W. and Christy, J.R. (2023) 'Effective climate sensitivity distributions from a 1D model of global ocean and land temperature trends, 1970–2021', *Theoretical and Applied Climatology*.

Stap, L.B. *et al.* (2017) 'The influence of ice sheets on temperature during the past 38 million years inferred from a one-dimensional ice sheet–climate model', *Clim. Past*, 13(9), pp. 1243-1257.

Steffen, W. *et al.* (2018) 'Trajectories of the Earth System in the Anthropocene', *Proceedings of the National Academy of Sciences*, 115(33), pp. 8252-8259.

Stevens, B. *et al.* (2016) 'Prospects for narrowing bounds on Earth's equilibrium climate sensitivity', *Earth's Future*, 4(11), pp. 512-522.

Stocker, T.F. *et al.* (2024) 'Reflecting on the Science of Climate Tipping Points to Inform and Assist Policy Making and Address the Risks they Pose to Society', *Surveys in Geophysics*.

Stokes, C.R. *et al.* (2022) 'Response of the East Antarctic Ice Sheet to past and future climate change', *Nature*, 608(7922), pp. 275-286.

Stone, E.J. and Lunt, D.J. (2013) 'The role of vegetation feedbacks on Greenland glaciation', *Climate Dynamics*, 40(11), pp. 2671-2686.

Taylor, K.E. *et al.* (2007) 'Estimating Shortwave Radiative Forcing and Response in Climate Models', *Journal of Climate*, 20(11), pp. 2530-2543.

Tebaldi, C. and Knutti, R. (2007) 'The use of the multi-model ensemble in probabilistic climate projections', *Philosophical Transactions of the Royal Society A: Mathematical, Physical and Engineering Sciences*, 365(1857), pp. 2053-2075.

Tierney, J.E. *et al.* (2020a) 'Past climates inform our future', *Science*, 370(6517), p. eaay3701.

Tierney, J.E. *et al.* (2020b) 'Glacial cooling and climate sensitivity revisited', *Nature*, 584(7822), pp. 569-573.

Tokarska, K.B. *et al.* (2020) 'Observational constraints on the effective climate sensitivity from the historical period', *Environmental Research Letters*, 15(3), p. 034043.

Trenberth, K.E., Fasullo, J.T. and Balmaseda, M.A. (2014) 'Earth's Energy Imbalance', *Journal of Climate*, 27(9), pp. 3129-3144.

Tschakert, P. *et al.* (2019) 'One thousand ways to experience loss: A systematic analysis of climate-related intangible harm from around the world', *Global Environmental Change*, 55, pp. 58-72.

UNFCCC (2023) *Technical dialogue of the first global stocktake. Synthesis report by the co-facilitators on the technical dialogue* (FCCC/SB/2023/9). UN Climate Change Conference - United Arab Emirates Nov/Dec 2023 - SBI 59, SBSTA 59.

Van Breedam, J., Goelzer, H. and Huybrechts, P. (2020) 'Semi-equilibrated global sea-level change projections for the next 10 000 years', *Earth Syst. Dynam.*, 11(4), pp. 953-976.

van der Ent, R.J. and Tuinenburg, O.A. (2017) 'The residence time of water in the atmosphere revisited', *Hydrol. Earth Syst. Sci.*, 21(2), pp. 779-790.

Vizcaíno, M. *et al.* (2008) 'Long-term ice sheet–climate interactions under anthropogenic greenhouse forcing simulated with a complex Earth System Model', *Climate Dynamics*, 31(6), pp. 665-690.

von der Heydt, A.S. and Ashwin, P. (2017) 'State dependence of climate sensitivity: attractor constraints and palaeoclimate regimes', *Dynamics and Statistics of the Climate System*, 1(1).

von der Heydt, A.S. *et al.* (2016) 'Lessons on Climate Sensitivity From Past Climate Changes', *Current Climate Change Reports*, 2(4), pp. 148-158.

von der Heydt, A.S. *et al.* (2014) 'On the state dependency of fast feedback processes in (paleo) climate sensitivity', *Geophysical Research Letters*, 41(18), pp. 6484-6492.

Wang, B. *et al.* (2024) 'Impact of Climate Change on the Dynamic Processes of Marine Environment and Feedback Mechanisms: An Overview', *Archives of Computational Methods in Engineering*, 31(6), pp. 3377-3408.

Waugh, D.W. and Eyring, V. (2008) 'Quantitative performance metrics for stratospheric-resolving chemistry-climate models', *Atmospheric Chemistry and Physics Discussions*, 8(3), pp. 10873-10911.

Webb, E.J. and Magi, B.I. (2022) 'The Ensemble Oceanic Niño Index', *International Journal of Climatology*, 42(10), pp. 5321-5341.

Weijer, W. *et al.* (2019) 'Stability of the Atlantic Meridional Overturning Circulation: A Review and Synthesis', *Journal of Geophysical Research: Oceans*, 124(8), pp. 5336-5375.

Willeit, M. *et al.* (2014) 'Time-scale and state dependence of the carbon-cycle feedback to climate', *Climate Dynamics*, 42(7), pp. 1699-1713.

Williamson, D. *et al.* (2015) 'Identifying and removing structural biases in climate models with history matching', *Climate Dynamics*, 45(5), pp. 1299-1324.

Wood, R.A. *et al.* (2023) 'A Climate Science Toolkit for High Impact-Low Likelihood Climate Risks', *Earth's Future*, 11(4), p. e2022EF003369.

Wunderling, N. *et al.* (2024) 'Climate tipping point interactions and cascades: a review', *Earth Syst. Dynam.*, 15(1), pp. 41-74.

Xiao, C.-D., Wang, S.-J. and Qin, D.-H. (2015) 'A preliminary study of cryosphere service function and value evaluation', *Advances in Climate Change Research*, 6(3), pp. 181-187.

Xiao, L. *et al.* (2017) 'Quantifying Snow Albedo Radiative Forcing and Its Feedback during 2003–2016', *Remote Sensing*, 9(9), p. 883.

Xu, Y. and Koll, D.D.B. (2024) 'CO2-Dependence of Longwave Clear-Sky Feedback Is Sensitive to Temperature', *Geophysical Research Letters*, 51(9), p. e2024GL108259.

Yoshimori, M. *et al.* (2016) 'A review of progress towards understanding the transient global mean surface temperature response to radiative perturbation', *Progress in Earth and Planetary Science*, 3(1), p. 21.

Zanna, L. *et al.* (2019) 'Global reconstruction of historical ocean heat storage and transport', *Proceedings of the National Academy of Sciences*, 116(4), pp. 1126-1131.

Zeebe, R.E. (2013) 'Time-dependent climate sensitivity and the legacy of anthropogenic greenhouse gas emissions', *Proceedings of the National Academy of Sciences*, 110(34), pp. 13739-13744.

Zelinka, M.D. *et al.* (2020) 'Causes of Higher Climate Sensitivity in CMIP6 Models', *Geophysical Research Letters*, 47(1), p. e2019GL085782.

Zelinka, M.D., Zhou, C. and Klein, S.A. (2016) 'Insights from a refined decomposition of cloud feedbacks', *Geophysical Research Letters*, 43(17), pp. 9259-9269.

Zhang, Y. *et al.* (2015) 'Glacier runoff and its impact in a highly glacierized catchment in the southeastern Tibetan Plateau: past and future trends', *Journal of Glaciology*, 61(228), pp. 713-730.

Zhou, C. *et al.* (2023) 'Explaining Forcing Efficacy With Pattern Effect and State Dependence', *Geophysical Research Letters*, 50(3), p. e2022GL101700.

Zhou, C. *et al.* (2021) 'Greater committed warming after accounting for the pattern effect', *Nature Climate Change*, 11(2), pp. 132-136.

Zhu, J. and Poulsen, C.J. (2020) 'On the Increase of Climate Sensitivity and Cloud Feedback With Warming in the Community Atmosphere Models', *Geophysical Research Letters*, 47(18), p. e2020GL089143.

Zhu, J. and Poulsen, C.J. (2021) 'Last Glacial Maximum (LGM) climate forcing and ocean dynamical feedback and their implications for estimating climate sensitivity', *Clim. Past*, 17(1), pp. 253-267.

Zhu, J., Poulsen, C.J. and Tierney, J.E. (2019) 'Simulation of Eocene extreme warmth and high climate sensitivity through cloud feedbacks', *Science Advances*, 5(9), p. eaax1874.

Zscheischler, J. *et al.* (2018) 'Future climate risk from compound events', *Nature Climate Change*, 8(6), pp. 469-477.